Faculty of Mechanical Technology and Engineering

# FLOW BEHAVIOUR AND SLIP VELOCITY EVALUATION THROUGH A CHANNEL WITH PARTIALLY FILLED OPEN-CELL FOAM

Khairul Azhar Bin Mustapha

Master of Science in Mechanical Engineering

2024

# FLOW BEHAVIOUR AND SLIP VELOCITY EVALUATION THROUGH A CHANNEL WITH PARTIALLY FILLED OPEN-CELL FOAM

**Khairul Azhar Bin Mustapha**

**A thesis submitted in fulfilment of the requirements for the degree of Master of Science in Mechanical Engineering**

**Faculty of Mechanical Technology and Engineering**



**UNIVERSITI TEKNIKAL MALAYSIA MELAKA**

**2024**

# DECLARATION

I hereby declare that this thesis entitled "Flow Behaviour and Slip Velocity Evaluation Through a Channel with Partially Filled Open-Cell Foam" is the result of my own research except as cited in the references. The thesis has not been accepted for any degree and is not concurrently submitted in candidature of any other degree.

| | | |
|---|---|---|
| Signature | : | ............ ....................................... |
| Name | : | Khairul Azhar Bin Mustapha |
| Date | : | 11 September 2024 |

# APPROVAL

I hereby declare that I have read this thesis and in my opinion this thesis is sufficient in terms of scope and quality for the award of Master of Science in Mechanical Engineering.

| | | |
|---|---|---|
| Signature | : | ... ............... .................................................... |
| Supervisor Name | : | Dr. Fadhilah Binti Shikh Anuar |
| Date | : | 11 September 2024 |

## DEDICATION

To my beloved mother and father and to the people that still finding their inner satisfying.

**ABSTRACT**

An open-cell metal foam (OCMF) is a porous structure material that is widely known among researchers and industries for its many benefits, such as its lightweight, low density, good impact absorption, and ability to transfer heat within its porous structure. However, using the foam in a fully filled configuration results in a high pressure drop, suggesting the need for a partially filled configuration. Hence, an interface condition between the clear and porous regions of the partially filled configuration must be well-understood to take advantage of its porous structure. This research aims to investigate fluid flow characteristics in the partially filled configuration, leading to the development of a slip velocity model for the OCMF. The foams used in the experiments were produced using an additive manufacturing method, where the images of 5 PPI (pores per inch) OCMF structures were used as a base structure in manipulating various pore diameters and porosities. The fluid flow characteristics across the 3D printed foams were investigated experimentally using a hot-wire anemometer and Computational Fluid Dynamics (CFD) simulation in Ansys Fluent Software. This study configured the porous structure of open-cell foam in two-dimensional (2D) simulation, since it is easier to be completed with less computational cost and the channel setup with a foam block can be considered symmetrical due to its rectangular design. Additionally, this study focused on obtaining averaging data in the free stream region to understand the effects of foam properties in the partially filled configuration. Based on the experimental data, the slip velocity model was developed using dimensional and regression analyses. Results show that the fluid flow behaviours in the partially filled channel would be affected by the presence of the foam, especially in the downstream region, where the velocity fluctuates and larger at the interface and clear regions. The foam size, pore diameter and blockage ratio are the significant factors that influence the flow behaviours in the partially filled channel. The pressure drop also varies from 343.53 - 1818.26 Pa/m at an inlet velocity of 5.0 m/s. Meanwhile, the slip velocity obtained from the proposed model is within the measurement uncertainties of the experimental studies. The slip velocity model that used an averaging value slightly underpredicted the real phenomenon at the interface region with a maximum percentage difference is 0.13 %. The secondary flow from the porous region caused a fluctuation of slip velocities and the values were higher than the inlet velocity.

***PENILAIAN TINGKAH LAKU ALIRAN DAN HALAJU GELINCIR MELALUI SALURAN SEPARA TERISI BUSA SEL TERBUKA***

## *ABSTRAK*

*Busa logam sel terbuka adalah satu struktur berliang yg sangat terkenal di kalangan penyelidik and pengamal industri disebabkan kelebihannya seperti bersifat ringan, ketumpatan yang rendah, penyerapan hentaman yang baik serta keupayaannya untuk mengalirkan haba melalui struktur berliang. Walau bagaimanapun, penggunaan busa secara pengisian penuh dalam satu saluran bendalir menyebabkan susutan tekanan yang tinggi, di mana, pengisian separuh busa logam sel terbuka disarankan bagi mengurangkan susutan tekanan tersebut. Oleh itu, keadaan antara dua kawasan, iaitu di antara kawasan yang berliang dan tidak berliang pada sistem saluran pengisian separuh ini perlu difahami dengan baik bagi memanfaatkan struktur berliang dalam saluran tersebut. Penyelidikan ini bertujuan untuk mengkaji sifat bendalir di dalam sistem saluran pengisian separuh dan menghasilkan satu model halaju gelincir untuk busa logam sel terbuka. Dalam kajian ini, busa sel terbuka dihasilkan mengunakan kaedah teknologi pembuatan aditif di mana gambar struktur asal busa logam 5 PPI (5 liang per inci) digunakan sebagai satu struktur asas dalam memanipulasikan pelbagai saiz diameter leliang dan keliangan. Sifat aliran bendalir melalui busa-busa tersebut telah dikaji dengan menggunakan anemometer dawai panas dan simulasi Pengkomputeran Dinamik Bendalir (CFD) menggunakan perisian "Ansys Fluent". Kajian ini mengkonfigurasi struktur berliang busa sel terbuka di dalam simulasi dua dimensi (2D), kerana ianya lebih mudah diselesaikan secara pengkomputeran dan saluran bersama blok busa tersebut boleh dianggap simetri berdasarkan bentuk segi empat tepatnya. Fokus kajian ini adalah untuk mendapatkan data purata bagi aliran dalam kawasan yang kosong di mana kawasan tersebut mungkin dipengaruhi oleh sifat busa yang terletak berhampiran dan memenuhi sebahagian saluran tersebut. Menggunakan data eksperimen, model halaju gelincir telah dihasilkan melalui analisis dimensi dan regresi. Hasil kajian menunjukkan dengan adanya busa sel terbuka dalam saluran, ia menyebabkan perubahan pada aliran bendalir terutamanya pada kawasan hilir, dengan nilai halaju tidak tetap di kawasan antara muka serta menjadi lebih laju di kawasan tidak berliang. Saiz busa, diameter leliang dan nisbah halangan adalah faktor penting yang mempengaruhi aliran bendalir di dalam sistem saluran pengisian separuh. Susutan tekanan juga berlaku, di mana jumlah susutan adalah dalam lingkungan 343.53 - 1818.26 Pa/m pada halaju masuk 5.0 m/s. Manakala, model halaju gelincir yang yang dicadangkan berada dalam ketakpastian pengukuran halaju gelincir yang diperolehi daripada eksperimen. Model halaju gelincir ini menggunakan nilai purata dari pelbagai parameter, dimana ia menghasilkan nilai yang sedikit rendah berbanding keadaan sebenar yang berlaku pada antara muka kawasan berliang dengan peratusan perbezaan tertinggi adalah sebanyak 0.13 %. Kehadiran aliran sukender pada antara muka kawasan berliang telah menyebabkan nilai halaju gelincir berubah-ubah dan ianya adalah lebih tinggi daripada halaju masuk.*

## ACKNOWLEDGEMENT

First and foremost, I would like to take this opportunity to express my sincere acknowledgement to my supervisor Dr. Fadhilah Binti Shikh Anuar from the Faculty of Mechanical Technology and Engineering, Universiti Teknikal Malaysia Melaka (UTeM) for her essential guidance, supervision, support and encouragement towards the completion of this thesis.

I would also like to express my greatest gratitude to Dr. Fatimah Al-Zahra Binti Sa'at from Faculty of Mechanical Technology and Engineering, as co-supervisor of this research for her advice, suggestions and guidance in this study especially in doing simulation for the flow behaviour for the porous foam using Computational Fluid Dynamic software (CFD). Special thanks to the KPT research grant under FRGS/1/2020/TK0/UTEM/03/2 for the financial support throughout this project.

Special thanks to my beloved mother, father and siblings for their moral support and trust in completing this degree. Lastly, I would like to thank myself for spending a lot of hours and effort in completing this study and thank you to everyone who had been associated with the crucial parts of the realization of this project.

## TABLE OF CONTENT

# LIST OF TABLES

# LIST OF FIGURES

## LIST OF APPENDICES

## LIST OF ABBREVIATIONS AND SYMBOLS

| | | |
|---|---|---|
| 3D | - | Three Dimensional |
| ABS | - | Acrylonitrile Butadiene Styrene |
| AM | - | Additive Manufacturing |
| CAD | - | Computed Aided Design |
| CFD | - | Computational Fluid Dynamics |
| CT | - | Computed Tomography |
| $d_l$ | - | Ligament diameter |
| DMLS | - | Direct Metal Laser Selective |
| $d_p$ | - | Pore diameter |
| EBM | - | Electron Beam Melting |
| $f$ | - | Inertial coefficient |
| FDM | - | Fused Deposition Modeling |
| FFF | - | Fused Filament Fabrication |
| h | - | Measured height |
| $h_f$ | - | Foam height |
| $h_c$ | - | Channel height |
| IR 4.0 | - | Fourth Industrial Revolution |
| K | - | Permeability |
| $l_f$ | - | Foam length |
| OCMF | - | Open-Cell Metal Foam |

| | | |
|---|---|---|
| PA | - | Polyamide / Nylon |
| PLA | - | Polylactic acid |
| PPI | - | Pore Per Inches |
| SLA | - | Stereolithography |
| SLS | - | Selective Laser Sintering |
| SLM | - | Selective Laser Melting |
| U | - | Measured velocity |
| $U_m$ | - | Mean pore velocity |
| $U_s$ | - | Slip velocity |
| $U_{inlet}$ | - | Inlet velocity |
| $U_0$ | - | Original velocity in unloaded wind tunnel |
| $U_m$ | - | Mean pore velocity |
| UV | - | Ultraviolet |
| $V_{void}$ | - | Void volume |
| $V_{total}$ | - | Total volume (full solid) |
| $\Delta P/\Delta l$ | - | Pressure drops per unit length |
| $\varepsilon$ | - | Porosity |
| $\mu$ | - | dynamic viscosity |
| $\mu_{fluid}$ | - | Fluid viscosity |
| $\rho_{fluid}$ | - | Fluid density |
| $1/\alpha$ | - | Viscous Coefficient |

## LIST OF PUBLICATIONS

1. Shikh Anuar, F., Mustapha, K. A., Mohd Sa'at, F. A. Z., Zini, N. H. M., Mat Tokit, E., Satishwara Rao, N., Hooman, K., and Abdi, I. A., 2023. Microstructural properties and surface roughness of 3D printed open cell-foam. *Jurnal Tribologi*.

2. Mustapha, K. A., and Anuar, F. S., 2022. Prediction of Slip Velocity at the Interface of Open-Cell Metal Foam Using 3D printed Foams. *Colloids and Interfaces*.

3. Mustapha, K. A., Anuar, F. S., Sa'at, F. A. Z. M., Tokit, E. M., Zini, N. H. M., and Tuan, T. B., 2021. Development of Small-Scale Wind Tunnel for Flow Visualization and Thermal-Fluid Experiments. *Proceedings of the MUCET 2021*, Melaka, Malaysia.

4. Mustapha, K. A., Shikh Anuar, F., Mohd Sa'at, F. A. Z., Zini, N. H. M., Mat Tokit, E., Satishwara Rao, N., Hooman, K., and Abdi, I. A., 2022. Production of Open-Cell Foam Using Additive Manufacturing Method and Porous Morphology Effects. *Proceedings of the ICESEAM 2021*, Melaka, Malaysia.

# CHAPTER 1

# INTRODUCTION

## 1.1 Background of study

Open-cell metal foam is a kind of porous media with a unique structure made of a solid matrix with interconnected pores. The open-cell metal foam is promising for wide applications due to its high strength, low density, good impact absorption, and its ability to move heat within its porous structure. The open-cell metal foam also has high porosity, commonly more than 90%, thus providing a large specific surface area and allowing the process of fluid mixing (Anuar, Malayeri, and Hooman, 2017). Due to its porous structure, naturally, the OCMF offers two different modes of heat transfer, (1) conduction which depends on the type of material used, and (2) convective heat transfer because of its pass-through structure. In other applications, OCMF has gained interest among researchers and industries over the years such as sound absorbers (Wan et al., 2021), dampers, filters (Mehrizi and Ravari, 2019) and in fuel cells as coolant distributors (Tan et al., 2018; Vazifeshenas, Sedighi, and Shakeri, 2020). In heat exchanger applications, normally the OCMF is used in HVAC&R, electronics cooling and solar thermal plants (Kuruneru et al., 2020).



In current practice, the open-cell metal foam can be manufactured utilizing several procedures such as direct foaming of melts, solid-gas eutectic solidification, and investment casting. In IR 4.0 era, an additive technology could be used to manufacture porous structures using either metallic or non-metallic materials. However, the usage of non-metallic material may restrict its potential in the thermal application. Nevertheless, the complicated structure of the porous foam in a pipe or channel may create a disturbance to the fluid flow, allowing a better fluid mixing for a higher heat transfer process. One major drawback of open-cell metal foam due to its complicated structure is a massive pressure drop. Alternatively, the OCMF can be arranged to partially fill a part of a tube or channel, instead of fully-filled the configurations. However, the partially filled configuration that contains a porous region and a non-porous region may induce a slip condition at the interface. Thus, the fluid behaviours and slip conditions must be well-understood to make use of the complicated structure of the open-cell foam. There are certain debates on slip and no-slip conditions at an interface region between porous and non-porous (free stream) regions. The most popular theory, Darcy law deduces there should be a statistical average of the slip velocity value immediately outside the porous block (Beaver and Joseph, 1967). Therefore, Beavers-Joseph (1967) proposed the presence of the slip condition at the interface region. Researchers also started to investigate the slip condition using extended models from either the Darcy or Beaver-Joseph models to describe flow in open-cell foam. However, a recent experimental study on OCMF by Shikh Anuar, Ashtiani and Hooman (2018) found a noteworthy outgoing flow from the porous into the free stream regions in a vertical direction through the interface, and there exist no-flow regions in certain areas of the porous structure. Thus, the effects of this secondary flow (a flow that comes out vertically from the porous structure to the free stream region through the interface region) at the interface region is still debated due to the presence of slip velocity and non-slip condition, contributed by its pore-ligament constructions. Moreover, the exposed structure next to a clear region is a surface with the ligament structure spikes and randomly distributed the small pores. The characteristic of another secondary flow, which is formed inside the porous region also remains unclear (Kim et al., 2021).

In this research, a reverse engineering technique is proposed to investigate the flow behaviours across a partially filled channel with open-cell foam. The exact structure of the original open-cell metal foam was produced by using additive manufacturing (AM) methods, where the pore diameter was enlarged to the desired size so that velocities in the partially filled channel, including pore velocity (velocity in the porous structure) can be experimentally measured using a hot-wire anemometer. A morphology test was conducted in choosing a better 3D printing method to minimize the frictional effects on the fluid flow behaviours. This research also proposes an open-cell metal foam slip velocity model through dimensional and regression analyses and gaining insights of what happened in the partially filled configuration by focusing more on the effects of open-cell foam with various heights and pore sizes.

## 1.2 Problem of statement

An OCMF is very valuable since it is used in a very wide range of applications (Mehrizi and Ravari, 2019; Vazifeshenas, Sedighi, and Shakeri, 2020) where it is typically produced using different types of conventional method (Banhart, 2000; Husain, Siddiquee, and Khan, 2022). The conventional method is seen to be very complicated and high in cost (Wan et al., 2021). For instance, an investment casting is a common method to produce OCMF where it may take a few steps to finalize the end product (Sutygina et al., 2020). However, with the introduction of the AM method, like 3D printing, (Zhang et al., 2022; Gama, Ferreira, and Barros-Timmons, 2019; Kim et al., 2021; Zhou et al., 2022; Wang et al., 2020) the open-cell foams have been successfully produced in a simpler method.



The fully filled configuration with open-cell metal foam has always been proposed in many applications but there is a constraint in pressure drop, in which the intricate structure of metal foam contributes to high pressure drop (Khadhrawi et al., 2020; Jadhav et al., 2022). Normally, the corresponding pressure drop in the fully filled configuration is considerably high which may generally about three to four folds of magnitude higher compared to an empty channel due to its complex structure (Qu, Xu, and Tao., 2012). At the same time, the pressure drop causes a reduction in the performance efficiency of the system (Zargartalebi and Azaiez, 2019) and the fluid also needs more pumping power to compensate the pressure drop (Lu, Zhang, and Yang, 2016). Thus, many studies have considered a partially filled configuration (Lu, Zhang, and Yang, 2016; Sener and Yataganbaba, 2016; Xu et al., 2018) to lessen the impact of pressure drop. However, the partially filled configuration with open-cell foam needs further study to understand the effects on the flow behaviours and pressure drop, especially with the presence of an interface region between the clear (non-porous region) and the porous region (Shikh et al., 2018). The OCMF studies usually adapted the general classical equation of porous media for different types of porous media such as bed rocks, and sands (Alvandifar and Amani, 2018). However, the well-known classical macroscopic models such as Beaver and Joseph (1967) and Kuznetsov (1996) could not accurately describe the real flow behaviours at the interface of OCMF (Anuar, Malayeri, and Hooman, 2017; Sauret, Abdi, and Hooman, 2014) and the findings contributed to additional modified models based on the Beaver-Joseph model. A lot of numerical studies (Yerramalle, Premachandran, and Talukdar, 2020; Kotresha and Gnanasekaran, 2020; Xu and Gong, 2018; Khadhrawi et al., 2020) and analytical studies (Mahmoudi, Karimi, and Mazaheri, 2014; Xu et al., 2018; Li and Hu, 2019) have been conducted on the partially filled configuration with porous medium. However, an intricate flow phenomenon at the interface region, including the slip velocity could not be accurately explained using a continuity equation since more experimental studies are required to address the real phenomenon occurs in that region (Nair and Sameen, 2015). The underlying theory on the interface condition, specifically for the open-cell metal foam should be investigated and validated by experiments. There are limited experimental works with open-cell metal foams that discussed the interface conditions, due to expensive foam samples, tedious, and time-consuming work. Nevertheless, additional experimental works are required to obtain accurate information in describing the flow behaviours and slip velocity at the interface of foam-fluid regions, and understanding the pressure drop effects.

## 1.3 Objectives of study

The main objectives of this research are:

1. To produce 3D printed open-cell foams based on a conventional open-cell metal foam structure.
2. To investigate flow characteristics patterns across a partially filled channel with open-cell foams.
3. To propose a predicted model for slip velocity at the interface of the metal foam-fluid region by correlating the flow characteristics with foam geometrical properties.

## 1.4 Scope of study

The scopes in this research are:

a) Three Dimensional (3D) printed open-cell foam structure is redesigned from the original 5 PPI open-cell metal foam, where the pore diameters are manipulated. Normally, the open-cell metal is classified based on pore density such as 5 PPI, 10 PPI, 30 PPI etc. This study used 5 PPI as a benchmark to produce 3D printed open-cell foam.

b) The 3D printed open-cell foams are manufactured using two types of AM technologies and morphology tests are conducted to select the best technology to produce the open-cell foams.

c) This research focuses on the effects of pore diameter and foam height on the flow behaviours and slips velocity in a partially filled channel. The flow inside the porous and non-porous regions is investigated experimentally and numerically.

d) This research will develop a slip velocity model from the 3D printed foam data that is applicable for 5 PPI open-cell foam and smaller pore diameters.

e) The effect of pressure drops due to the manipulating parameters e.g., the foam geometrical properties are also investigated as a part of this research, expecting their influences on the flow behaviours in the partially channel.

f) The numerical study is based on a two-dimensional model using the existing porous model in Ansys Fluent software and is compared to the results of the predicted model and experiments using the open-cell foams.

## 1.5 Thesis structure

This thesis structured in five chapters consists of an introduction, literature review, methodology, results and discussions, and also a conclusion and recommendations.



**Chapter 1 -** Introduction

This chapter describes the basis of this research that is relatable to the uses of open-cell metal foam in a partially filled configuration. A brief background of the research is presented along with the problem statement and the objectives of this research in giving the novelty and the purposes of this research. The scope of the study has also been outlined to illustrate the boundaries of this research.

**Chapter 2 –** Literature Study

A review of the previously published works is conducted to have more understanding of all aspects of the research and used as a guideline for achieving better results. It concludes the basis of history, some theoretical issues, significant parameters to be considered, previous experimental procedures, and analysis.

**Chapter 3** – Methodology

This chapter presents a methodology that describes an experimental setup and procedures used in this research to achieve the objectives. The methodology illustrates a full flow of the process that has been conducted starting from the image reconstruction of foam structure, foam production, experimental investigation, numerical studies and also dimensional analysis. Therefore, the numerical study is not the main procedure where it is conducted as a validation step for the experimental and predicted model.

**Chapter 4 –** Results and discussions

The discussion and analysis of the experimental and numerical findings are stated in this chapter. The analysis is conducted by referring to the research's objectives. The results for each case are presented starting from the experimental data, numerical results, and lastly a comparison with the predicted model.

**Chapter 5** – Conclusion and recommendations

A brief conclusion of the research findings and also recommendations for future works are provided in the chapter.

# CHAPTER 2

# LITERATURE REVIEW

## 2.1 Overview

This chapter is divided into several main sections, which discuss recent and past studies related to the open-cell foam that considers the fluid flow and pressure drop in a partially filled configuration. The history of open-cell metal foam and its physical properties are discussed in Section 2.2. The fluid flow and pressure drop that are being affected by the presence of a porous medium in various partially filled configurations are discussed in Sections 2.3 and Section 2.4, respectively, which covered experimental, numerical, and analytical approaches from past studies. The historical, and past studies on the slip velocity at the interface region are also discussed in Section 2.4 which concludes the possible key parameters that may affect the slip velocity and be considered for governing the correlation involving slip velocity with configuration in a partially filled state.



## 2.2 Open-cell metal foam and 3D printed foam production

### 2.2.1. Background of open-cell metal foam

The open-cell metal foam is a porous material that contains pores, in which the skeletal portion of the material is known as the "matrix" or "ligament". The ligament is a solid part contra with the pores that represent the voids within the structure. The microscopic structure of open-cell metal foam can be seen in Figure 2.1. The conventional open-cell metal foam commonly has randomly distributed pore diameters. Nowadays, the classification of porous foam is not only limited to conventional foam but its porous structure can be developed into a lattice structure using the lattice Boltzmann method (Hamidi et al., 2022; Shokouhmand, Jam, and Salimpour, 2011; Suga and Nishio, 2009). The lattice structure distributes the pore and ligament size evenly. Hence, the conventional and new generation of open-cell foam is classified as a type of porous media like beach sand, sandstone, limestone, human lung, etc., where its material structure consists of a solid matrix with interconnected pores.

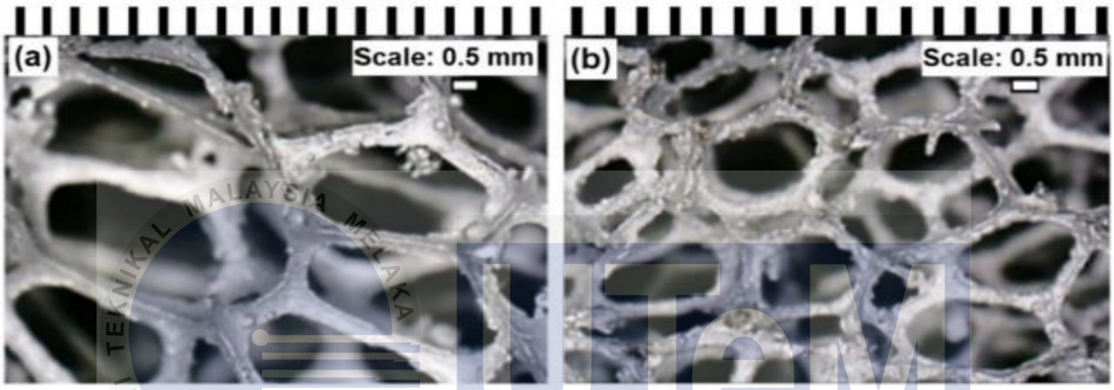


Figure 2.1: Example of microstructure image of open-cell metal foam for different pore densities: (a) 10 PPI and (b) 30 PPI (Shikh Anuar et al., 2018)



The open-cell metal foam gains industrial attention for its advantages of complicated porous structure, especially in heat transfer capabilities (Kuruneru et al., 2020). The OCMF is also promising for wide applications due to its high strength, low density, and good impact absorption. Moreover, based on the used material, e.g., aluminium, it may offer qualities like lightweight as it has high porosity of more than 90% and excellent heat transfer as it provides good thermal conductivity with a large specific surface area (Anuar, Malayeri, and Hooman, 2016). Naturally, the open-cell metal foam may introduce two distinct modes of heat transfer, which are conduction which depends on the type of material used, and convective heat transfer because of its pass-through structure. The open-cell metal foam has wider applications in the present day, especially in thermal fluid, compared to other uses such as sound absorption, dampening, and transportation because of its lightweight structure (Mehrizi and Ravari, 2019). In thermal engineering, many applications used metal foam such as micro-channel condensers with metal foam in the air side, flat-plate solar water collectors with metal foam blocks, finned metal foam heat sinks, and metal foam catalyst support (Vazifeshenas, Sedighi, and Shakeri, 2020). Many researchers (Shen et al., 2017; Orihuela et al., 2018; Alvandifar and Amani, 2018; Ahmed, Fadhil, and Salih, 2019) found that the metal foam with complicated interconnected pore-ligament construction has a good potential as a heat exchanger, but with one major drawback which is massive pressure drop effects. However, the metal foam can also be found in many industries such as geothermal systems, oil extraction, transpiration cooling, groundwater pollution, storing of nuclear waste, catalytic convertors, filters, and chemical reactors (Lu, Zhao, and Dennis, 2020). Therefore, it demonstrates the extensive applications of porous structures in various industries that acknowledge the superior characteristics of open-cell metal foam.

Initially, open-cell metal foam can be developed using a variation of conventional methods, including melt foaming by gas injection and solid-gas eutectic solidification (Banhart, 2000). The metal foam with a porosity, $\varepsilon$ of 89 to 93% and 60 to 85% can be produced through a method of melts foam using blowing agents and foam development method using powder as foaming agents, respectively (Husain, Siddiquee, and Khan, 2022). In the latter method, the foaming agents such as calcium and hydrides and blowing agents are mixed together with molten metal (i.e., wrought aluminium alloys and some cast alloys) to produce foaming from the inside. The mixture with the molten metal then needs to be heated to remove the driving agents and leave only the porous structure when cooled. Certain additives must be added to the molten metal to enhance the foaming process, where the molten metal is injected with gas to create a porous structure from the bottom surface and the fluid moves towards the surfaces. The metal is then compressed into rectangular blocks to give it shape. Investment casting is also one of the conventional production methods, where it consists of four main manufacturing steps, for example using reticulate polyurethane (PU); (1) PU foam template, (2) decomposition of PU foam, (3) filling melt metal inside the casting and (4) removing mold component (Sutygina et al., 2020). However, the microstructure of the open-cell foam could also be influenced by the process parameters for instance pattern and casting temperature which contribute to some disadvantages such as complicated production steps and high cost (Wan et al., 2021).

The open-cell metal foam characteristic can be determined in terms of pore density or PPI (pores per inch), where a larger PPI gives a smaller pore diameter, $d_p$ and vice versa. The pore density provides a qualitative measurement of pore diameters, hence using various foam sizes with equivalent PPIs may display various pore size distributions or mean values (Park, Seo, and Jeong, Seo, and Jeong, 2020). Another main characteristic is porosity, $\varepsilon$ which depends on the pore diameter and amount of ligament structures. Thus, the bulk porosity of the open-cell metal foam can be defined as a ratio of void volume, $V_{void}$ to total body volume, $V_{total}$. Commonly, the open-cell metal foam can be extremely porous, with void spaces are about 75 % to 95 % (Amin and Rashed, 2019). The permeability, K is also an important characteristic that describes a measure of the fluid flow, which passes across the foam's porous structure. The porous structure with low porosity is less permeable and typically has smaller pores, making it more difficult for fluid to pass through them. Meanwhile, high-porosity material has larger pores and is thus easily permeated. The physical properties of open-cell metal foam such as pore diameter, porosity and permeability, are related to each other. For example, when the pore diameter increases, the permeability also increases along with the porosity. However, it is important to note that an open-cell metal foam may have the same porosity but different permeability since those parameters can be influenced by the pore size distribution and its spatial arrangement (Costa, 2006). The permeability for 10 – 40 PPI metal foam with a range of porosity, from 0.75 to 0.97 can be calculated using Equation (2.1) and (2.2), respectively. However, for a smaller PPI foam, such as the 5 PPI foam, Equation (2.3) can be considered (Shikh Anuar et al., 2018). Alternatively, Darcy or Forchheimer equations can be used to determine the permeability of the porous materials by using pressure gradient data.

$$\epsilon = 1 - \frac{m_{solid}/\rho_{solid}}{V_{total}} \quad (2.1)$$

$$K = \frac{d_p d_l \epsilon}{6} \quad (2.2)$$

$$K = 0.00073.d_p^{\,2}.(1-\epsilon)^{-0.224}(d_l/d_p)^{-1.11} \quad (2.3)$$

### 2.2.2 Production of 3D printed open-cell foam using reverse engineering method

Reverse engineering is used to gain a better understanding of a product's design, identify, and recreate the product's components, which consequently increases the efficiency of a manufacturing process. The reverse engineering also implies the pathway "object-model-concept" which is the information from the original part utilized in creating a new model with the same design (Saiga et al., 2021). Today, the reverse engineering method is not only limited to engineering industries but is also widely used in a variety of applications such as historical objects, the development of computer games, etc. (Štefan and Janette, 2022). For many years, the only practical methods to manufacture the metal foams have been conventional techniques such as injecting gas into melts and solid-gas eutectic solidification, making it difficult to modify the porous structure for optimal fluid flow and prevent no-flow regions. The reverse engineering method using Computed Tomography (CT) scans could be used to duplicate the design of a porous metal foam (Matheson et al., 2017). The process involves the analysis of structure images of the porous foam from the translated x-ray beam and then generating the geometry of porous foam, including the pore and ligament diameters. Many researchers started to implement computed tomography (CT) scans as a reverse engineering method to have the exact design of a porous sample for their research (Fengshan et al., 2020; Jorge et al., 2019). Jorge et. al (2019) used 3D CT scans to study the characterization of Darcy and Forchheimer regimes from the realistic foam structures while Fengshan et al., 2020 used computed tomography using an x-ray beam to be applied in fluid flow simulation. Their study also used the CT scan to analyze the structure of the porous foam and generate the geometry of porous foam which enables the accuracy in measurement of pore and ligament diameters.

Industry 4.0 advancements have significantly improved the ability to use 3D printing for a wider range of applications, allowing for faster and easier production of complex parts using various technologies and materials. 3D printing is also commonly used for reverse engineering, creating samples with identical characteristics based on virtual models for further experimentation and allowing further investigation for experimental validation (Bracconi et al., 2019). The 3D printed samples can be generated by means of stereolithography, the technique for 3D printing which produces a solid model in a layer-by-layer fashion using photopolymerization. The AM is usually categorised into three different classes, mainly according to its material deposition; (1) laser based (2) direct printing and (3) nozzle-based systems (Qu, 2020; Hollister, 2006). There are a few types of additive manufacturing methods that are applicable to polymer material for instance, Fused Deposition Modelling (FDM), Stereolithography (SLA) and Selective Laser Sintering (SLS). The FDM or the other name Fused Filament Fabrication (FFF) is an example of an additive manufacturing technique where the process is a cutting-edge technology that can produce a reliable product while very cost-effective (Dileep et al., 2021). The FDM technique employed the use of thermoplastic material where the material is been heated to the melting temperature and then extrude onto the printing platform layer-by-layer (Solomon, Sevvel, and Gunasekaran, 2020). FDM technique also offers a fast printing process, low production cost, a variety of materials that can be used for the produced part, despite having a poor surface finish, and the needs for support structures (Kafle et al., 2021). There is also a major problem that may arise in using the FDM technique, where the nozzle will easily clog from extruding the printing material (Qu, 2020). The other polymer additive manufacturing technique like SLA applies a laser-based material deposition by focusing an ultraviolet (UV) laser beam to the liquid photopolymer in the polymerization process. This technology is very advantageous in producing a high-resolution product but still have insufficient information mechanical properties, extensive post-treatments, and uncured resin toxicity (Qu, 2020).

Meanwhile, the powder bed approach, including SLS, is also a widely used method in additive manufacturing due to its ability to produce complex shapes with a range of materials (Walker et al., 2014). However, the SLS technology can be used to produce standardized and optimized geometry, reducing variations in properties (Herdering et al., 2019). Lupone et al. (2022) agreed that the SLS technology enables the easy fabrication of complex geometries for polymer and composite parts without the need for supports or molds, making it the most cost-effective method compared to other additive manufacturing techniques or conventional methods. The study also asserted the potential uses of SLS in various fields, such as the production of spare parts and small series in the automotive and aerospace industries, as well as custom prostheses for biomedical applications. Wang et al. (2021) explained the process of using SLS composed of three main stages, starting from warming up, building and lastly, cooling process. The warming-up stage consists of the preheated process of the powder bed to a predefined temperature, during the printing process. In the building stage, a layer of powder is evenly spread making a powder bed onto the building platform. The spreading of powder is a crucial aspect of SLS technology, as it has a significant impact on the quality of the powder layer, including density and homogeneity. The deposition method also affects the forces exerted on the underlying solidified part. The process of spreading the powder can be done using either a roller or blade. However, the roller is preferred as it provides a higher-quality powder layer, and it has a larger contact area which leads to a more gradual rearrangement of particles during the spreading step (Haeri et al., 2017; Lupone et al., 2022; Wang et al., 2020). Meanwhile, the blade has limited interaction with the particles, leading to a rougher powder layer due to the occurrence of the dragging effect (Lupone et al., 2022). The cooling process is the last stage in the SLS technology, where the sintered part, including the building chamber gradually and evenly cooled down until a room temperature is reached (Brighenti et al., 2021; Lupone et al., 2022). However, a variation in the final output in terms of qualities, physical appearance, and surface roughness should be expected from a variety of additive manufacturing technologies (Adekanye et al., 2017). Since there are many 3D printing technologies in the market, a careful selection must be done to produce a quality open-cell foam to suit applications. The quality of the printed products depends on the layer thickness, nozzle temperature, platform temperature, printing speed, extruding rate, and layer height in the 3D printing process (Kumaresan et al., 2021).



Usually, different types of additive manufacturing technologies conducted with polymer materials have a different or specific form of materials; FDM with filament, SLS with powder and SLA with liquid form. The general materials that have been used for those polymer 3D printers are given in Table 2.1 where the FDM can use a wide range selection of materials. For FDM, the Polylactic acid (PLA) and Acrylonitrile Butadiene Styrene (ABS) are the most prominent selection of materials due to their high and good quality in tensile strength (Kafle et al., 2021). The PLA is one of the common materials in FDM due to its versatility, good performance and also have unique characteristics such as a relatively low melting point that is very beneficial in reducing the energy demand (Kottasamy et al., 2021). The PLA has excellent properties since it is tougher, more stable, and crystallizing more quickly (Silva et al., 2021). However, studies on materials for SLS technology are very limited (Khudiakova et al., 2020) even though there are a variety of polymeric sinterable materials. The application for the SLS is still limited due to a lack of comprehensive knowledge of the connections between raw materials, process transformation, and final properties (Brighenti et al., 2021). On the other hand, nylon PA 12 is a common thermoplastic material that has been used since it has a supercooling window, small crystallisation shrinkage, and stable processing (Omar et al., 2022). A study from Omar et al. (2022) conducted an investigation of a few compositions of nylon powder; virgin nylon and recycled nylon powder, where the virgin is slightly better in tensile strength and surface roughness compared to the recycled nylon material.

Table 2.1: Common print materials for FDM and SLS (Kafle et al., 2021)

| Additive Manufacturing (AM) Technology | Available Material/Type | Flexural Strength (MPa) | Elongation (%) |
|---|---|---|---|
| Fused Deposition Modelling, FDMn/ | PLA | 60 | 3 |
| | ABS | 86.14 – 102.20 | 4.5 – 10.6 |
| | Nylon | 83.59 – 114 | 5.81 – 10.6 |
| Selective Laser Sintering, SLS | PA12 | 86 ± 5 | 11 ± 0.5 |
| | PA 2200 | 19.89 - 59.23 | 3.28 - 4.96 |



As long as a CAD and STL. file is available, more objects can be produced rapidly and efficiently with various materials that can be used to fabricate the object. Recent research studies have shown that a variety of porous structures can be fabricated using various technologies and materials such as ceramic foam (Zhang et al., 2022), polyurethane composite foams (Gama, Ferreira, and Barros-Timmons, 2019), Vero Clear resin (Kim et al., 2021), and aluminium foam (Zhou et al., 2022). Wang et al. (2020) successfully created micromechanical models of a random open-cell foam using Voronoi technique. The Voronoi technique is a combination of methods that generate simple random pore structures based on Voronoi tessellation, which refers to the specific decomposition of a metric space using a given set of points. Xiao and Yin (2016) used three types of AM techniques as shown in Figure 2.2: (1) SLS, (2) Jet Fusion and (3) FDM to produce porous structure. Using a different approach, Costanza, Del Ferraro, and Tata (2022) used 3D printing to make a mold in casting aluminium foam with different cell shapes (rectangular, octahedron and icosahedron).

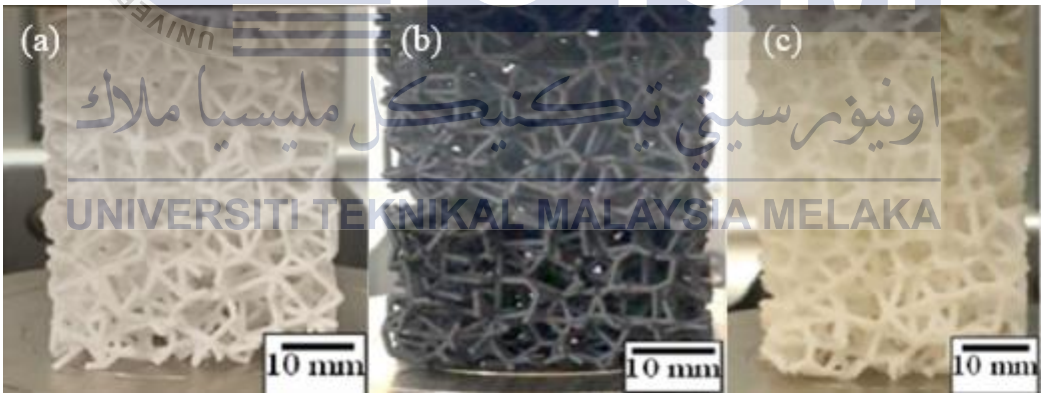




Figure 2.2: Foam structure with different printing technologies and materials (Wang et al., 2020): (a) SLS, (b) Jet Fusion and (c) FDM

Since the production of open-cell foam using 3D printing is not limited to polymer and composite materials, it can also be produced through various methods such as Selective Laser Melting (SLM), Electron Beam Melting (EBM), and Direct Metal Laser Sintering (DMLS). Basically, the SLM completely melts the materials, while DMLS fuses the material particles and bonds them together (Adekanye et al., 2017). Meanwhile, the EBM process involves an electron beam that melts each layer of raw materials (Adekanye et al., 2017). However, it is important to use a suitable material and electron beam for different 3D printing technologies. For example, using copper material with DMLS causes problems such as rapid reflection due to the high coefficient of thermal conductivity, curling and swelling. Meanwhile, the use of an electron beam in EBM can minimize optical reflectivity but still result in shrinkage of more than 12% (Pandey and Singh, 2019). Mostly the production method of aluminium foam using direct SLS, electron beam melting (EBM), and SLM may result in disadvantages since it will contribute to the high reflectivity of aluminium (that resulting to porosity) and high thermal conductivity of aluminium. The method is considered complicated and expensive (Wan et al., 2021). Westhoff et al. (2018) produced an OCMF with a stochastic model established on Laguerre tessellations using SLM. The Laguerre tessellation divides the region of interest into a system of convex polytopes (foam cell structures) through the random packing of non-overlapping spheres.



## 2.3 Classical theories on fluid flow in porous media

In fluid mechanics studies, fluid flow behaviour and characterization can be affected by the presence of solid or porous resistance in flow passages. The fluid velocity in a bounded flow without any resistance, such as one in a pipeline, is assumed to be zero at the wall and reaches a maximum in the center as shown in the velocity profiles of Figure 2.3 by Dou (2005). The fluid flows are classified into either laminar or turbulence flow, which is a critical factor in the design and operation of fluid systems. Laminar flow, also known as streamlined or viscous flow, is characterized by (1) layers of fluid flowing over one another at different speeds with little mixing between layers, (2) fluid particles moving in definite and observable paths or streamlines, and (3) being dominated by fluid viscosity. Turbulent flow is marked by the chaotic movement of fluid particles, with no observable pattern and no definite layers (Dou, 2005).

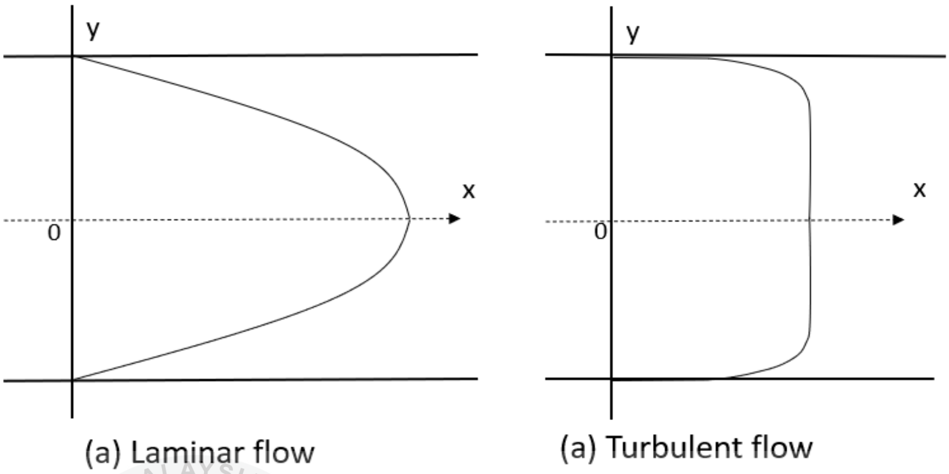


Figure 2.3: Types of flow (Dou, 2005)

Meanwhile, the fluid that passes through a resistance such as a porous medium can be classified into various regimes based on the local fluid velocity in the porous structure. The regimes are Darcy flow, weak inertia flow (pre-Darcy flow), non-Darcy flow, or turbulent flow (Macini, Mesini, and Viola, 2011).



### 2.3.1 Darcy law

Darcy's law is an equation that describes the flow of a fluid through a porous medium which is formulated by Henry Darcy based on the results of an experimental investigation on the flow of water through beds of sand as a porous medium (Atangana, 2018). Darcy's law, which expresses the conservation of momentum, is initially determined experimentally but has since been derived from the Navier–Stokes equations through homogenization (Atangana, 2018). The Navier-Stokes equation conduct for a laminar flow inside a free stream region. Darcy established a proportional relationship between flow rate and applied pressure difference for unidirectional flow in an isotropic medium, covering a laminar flow with the equivalent Reynold numbers (Jorge et al., 2019). The equation can be written as,

$$U = -\frac{K}{\mu}\frac{dP}{dl} \tag{2.4}$$

where U is the velocity in the direction of flow, $\mu$ is dynamic viscosity, dP/dl is pressure gradient or pressure per unit length K is the permeability of the porous materials. The Darcy Law has been modified and extended by using it as a base equation to generate a new equation that fits the specific application. The Forchheimer equation extends the Darcy equation to a higher Reynolds number regime and while the Brinkman equation modifies the Darcy equation to include effects at a lower Reynolds number regime (Koplik et al., 1983). The idea from Brinkman is to address the deficiency from the Darcy law in understanding and modelling fluid flow through the porous structure. The Darcy Law is often used to describe fluid flow through porous media, but it does have some limitations due to the occurrence of a jump in the velocity and shear stress at the interface. However, in some cases, particularly in the interface region between the fluid and the porous medium, these assumptions may not hold, leading to limitations in the accuracy of the Darcy law (Wu and Mirbod, 2018). In this case, more advanced models modified from the Darcy equation, such as the Brinkman equation are better at describing the fluid flow in the interface region where the Brinkman equation is shown in Equation (2.5). Brinkman's equation has always been used with the Navier-Stokes equation as a method for determining both regions (porous and free stream) (Wu and Mirbod, 2018).

$$\mu'\frac{d^2u}{dy^2} - \frac{\mu}{K}u - \frac{dP}{dx} = 0 \tag{2.5}$$

Meanwhile, Beaver-Joseph contributes to finding the slip conditions at the interface between the porous and free-stream regions in consideration of Darcy's law (representing a flow inside the porous medium) as a reference (Wu and Mirbod, 2018). Beaver and Joseph defined a new boundary condition that relates the velocity inside the porous region to the shear rate at the permeable boundary where the velocity approaching the interface indicated differs from the mean value within the porous material.

### 2.3.2 Forchheimer law

The theory of fluid flow across the porous structure is extended from the Darcy law for the uses in turbulence flow cases and also involving higher Reynold numbers. The Forchheimer-extended Darcy or also known as Hazen-Dupuit-Darcy improve the Darcy equation by improving the pressure drop term with inertial resistance as compared to Darcy's law (Park, Seo, and Jeong, 2020). Hence, the Forchheimer law is used for turbulent flow through a porous medium where both inertial and viscous effects are considered. Most researchers consider the Forchheimer instead of Darcy Law due to the inevitable usage of higher Reynold in many applications. The Forchheimer equation is shown in Equation (2.6):



$$-\frac{dP}{dl} = \frac{\mu}{K}U + \frac{\rho f}{\sqrt{K}}U^2 \tag{2.6}$$

where dP/dl is the pressure gradient or pressure drop per unit length (Pa/m), μ is the dynamic viscosity, ρ is the fluid density, $f$ is the inertial coefficient and K is the permeability. For most of the studies, the Brinkman-Forchheimer extension of the Darcy law is used to describe fluid flow through a porous medium (Bulat and Volkov, 2020). This form of motion equation is possible to account for non-Darcian effects, where the Brinkman term describes viscous effects and adds the possibility to apply a non-slip boundary condition at the walls or boundary, while the Forchheimer term describes form drag of the path and counting this term significant for high flow velocity.

### 2.3.3 Ergun law

The Ergun equation describes pressure drop behaviour by including two categories of flows that are Darcy and turbulent. Ergun's equation is also used to show the pressure drops of fluid flow through packed beds which are made of cylinders, rough sands, or other sphere-shaped particles. It is also commonly used in metal foam studies (Dukhan, Bağci, and Özdemir, 2014). The Ergun's equation is shown in Equation (2.7):

$$-\frac{dP}{dl} = \frac{150\mu(1-\varepsilon)^2}{d_p^2\varepsilon^3}U + 1.75\frac{(1-\varepsilon)}{\varepsilon^3}\frac{\rho U^2}{d_p} \tag{2.7}$$

where $d_p$ represents the pore diameter of the porous medium. The correlations of $1/\alpha$, viscous coefficient resistance and $\beta$, inertial resistance coefficient can be obtained when Equation (2.6) and Equation (2.7) are combined as shown in Equation (2.8) and Equation (2.9):

$$\alpha = \frac{d_p^2}{150} \cdot \frac{\varepsilon^3}{(1-\varepsilon)^2} \tag{2.8}$$

$$\beta = \frac{3.5}{d_p} \cdot \frac{(1-\varepsilon)}{\varepsilon^3} \tag{2.9}$$

There are many studies investigated the laminar flow across the porous media using the Darcy or Forchheimer's equation. For example, Jorge et al. (2019) used the Darcy model and Forchheimer model to do a thorough flow simulation of laminar flow in a periodic porous structure. The study served as a foundation for formulating and verifying the Darcy and Forchheimer coefficient expressions to periodic and random porous structures. Banerjee and Pasupuleti (2019) experimentally investigated the impact of converging boundaries on laminar flow in porous media. They assessed the suitability of the Forchheimer equation and analyzed its coefficients' behaviour under different converging angles. The researchers then compared their findings from the converging boundary tests to parallel flow results to understand the equation's influences.

## 2.4 Fluid flow behaviours across open-cell foam

### 2.4.1 Fluid Flow behaviours in partially filled configuration

Past pieces of literature (Khadhrawi et al., 2020; Kotresha and Gnanasekaran, 2018; Park, Seo, and Jeong, 2020; Tupin and Ohta, 2020) have adapted the classical model of porous media, like Darcy's Law, Forchheimer or a modified version into OCMF studies, focused on fully filled configurations. The OCMF in a fully filled configuration shows significant heat transfer and high pressure drop (Xu and Gong, 2018). Meanwhile, a partially filled configuration can be used as a replacement to minimise the pressure drop effects. Researchers have studied the fully and partially filled configurations with porous foam in different setups such as a rectangular channel or circular pipe (Qu, Xu, and Tao, 2012; Xu and Gong, 2018). The flows in the setups depend on the Reynolds number, which can be influenced by the fluid properties and types of characteristics length (Qu, Xu, and Tao, 2012; Xu and Gong, 2018). In a partially filled configuration, a pipe or channel is filled with a portion of a porous structure to create two major regions: (1) non-porous (free stream) region and (2) porous region. A small region between the free stream and porous regions is called an interface region. An example of a partially circular pipe is shown in Figure 2.4.

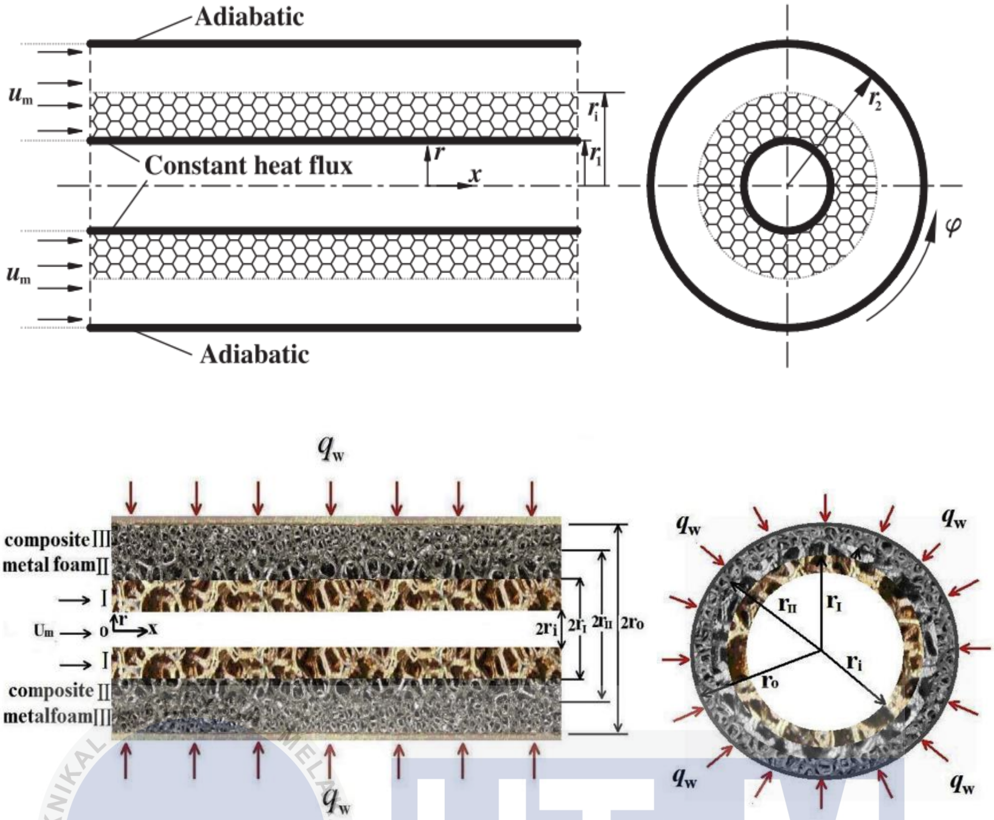


Figure 2.4: Partially filled with circular pipe from two different studies: (a) Qu, Xu, and Tao (2012) and (b) Xu and Gong (2018)



Shikh Anuar et al. (2018) found that the velocity in the non-porous region increased with a resistance of porous block, leading to a recirculation zone in a channel's downstream region. However, the recirculation zone only appeared with high PPI foam e.g., 30 PPI, where the pore sizes are very small. With low PPI foam like 10 PPI, where the pore sizes are larger, the incoming flow passed through the porous structure and exits through the rear of the porous block. It is also reported that the velocity profile shows an increasing trend towards the interface region of high PPI foam. However, the trend is only significant with a high blockage ratio (a foam height to channel height ratio) but diminished with the incoming inlet velocity. Hamidi et al. (2022) studied 5, 10, 20, 60 and 80 PPI metal foam by scanning the porous structures using 3D micro x-ray tomography and conducted a simulation in the Lattice Boltzmann Method (LBM). The result shows the fluid velocity profile across the porous structure is affected by pore diameter, while there is also the formation of vortexes occupying the spaces between the structure of the ligaments.

In another numerical investigation on tubes partially filled with composite metal foams (Xu and Gong, 2018), the momentum equation is developed using the Brinkman-Darcy model. The study found that the velocity profile inside the tube increases from the inner wall to the tube center (porous to free stream region). Xu and Gong (2018) also mentioned that the phenomenon occurs due to the reduction of flow resistance as the porosity increases. Qu, Xu, and Tao (2012) conducted an analytical study for a partially filled configuration inside of the annulus structure that is filled with 5 and 10 PPI metal foam. The study stated that an increase in porosity led to an increase in velocity with porous structure and a decrease in velocity in the open region. However, with higher PPI, the permeability of the porous foam decreases, leading to a decrease in pore velocity and an increased velocity peak in the fluid (no-porous) region. The high PPI foam causes the pore velocity to remain low even with a high incoming flow velocity and the low velocity in the porous structure is usually described by Darcy's Law.



### 2.4.2 Slip velocity at the interface of porous-clear region

The use of Darcy or Forchheimer with Navier-stokes equations is imminent in the case of partially filled configurations. In addition, the presence of the interface region in the partially filled configurations brings forth the importance of slip velocity in fluid flow studies with porous media. The fluid passes through the porous structure of the open-cell foam and may exit the pores at the interface region which totally causes the velocity at the interface unequal to zero (Guo et al., 2020). There are certain arguments over whether slip or no slip conditions will be more acceptable, considering the randomly distributed pores along the interface region. Moreover, the investigation on the partially filled configurations has been done since years ago, for instance, Beavers and Joseph (1967) who used metal foam inside an open rectangular channel, but the interface region remains an unresolved issue, especially for open-cell metal foam. From a theoretical point of view, Beavers and Joseph first proposed a method to deal with the boundary conditions at the interface and obtained the velocity distribution of fluid across porous media (Nield, 2009; Nair and Sameen, 2015; Guo et al., 2020). They proposed that there is a tangential slip velocity at the interface (velocity discontinuity at the fluid-solid interface), assuming that a shear effect is exerted from the interface to the porous medium through the boundary layer region until the velocity of the fluid decreases to the pore velocity. Beaver-Joseph studied the interface region by considering Darcy's law as a reference in determining the slip conditions (Wu and Mirbod, 2018). The theory of Beaver-Joseph defines a boundary condition that relates the velocity to the shear rate at the interface boundary layer as the velocity indicated differs from the mean value within the porous material. In the Beaver-Joseph (BJ) theory, they also stated when a viscous fluid passes by a porous structure, tangential stress causes the fluid to slide closely below the interface area, where the slip velocity is just a little bit higher than the pore velocity. The BJ equation is shown in Eq. (2.10), where the fluid slip velocity, $U_s$ is proportional to the shear rate at z = 0. In the equation, $U_m$ is the mean pore velocity in the porous region, and $\alpha$ is a dimensionless quantity which is independent of the height of the clear fluid channel or the viscosity of the fluid (McKay, 2001). Numerous experimental studies have been carried out by using the BJ equation to quantify $\alpha$ for a variety of materials with varying pore diameters (McKay, 2001).



$$\frac{dU_s}{dz} = \frac{\alpha}{\sqrt{K}}(U_s - U_m) \tag{2.10}$$

There is a study on the partially filled configurations has been conducted analytically (Xu et al., 2018) by adapting and extending the BJ theory at the interface region. However, the idea is opposed by Ochoa-tapia and Whitaker (1995) where a stress jump is introduced at the interface region (Shikh Anuar et. al., 2023). The volume averaging method is used in their study to categorize the different regions on either side of the interface and obtain the corresponding governing equations. Ochoa-Tapia and Whitaker's theoretical analysis of momentum transfer across the interface provided more understanding of the interfacial flow phenomenon, but the idea of slip velocity cannot be deduced due to a lack of experimental and numerical investigation to achieve a consistent boundary condition (Nair and Sameen, 2015). Both BJ and Ochoa-Tapia and Whitaker's models have been widely used in many studies of porous media and the difference between the theories can be referred in Figure 2.5. Vafai and Kim (1989) suggested that the velocity and shear at the interface should be treated continuously. Kuznetsov (1996) also extended the investigation carried out by Vafai and Kim (1990) earlier that considers a developed boundary condition which accounts for a jump in the stress at the interface from Ochoa-Tapia-Whitaker. Kuznetsov (1996) stated the condition from Ochoa-Tapia and Whitaker demonstrating not only a theoretical interest but also important in solving practical fluid flow problems. However, Kuznetsov (1996) only obtained analytical solutions for the steady fully developed laminar fluid flow and lacked experimental works to provide accurate information in illustrating slip velocity and boundary conditions at the interface of metal foam-fluid regions.

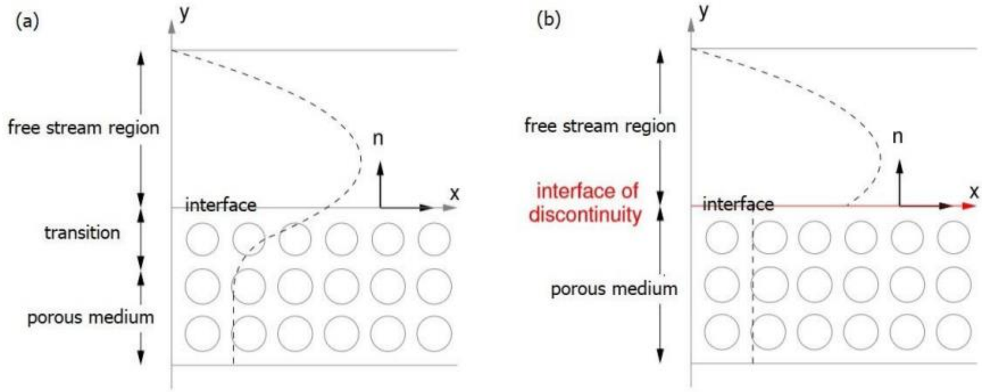


Figure 2.5: (a) Slip velocity (Beavers and Joseph, 1967) and (b) Flow discontinuity at the interface region (Ochoa-tapia and Whitakeri, 1995)

A non-uniform phase transition zone between a free stream and porous material is already described by Chandesris and Jamet (2006). By using the matched asymptotic expansion method, the boundary conditions were assessed. The investigation came to the conclusion that the pressure gradient and the properties of the transition zone are related to the stress jump condition. Numerous have considered numerical (Xu and Gong, 2018; Banjara and Nagarajan, 2020; Yerramalle, Premachandran, and Talukdar, 2020) and analytical study from Xu et al. (2018) in investigating the partially filled channel with porous medium cases since the experimental research are laborious, expensive, and time-consuming process. Unfortunately, employing the continuity equations is simply unable to explain the complex flow phenomenon at the interface of metal foam-fluid regions as conducted in the numerical studies (Xu and Gong, 2018; Banjara and Nagarajan, 2020; Yerramalle, Premachandran, and Talukdar, 2020). There is still no exact equation or model available to determine the slip velocity for metal foams with various pore diameters from Vafai and Kim, 1990; Beaver and Joseph, 1967 studies. Additional experimental works are required to obtain accurate information in describing the flow behaviours and slip velocity at the interface of foam-fluid regions. Following Beavers and Joseph's seminal investigation of the interface boundary conditions, some research has suggested alternative approaches for processing these conditions. The jump boundary conditions for mass flux (imposing continuity in the concentration and searching for a jump in the flux) between a microporous media and a homogeneous fluid were determined by Valdés-Parada, Goyeau, and Alberto Ochoa-Tapia (2006) using the volume averaging approach. It is demonstrated that the jump reaction coefficient varies with the porosity. The boundary conditions of velocity and stress at the interface can be derived using a method described by Wood, Quintard, and Whitaker (2000) who discovered that jump coefficients can be used to express the boundary conditions. An experimental study by Shikh Anuar et. al. (2018) also found the presence of no-slip and slip conditions along the interface regions of 10 and 30 PPI metal foam when using particle image velocimetry (PIV), and an infrared thermography camera as shown in Figure 2.6. The study found the impacts of pore density and foam height on the fluid velocity at the interface region. The location of the maximum fluid velocity in the partially channel is also different as compared to the classical models, asserting the important effects of frictional resistances and foam geometries on the incoming flow's momentum.



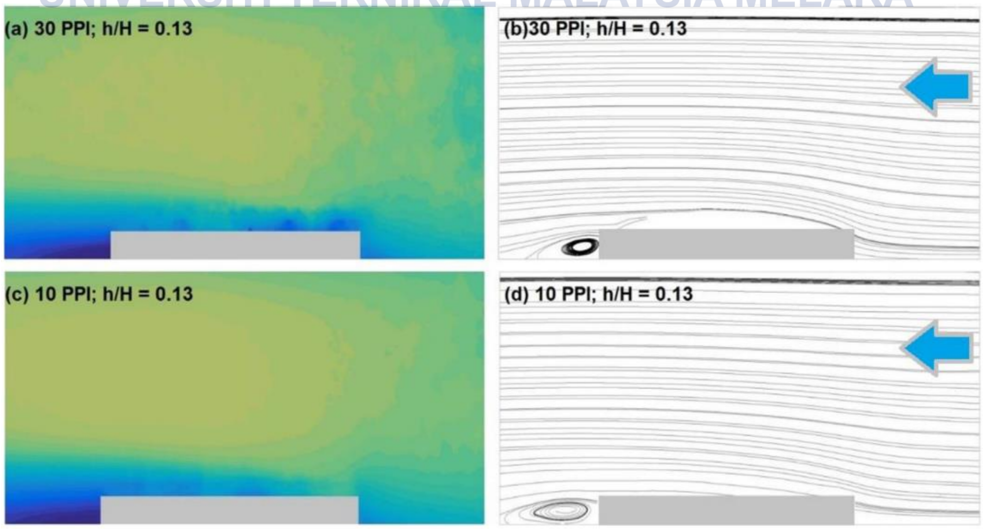


Figure 2.6: The flow behaviours across open-cell metal foam (Shikh Anuar, Ashtiani Abdi, and Hooman, 2018)

Terzis et al. (2019) used uniformly spaced micro-structured rectangular columns to create a porous medium with a porosity of 0.75 and then performed a single-phase flow experiment at a low Reynolds number, disclosing the fluid's microscopic velocity field in the porous medium. This led to the eventual achievement of the BJ and Ochoa-Tapia-Whitaker boundary conditions. Wu and Mirbod (2018) investigated the influence of porosity, Reynolds number, and thickness of porous media on velocity distribution and slip velocity using soft and random porous media samples made of diverse materials, such as 95% polyester and 5% silk. The experimental findings demonstrated that the velocity distribution and the analytical solution for the permeability of random porous media were in good agreement. Nakshatrala and Joshaghani (2019) applied the principle of virtual power and calculus of variation to obtain a complete set of interface conditions by considering a jump condition. The study also considered the BJ concept and BJ-Saffman (an extended BJ's boundary condition assuming a uniform pressure gradient in the porous medium) as special cases in their framework to reveal the assumptions and the validity of those conditions at the interface. BJ-Saffman concept is performed by Saffman by performing a statistical analysis where he argued that the velocity on the foam side is a higher-order term which should be neglected (Neale and Nader, 1974; Nakshatrala and Joshaghani, 2019). In their experimental study on partially filled configurations with open-cell metal foam, Alvandifar and Amani (2018) investigated heat transfer and pressure drop as a whole without delving into local and pore velocities. It is understandable since the micro-size pores (of open-cell metal foam) are impossible to be measured using conventional measuring equipment like a hot-wire anemometer.

As the experimental studies on the partially filled channel with open-cell metal foam are really limited, it could be the reason for the missing information on the secondary flows and unsaturated (no flow) regions in the porous metal foam. Moreover, another experimental study by Arbak et al. (2017) also found that the thermal entry length must be taken into account as the classical porous media model could not accurately describe the thermal development in the metal foam. However, it is important to extend BJ theory or provide a new model so that it may explain the fluid flow at the interface better. It should be recognized that a comprehensive understanding of fluid flow through porous and non-porous structures is crucial for optimizing heat transfer in partially filled configurations, thereby optimizing the use of open-cell metal foam.

### 2.4.3 Pressure drops effects

The intricate structure of open-cell foam causes massive pressure drops due to its interconnected ligament-pores and becomes a major drawback from real implementation (Shikh Anuar et al., 2018). Thus, a partially filled configuration is preferred to minimize the excess pressure drop (Shikh Anuar, Ashtiani and Hooman, 2018). An open-cell foam has a very large specific surface area and a large void fraction which is absolute and may reach more than 70 % and promotes low pressure drops (Bracconi et al., 2019). The pressure drop in metal foam is dependent on the microstructure of the porous material, which includes parameters such as porosity (or relative density), cell size, cell shape, and the morphology of the ligaments that form the pore network. (Dukhan, 2006). The open cell foam with a porosity over 90% provides an outstanding low pressure drop that simultaneously promotes heat transfer and radial mixing in heat transfer application (Bastos Rebelo et al., 2018). Mostly the pressure drop can be calculated, using a certain equation, or measured experimentally using pressure sensors.

Sener and Yataganbaba (2016) experimentally investigated 10 and 20 PPI alluminium foams within a channel with four distinct configurations, resulting in a decrease in the effect of Reynolds number (Re) on pressure drop for a surface curvature parameter greater than zero, regardless of pore density. The pressure field across the porous foam also increases with the inlet air velocity as shown in Figure 2.7 (Tang, Wang, and Huang, 2023). Moreover, from the past study, the pressure also decreased along the porous foam length relatively due to a few factors such as; (1) loss of local flow between fluid and ligament structure and (2) frictional effect. Liu et al. (2014) experimentally investigated the thermo-hydraulic characteristics of a tube partially filled with metal foam and discovered that increasing the PPI caused the pressure drop to rise first and then fall. The fluctuations of the pressure drop in the high PPI foams are claimed to occur due to (1) the high proportion of ligaments, which increases flow resistances and (2) the decrease in mass flow rate in the low permeability foam, which results in lower flow resistances. Lu, Zhang, and Yang (2016) utilized porous media characteristics such as the Brinkman-extended Darcy model to distinguish the pressure drops performances of metal foam. Their findings revealed that pressure drop increases with PPI, but that significant increases only occurred with low PPI foams (less than 15 PPI). The high PPI foam with more constraints drove the flow to head toward the free stream region, which reduced the total resistance effects brought on by the porous structure. At the same time, increasing the foam height and flow velocity can result in a larger pressure decrease as found by Shikh Anuar et al. (2018).

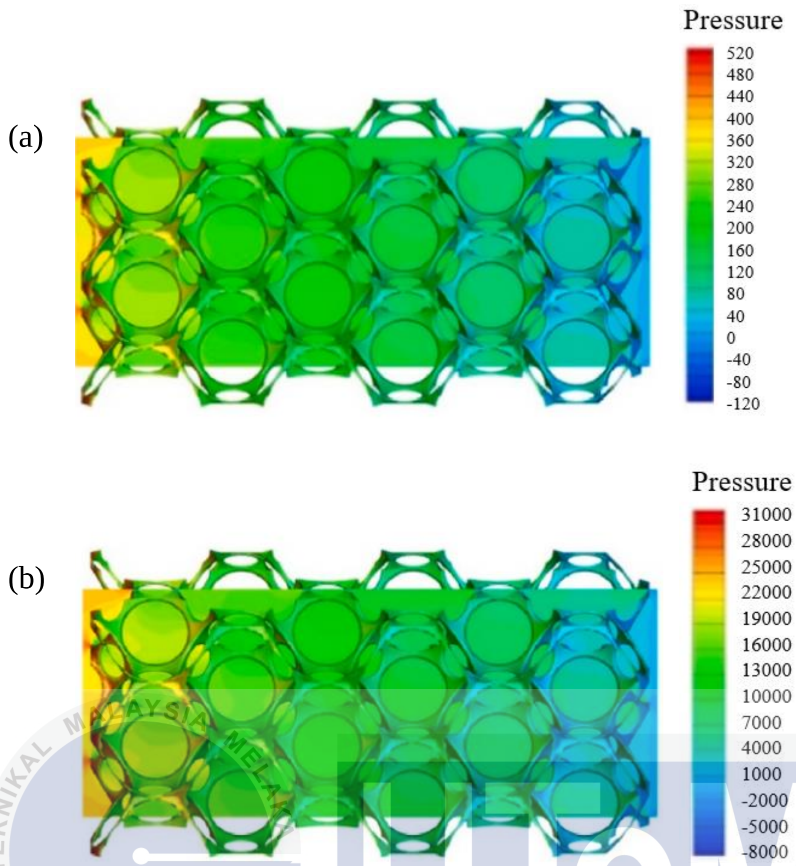


Figure 2.7: Pressure field from CFD simulation by (Tang, Wang, and Huang, 2023); (a) $U_{inlet}$ = 10 m/s and (b) $U_{inlet}$ = 80 m/s



Forooghi, Abkar, and Saffar-Avval (2011) in their numerical study discovered that the pressure drop effects were astounding once the porous medium had filled more than half of the channel. According to the study, when the blockage ratio exceeds 0.4, a smaller Darcy number, Da = $10^{-5}$, will only cause a higher pressure drop than Da = $10^{-4}$ work found that the pressure drop effects were remarkable once the porous medium has filled more than half of the channel. Hyung Jin Sung, Seo Young Kim, and Jae Min Hyun (1995) numerically investigated the impact of the Darcy number on the flow behaviour of a channel partially filled with a porous block with a larger recirculation zone appearing behind the porous block with a higher Reynolds number, Re = 500, as contrasted to Re = 100, at a constant Darcy number, Da = $10^{-5}$. However, neither any recirculation zone appears when the Darcy number is greater than $10^{-2}$. The study also discovered that pressure drops increase with porous height, but a fully filled channel caused a 400-fold higher pressure drop than a clear channel. Hu et al. (2020) studied porous medium by employing numerical simulation using computational fluid dynamics (CFD) and the open-Kelvin model which is alternatively termed sphere-subtraction and pillar models as a porous foam. The study found that the pressure drop increased with the increase of PPI and decreased with the porosity which can be attributed to a higher volume or number of ligaments that causes more disturbance and pressure loss to the airflow.

## 2.5 Numerical studies on porous media and 3D printed open-cell foam

There have been numerous numerical research studies concerning these porous media in the literature either related to fluid flow behaviour or pressure drop. Computational Fluid Dynamics (CFD) is the analysis of fluid flows using numerical solution methods where the analysis can provide information which is difficult to measure by experimental (Park, Seo, and Jeong, 2020). The same structure as porous media is required for performing in the computational domain to obtain the information. However, only a few research have directly compared the results of numerical analysis with experiments on the same specimen. Wood et al. (2015) performed direct numerical simulation on porous media structures and analyzed the laminar flow velocity distribution inside the randomly filled porous media using the Particle Image Velocimetry (PIV) technique. The study shows that both numerical and experimental studies show geometrical structure is identical to be compared directly whereas it also shows almost a similar pattern to be compared. Therefore, instead of the actual geometry of the porous media, CFD analysis is performed using a porous geometry constructed of an ideal mathematical model. Even though foam manufacturing is quite uniform, the sample's nominal porosity may deviate significantly from the sample's actual porosity, therefore manufacturers provide customers with actual porosity. Furthermore, because PPIs are a qualitative indicator of pore diameters so that different foams with equal PPIs might present different pore/cell size distributions or mean values. Thus, porosity is an appropriate property in defining a porous structure inside the analysis.

There are various types of models and setups of porous media that have been used with the fully and partially filled configuration in the numerical studies. A 20 PPI metal foam with a porosity, of 95.7% is used in the numerical simulation by Park, Seo, and Jeong (2020). The study mainly investigates the pressure drop for open-cell foam using a three-dimensional model where the real image is translated from the real structure through x-ray tomography. It stated that the pressure drop is affected by the friction drag force on the surface of the ligaments. Meanwhile, a flow separation also occurs due to the insufficient momentum from the flow to make the flow back against the adverse pressure gradient and the streamline also apart from the ligament surface. Their schematic diagram is shown in Figure 2.8.



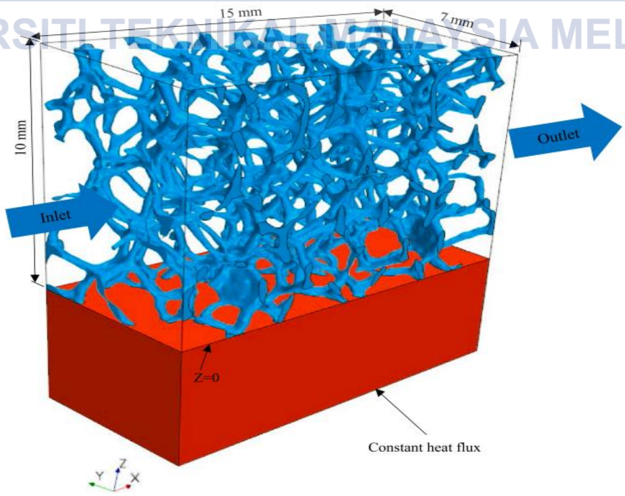


Figure 2.8: Schematic diagram of computational domain with REV of porous metal (Park, Seo, and Jeong, 2020)

Narasimmanaidu et al. (2021) investigated the flow behaviours across the complicated structure of the porous medium by setting up different blockage ratios and pore diameters (PPI) as a two-dimensional computational domain in Ansys Fluent. The study used an existing porous media equation (Ergun-Forchheimer) in the CFD simulation to describe the flow behaviours in the partially filled section with open-cell metal foam. The results show the metal foam with greater pore density than 30 PPI may act like a solid block, where the stagnant region could be wider as compared to the metal foam with a bigger pore diameter. Another study from Diani et al. (2014) used 5, 10, 20, and 40 PPI copper foams in Simpleware software where the original metal foam structure is scanned by using microcomputer tomography. The CT scan images were meshed in the software and exported to Ansys Fluent software for fluid flow simulation. The study concludes that the pressure gradient or pressure drop per unit length, $\Delta P/l$ is found in having a quadratic relation to the velocity where it also increases when the number of pores per inches, PPI increases (smaller pore diameter).

Shuja and Yilbas (2007) investigated two different porosities (0.9726 and 0.8991) of porous media with an aspect ratio ranging from 0.25 to 4.00 in a channel at the inlet air velocity of 0.085 m/s. The flow across the porous foam has been formulated through governing equations of mass continuity, energy, and momentum. A similar behaviour was found between the low aspect ratios of porous and solid blocks where a stagnation region appeared at the region facing the foam is set up in the middle with distance around the samples. Furthermore, a recirculation flow appeared behind the solid block for an aspect ratio of 4, but not for the porous block due to the penetration of flow through its structure. Yu et al. (2021) considered a fully filled channel with a porous structure as shown in Figure 2.9 to study the flow characteristics. The 3D model of the porous structure was reconstructed using Image J and Mimics Research software while the porous structure has been provided from an X-ray CT scan. The porous foam length at the inlet region was extended two times of length to produce uniform velocity distribution while the outlet region is extended ten times to avoid the occurrence of recirculation flow. In solving the mass and momentum equations, Fluent software was used in this study as also SIMPLER algorithm to couple between pressure and velocity. The velocity increases significantly as the air enters the porous structure while the presence of obstacles (porous structure) inside the channel leads to the emergence of a stagnation zone on the leeward side of the frame.

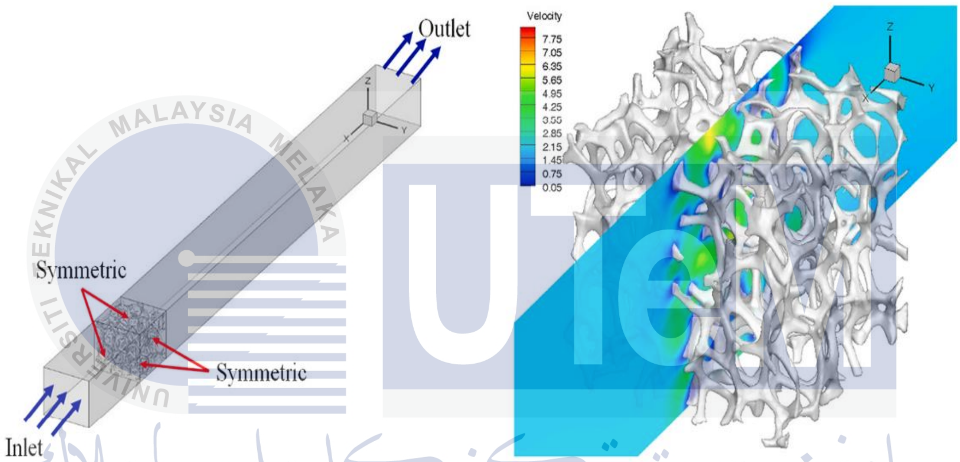




Figure 2.9 : Computational domain and cross-section velocity distributions (Yu et al., 2021)



The flow behaviour has also been numerically investigated in 2D simulation using the commercially available software Fluent by Jadhav and Gnanasekaran (2021). The parameters geometry including the metal foam properties are considered from Sauret, Abdi, and Hooman (2014). The investigation involved the instalment of metal foam structure with different pore diameters and heights (pore diameter: 20 and 40; height: 3 mm and 4 mm) inside a channel and provided with inlet velocity up to 30 m/s. The 2D simulation used a standard k-ε turbulence model for the porous region. The investigation from Jadhav and

Gnanasekaran (2021) resulting the velocity differs with the different pore density which is expected the smallest pore density to achieve a higher value. Meanwhile, the findings from Sauret, Abdi, and Hooman (2014). show the pore diameter and PPI indicates almost no influence on the velocity contour whereas the data set from the velocity profile for 20 and 40 PPI has a very small difference. This is occurrence may be due to a very thin foam used in the channel and the pore diameter too small where it can be assumed to be a solid block for a fluid flow to ignore it. A recent numerical study by Kotresha and Gnanasekaran (2020) on 20 and 40 PPI foams applied continuity in shear stress at the interface like many other studies but no detailed information on the slip velocity is given. However, an interesting finding from the numerical studies as the velocity is increase as the foam thickness and pore density increase. The flow resistance also increases from the increase of the foam thickness and pore density that brings the airflow to rush into the open space.

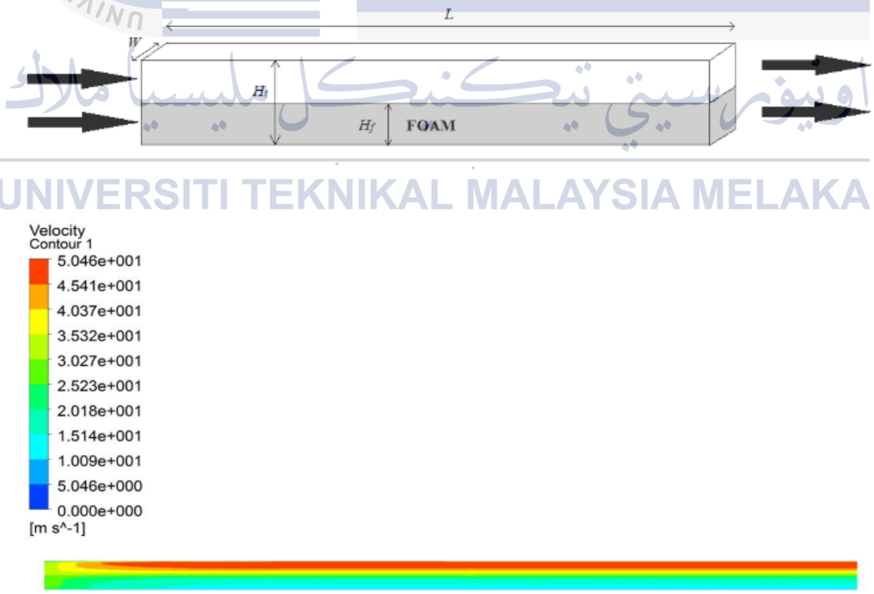




Figure 2.10 : Schematic computational domain and velocity contour (Sauret, Hooman, et al., 2014)

## 2.6 Summary

The conventional method to produce the open-cell foam required more steps that is time-consuming. However, with the growth of additive manufacturing technologies, the open-cell foam with complicated structure can be produced using a variety of techniques and materials. In the comparison of the AM technologies, laser-based 3D printing such as SLS is superior in producing the complicated structures of the foam whereas the raw materials would technically bond together thus giving a better surface finish (Omar et al., 2022). However, the production of porous structure by a metallic material is restricted for laser-based technologies due to the high reflectivity that occurs during the process, which can cause unwanted porosity.

Meanwhile, in applications that may relate to the fluid behaviour across the open-cell foam, a partially filled configuration is suggested since the configuration may benefit from a lower pressure drop effect. However, it still needs further studies for instance flow the phenomenon at the interface region which is in between of porous and free stream region. The interface condition is still being debated nowadays where Beaver and Joseph figured out the presence of stress jump which is a slip on the interface region. However, there is almost no further discussion on factors from OCMF that may affect the slip velocity at the interface region and the investigation is still limited, especially from the point of experimental studies. The condition inside the porous region is still uncovered in details due to its small and complicated structure, but may become a significant factor in affecting the interface region.

# CHAPTER 3

# METHODOLOGY

## 3.1 Overview

In this chapter, the methodology used in this research is illustrated in a flow chart as shown in Figure 3.1. The flow chart shows a composition of experimental stages used to achieve the objectives of this research, conducted to understand the fluid flow behaviours and propose a model of slip velocity in a partially filled channel with open-cell metal foam. This research used 3D printed open-cell foam as the tested samples, produced using reverse engineering and additive manufacturing methods. The physical properties of 3D printed open-cell foam were examined and their effects on flow characteristics were investigated in a close-loop wind tunnel. The slip velocity and flow behaviour in the wind tunnel experimental data were verify using Computational Fluid Dynamics (CFD) analysis conducted with Ansys Fluent (version 2022). The methodology of this research is thoroughly explained in the chapter.

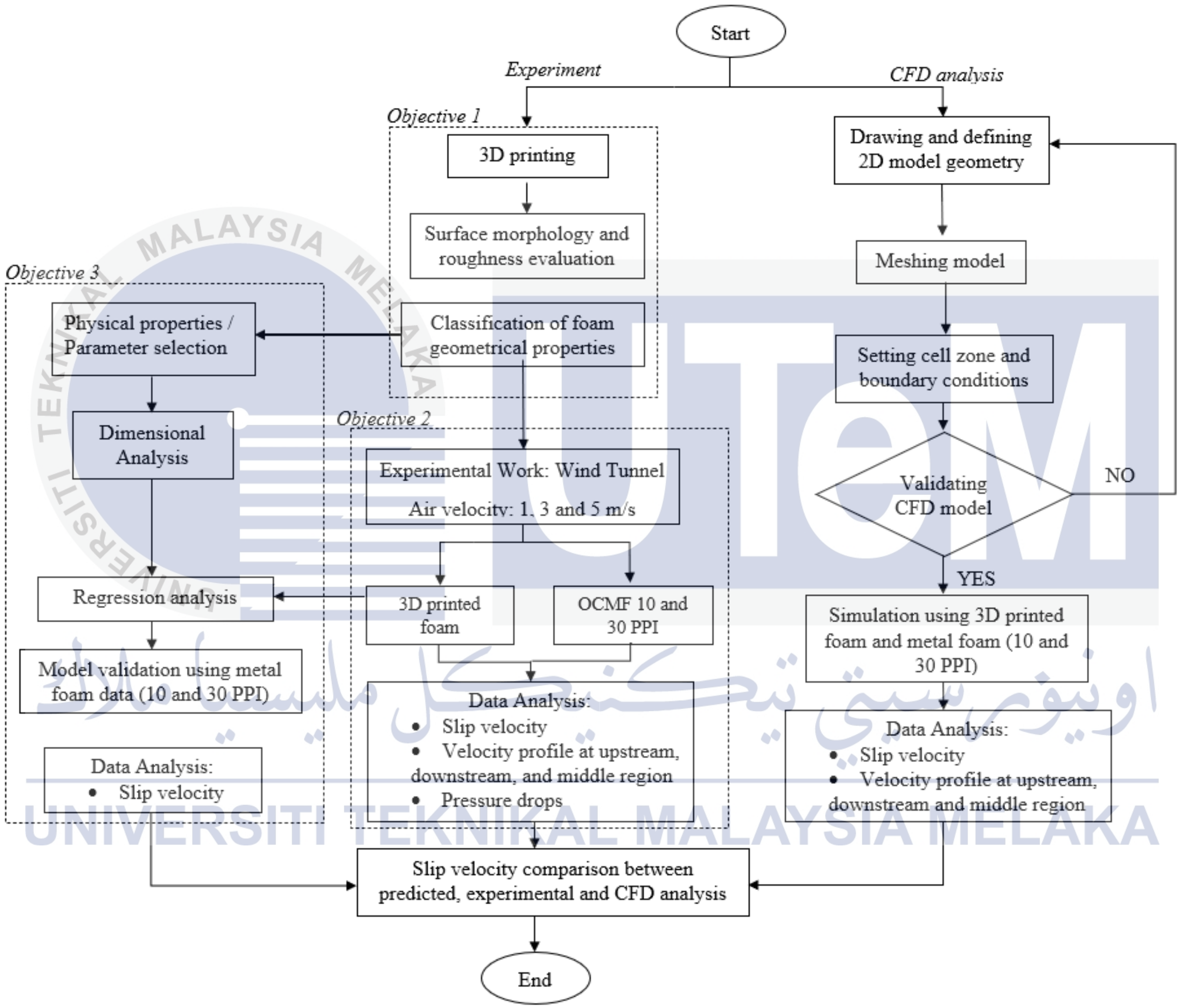


Figure 3.1: Flow chart of methodology

## 3.2 Production of 3D printed open-cell foam and physical properties determination

This research intends to use 3D printed open-cell foam in investigating the slip velocity at the interface region between porous and clear regions. The 3D printed foam was selected as the test sample in this research due to the difficulty in measuring flow velocity in the small pores of the original open-cell metal foam. A reverse engineering method was employed to recreate the porous structure of the open-cell foam using an AM method. This study has engaged the reverse engineering method starting from replicating the 5 PPI structure and resizing the pore size using CAD software, followed by the production of foam samples using the 3D printing techniques. The CT-scan also a part of reverse engineering but has not been covered in details since it is out of this study's work scope.

### 3.2.1 Dimension and reconstruction on open-cell metal foam

The 3D printed open-cell foam was produced based on the original, 5 PPI OCMF as shown in Figure 3.2. The 5 PPI was selected as a benchmark in producing the porous structure instead of 10, 30 PPI etc. since it has the largest pore diameter amongst the OCMF where it guaranteed a flow transition inside the structure that may be difficult to achieve with a larger PPI. Generally, a CT scan is an intricate and dynamic tool, and its usage covers a wide range of inspection works and is capable to provide a model or drawing for reverse engineering purposes. This advanced scan provides an efficient way to obtain measurements and build an accurate CAD model of an object. The CT scan uses an x-ray beam to illustrate the porous structure of open-cell foam (composition of ligaments and pores) and provide an almost accurate structural image in the meshed form. However, it is important to note that this research does not involve scanning the porous structure of the open-cell metal foam but starting with an image reconstruction to match the test section of the wind tunnel. Twelve samples of 3D printed open-cell foam were produced with their pore diameters, $d_p$ was larger than the original pore diameter of 5 PPI metal foam, which is 5.77 mm. The morphology of the 3D printed foams was also investigated, considering there are many kinds of AM technologies with various selections of materials. An example of CAD images of 3D printed open-cell foam is shown in Figure 3.3.

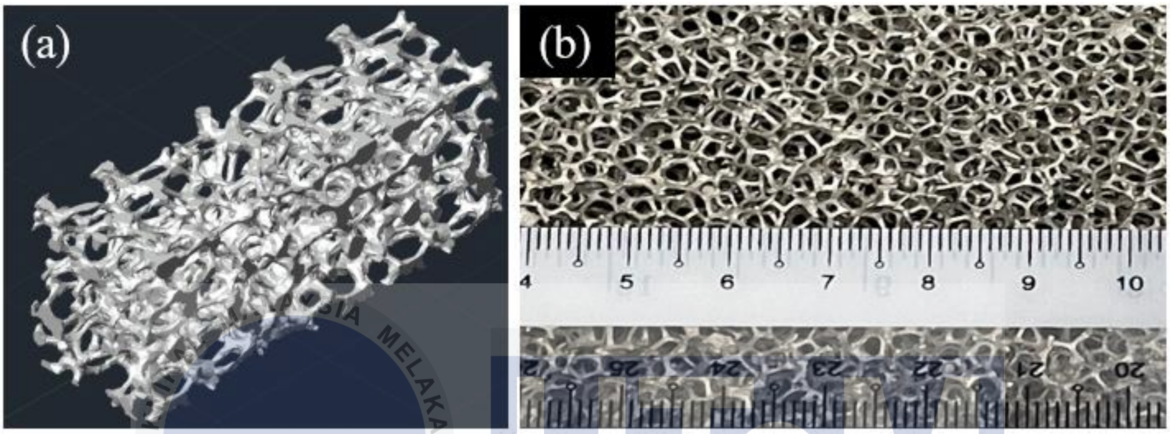


Figure 3.2: 5 PPI open-cell metal foam: (a) CT scan image translation and (b) original microstructure



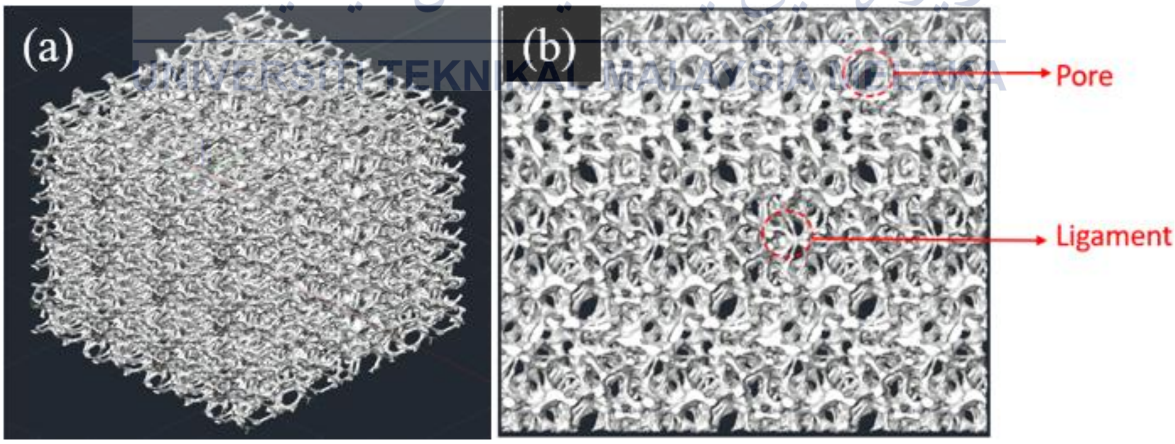


Figure 3.3: 3D printed open cell foam: (a) CAD drawing 2 scale foam and (b) microstructure of the open cell foam

The images of open cell foam were reconstructed using CAD software, AutoCAD (version 2022) to manipulate pore and ligament diameters to various sizes (2, 4, and 6 times larger than the 5 PPI metal foam). It is noteworthy to mention that the original size of OCMF cannot be produced using a 3D printer like SLS since the ligament thickness is too small, which is about 1.13 mm as stated in Table 3.3. Since the foam samples are made of nylon powder, it is easily broken when dusting off the powder (Mustapha et al., 2022). Thus, the enlargement of foam size which is started from 2 scales, twice larger than the 5 PPI metal foam is required to ensure the existence of fluid flow in the porous structure, reducing the restrictions from the ligament structures (Sauret, Abdi, and Hooman, 2014). Furthermore, this study manipulated the pore sizes to investigate the effect of flow resistance, pressure drop, and flow velocity in the partially filled configuration. Figure 3.4 shows a comparison of 3D printed foam in the original size of 5 PPI with 2 scale enlargements. The dimensions of 3D printed open-cell foams were created by copying, pasting and cutting the initial size of the porous structure until the required dimension is met. The base size of every foam sample in this research is 99 mm (length) × 94 mm (width), following the base area of the test section. Only the foams' height, $h_f$ were manipulated from 30 to 90 mm to create a partially filled configuration as shown in Figure 3.5. The partially filled configuration means that the height of the 3D printed foam is smaller than the channel (test section) height, $h_c$ and partly filled the test section area in a normal (y-axis) direction.

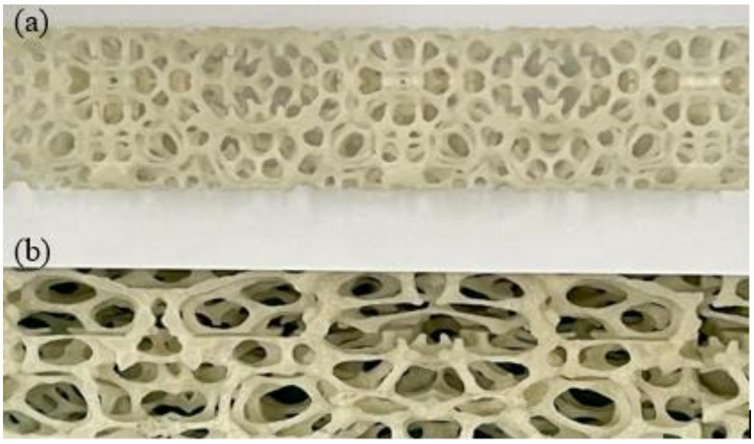


Figure 3.4: Comparison of 3D printed open-cell foam (a) Original size of 5 PPI and (b) 2 scale- twice of 5 PPI size

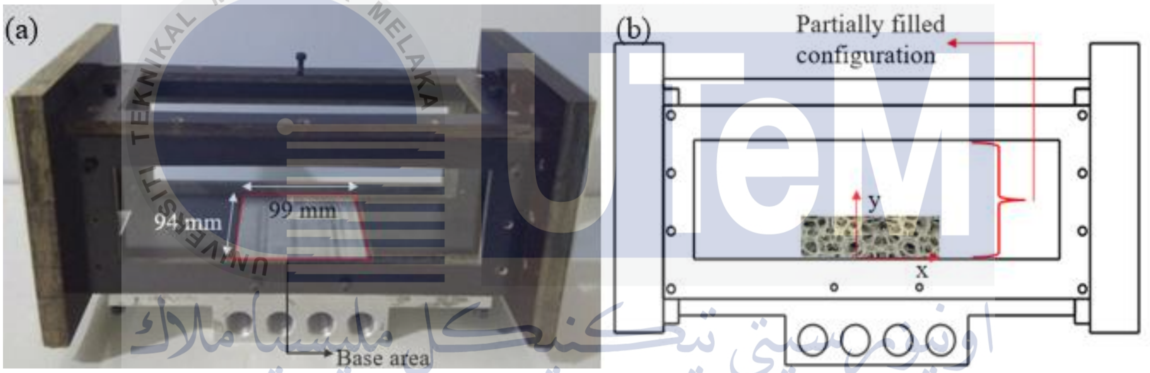


Figure 3.5: (a) Base area of channel, and (b) Partially filled configuration



The minimum height of 3D printed foam was set from 30 mm, considering the noticeable effect of the porous structure can be only seen at this height (Shikh Anuar et al., 2018) and the rest of the heights were manipulated by increments of 30 mm to understand the effects of foam heights on the fluid behaviour in the free stream region. A study by Lu, Zhang, and Yang (2016) also stated that the open-cell foam with a lower height with a blockage ratio < 0.7 has less than 20% of total flow inside the porous region even though it has porosity up to 90%. If the foam height is higher than 20 mm, e.g., 30 mm, the fluid would be forced to flow inside the complicated structure of porous foam (Hamadouche et al., 2016).

A streamlined result from a numerical study by Yerramalle, Premachandran, and Talukdar (2021) that consists of a setup with different blockage ratio from 0.3 – 1.0 showed the existence of fluid flow inside the porous structure. In this research, a fully filled channel ($h_f = h_c$ = 100 mm) was also considered in the experiment to investigate the permeability of the 3D printed foam using Forcheimmer's equation. The foam configurations are presented as a blockage ratio, $h_f/h_c$, which are 0.3, 0.6 and 0.9 for the partially filled channel and 1.0 for a fully filled channel. The details of 3D printed foams are listed in Table 3.1.

Table 3.1: Dimension of 3D printed open-cell foams

| Scale size | Base Size (mm) | Height (mm) |
|---|---|---|
| 2 scale | 99 × 94 | 30; 60; 90; 100 |
| 4 scale | | |
| 6 scale | | |



### 3.2.2 Three-dimensional (3D) printing technologies

This research used 3D printing techniques to produce and replicate the complicated structure of the open-cell foam. Nowadays, there are various types of 3D printing technologies available which can produce parts with different types of material, for example, FDM and SLS for plastic material while Direct Metal Laser Sintering (DMLS), Electron Beam Melting (EBM), and SLM for metallic material. However, a production through a metallic 3D printer is restricted as some metallic materials have high reflectivity which can cause porosity and it is considered as an expensive equipment (Wan et al., 2021). The AM technology is more advantageous than the conventional method, since it is cost efficient, consuming less time, and the parts can be produced with various types of material. Since, the present research does not focus on the application of heat transfer, the 3D printers using plastic material are considered which focused on the production of complicated porous structure with a smooth surface finish.

The 3D printed open-cell foams were produced using two different 3D printing technologies; (1) FDM and (2) SLS as shown in Figure 3.6. Both FDM and SLS were used as a part of the reverse engineering method to produce 3D printed foams using the restructured images. The FDM is a manufacturing method via extrusion where it works by ejecting melted filament, layer-by-layer onto the forming stage. The printer’s nozzle moves along according to the foam structure until the layering process is completed and finished (Sachlos et al., 2003). However, supports (external structures) would be needed in between the structures to maintain the form and shape of the porous structure while supporting overhanging or unconnected features. It was conducted through trial and error due to the randomization of pore structures and different pore sizes where the support structures were attached to the foam structure during slicing process in pre-processing stage. Later, the supports need to be removed manually from the 3D printed foam to ensure there is no blockage in the pores.

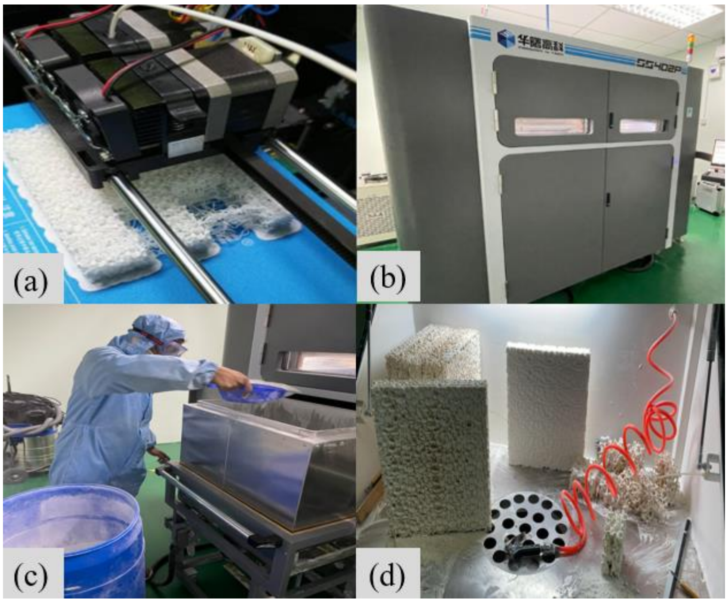

Figure 3.6: (a) FDM processing, (b) SLS printers, (c) SLS pre-processing and (d) SLS post-processing

Meanwhile, the SLS printer consists of four main chambers: (1) feeding chamber, (2) building chamber (printing platform), (3) collector chamber and (4) powder overflow chamber. The building chamber has a maximum printing area of 320 × 320 × 380 mm where it can be loaded with all twelve foam samples arranged with gaps between them. This research used nylon powder (FS3300PA, Farsoon), which was dispersed on a printing platform in a very thin layer to create a powder bed. The powder was bonded together to form a solid structure of foam ligaments through laser sintering. The powder bed that is fully self-supported provides great convenience since it allows a high overhanging angle (0 to 45º from the horizontal plane) during the printing process. However, it is important to note that uneven scattering and insufficient amounts of powder on the printing platform may affect the foam structure and its surface. Thus, a correct amount of powder must be carefully set to ensure all of the platform areas are covered. The left behind or unfused powder inside the porous structure may also become the support. The SLS produces the foam sample through layer-by-layer printing where the platform can automatically move down to form a new layer of powder on top. The powder was sintered until a sample was formed. The printing process to prepare the foam samples took three days, including the cooling duration. The duration of printing varies depending on the size and complexity of the foam samples. The printed foam was blasted using high-pressure air to clean and remove the unfused powder.

The properties of 3D printing materials used in the SLS and FDM are shown in Table 3.2. In term of the tensile strength, the PLA is superior in tensile strength but requiring a very high melting temperature compared to the nylon. The PLA is selected for FDM materials since it may had a superior strength and commonly used in the technology. However, for the SLS technology, the material in powder form is limited to only nylon.

Table 3.2: Properties of 3D printing materials

| Materials | Melting point (°C) | Tensile strength (MPa) | Elongation at break (%) | Reference |
|---|---|---|---|---|
| Polylactic Acid (PLA) – FDM | 200 - 240 | 59 | 7 | Farah, Anderson, and Langer (2016) |
| FS 3300 PA (nylon) – SLS | 183 | 46 | 36 | Khudiakova et al. (2020) |

This research also used alluminium open-cell metal foam to compare with the results of 3D printed foam, made of nylon. The open-cell metal foam was obtained from Beihai composite (n.d) which is the same as the 3D printed foam. The specific physical properties of open-cell metal foam have been tabulated in Table 3.3. It is shows that the porosity of 30 PPI foam is slightly higher than 10 PPI but lower in permeability. It is expected that the 30 PPI would have a lower permeability since the structure has a smaller pore size and more ligament restrictions.

Table 3.3: Physical properties of open-cell metal foam

| Physical properties | ERG Aerospace | Beihai Composite | |
|---|---|---|---|
| Pore diameter, PPI | 5 | 10 | 30 |
| Ligament diameter, $d_l$ (m) | 0.00113 | 0.00044 | 0.00027 |
| Pore diameter, $d_p$ (m) | 0.00577 | 0.00256 | 0.00087 |
| Porosity, $\varepsilon$ (–) | 0.86 | 0.91 | 0.94 |
| Permeability, K $\times 10^{-7}$ ($m^2$) | 0.02 | 1.65 | 0.37 |
| Foam height, $h_f$ (m) | 0.02 | | |
| Blockage ratio, $h_f/h_c$ | 0.2 | | |
| Foam length, $L_f$ (m) | 0.093 | | |

### 3.2.3 Surface topology and roughness test of 3D printed open-cell foam

The microstructure of the 3D printed foam was examined using a USB Wi-Fi microscope (RS Pro; 1280 x 1024 pixels and up to 200x magnification). The microscope has been paired with Mic-Fi (mobile application) to record and control the process of capturing the microstructure image. It can also be used to make a measurement on the image, e.g., pore and ligament diameters. The images of ligament surfaces that been captured are also required for surface roughness evaluation. The captured images should have a wide and flat surface area to avoid inaccuracy in examining the surface roughness as shown in Figure 3.7. The roughness evaluation was conducted using Image J software, which presented as a profile plot; gray value against distance (pixel). The gray value is commonly found in the surface roughness evaluation where it indicates the value of each pixel that represents an amount of light. Thus, the software is used as a gauge for generalization in comparing two or more different foams. This approach is utilized due to limitations of the porous sample; (1) surface area to evaluate too small and (2) foam material is incompatible with other apparatus such as Scanning Electron Microscope (SEM) and profilometer. By subtracting the background image, the surface roughness could be determined thoroughly. The dissipation of nylon powder on the foam produced using the SLS method is shown in Figure 3.7 (b), which is clearly seen after the background image of the surface was subtracted. The powder dissipation is formed since the laser did not sinter the remaining powder, which then accumulated on the foam surface. The powder dissipation can be removed completely through finishing and deep cleaning. The images were also set up at 32 bits for post-processing to obtain clear images of the ligament surface and the roughness on the surface is highlighted in Figure 3.7 (b). The plot profile, surface plot and average roughness, Ra can be generated by using the "analyze function" in the Image J software.

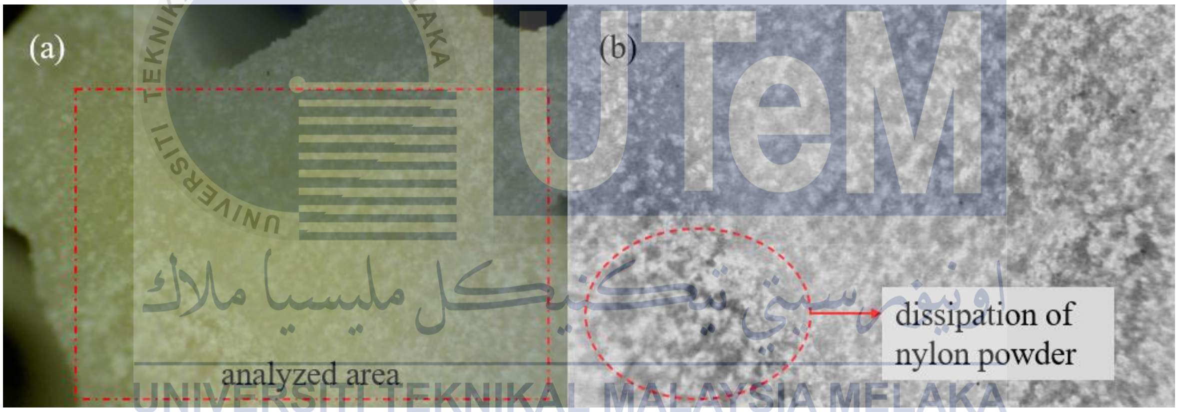




Figure 3.7: (a) Image captured by microscope and (b) Processed image from surface roughness test

### 3.2.4 Determination of open-cell foam properties

The classification of 3D printed foam properties is required after the production stage. The foam properties were obtained through measurement or calculation using the existing equations in the literature. For example, the pore diameter and ligament diameter can be measured using a microscope and special small rulers from the manufacturer. Meanwhile, the porosity and permeability of the 3D printed foam can be calculated using the experimental data. The porosities of the 3D printed foams were determined using a rectangular container with the cross-sectional area, A is 0.151 m (width) X 0.109 m (length), filled with water with a height of 0.12 m. The foam was immersed in the container where the water level was observed and measured. The change in the level of water ($\Delta h$) gives the volume of water displaced by the solid structure of the foam, which was equivalent to the volume of the solid structure ($V_{porous}$). The void volume ($V_{void}$) can be calculated by subtracting $V_{porous}$ from a whole solid block volume (with the same dimensions as the porous foam). It can be calculated as:

$$V_{porous} = A_{container}\Delta h \tag{3.1}$$

$$V_{void} = V_{total} - V_{porous} \tag{3.2}$$

The porosity can be calculated based on the ratio of $V_{void}$ with $V_{total}$ as listed in Equation (3.3) (Alomair and Tasnim, 2018). Note that, $V_{total}$ was the total volume of the foam (including the voids or pores).



$$\text{Porosity, } \varepsilon = \frac{V_{void}}{V_{total}} \tag{3.3}$$

The permeability equation of the foam can be expressed using the Forchheimer equation, as shown in Equation (2.6) (Bhattacharya, Calmidi, and Mahajan, 2002), which can be also expressed in Equation (3.4).

$$\frac{\Delta P}{\Delta l} = aU + bU^2 \tag{3.4}$$

Note that, the permeability and inertial coefficient, *f* can directly be determined using Equation (3.5) as a result of solving Equations (2.6) and (3.4).

$$K = \frac{\mu}{a}, \quad f = \frac{b\sqrt{K}}{\rho} \tag{3.5}$$

An analysis on a plot of pressure drops per unit length, ΔP/Δl versus velocity, U must be done to determine the coefficients a and b, in Equation (3.5). The analysis should yield a fit with $R^2 > 99.9\%$ for all pore diameter cases to be considered statistically correlated (Bhattacharya, Calmidi, and Mahajan, 2002).

## 3.3 Experimental setup and calibration

In this research, flow visualization and pressure drop investigation was conducted in a close loop wind tunnel. A hot wire anemometer (HT 9830; accuracy: ± (1% + 1d)) was used to measure flow velocity at five different regions: inlet, upstream, middle, downstream and interface regions. The upstream and downstream regions were considered to characterize the flow behaviours in the test section (rectangular channel) and estimate the flow condition in the partially filled section with 3D printed foam. The pressure drops across the partially filled section were also measured. The slip velocity at the interface between the free stream and porous regions would be investigated through the measurement of local velocity. This research focuses on experimental work using a hot wire anemometer and the results would be validated using CFD analysis.

### 3.3.1 Test rig

A small scale wind tunnel can be used for a detailed experimentation study of fluid phenomena in thermal-fluid systems (Cengel and Cimbala, 2019). The wind tunnel consists of a centrifugal fan, frequency inverter, channel and flexible duct as shown in Figure 3.8. The centrifugal fan (AIRSPEC; Model ARC 629) can provide air flow (inlet air) up to 7.0 m/s into the channel test section of the wind tunnel. The fan is connected to an inverter (TECO Inverter F510 – 4 kW), which is used to control the three-phase induction motor of the fan and manipulate the frequencies to have inlet air velocities of 1.0, 3.0, and 5.0 m/s in the channel. The frequency selection is supported with reliable standard ASTM D 6011-96, that requires the wind tunnel to operate in a standard range of anemometer measurement which is at least 0 –10 m/s. The blower frequency was determined by trial and error by placing the hot wire anemometer inside an empty wind tunnel. Since the maximum frequency of blower is 50 Hz, the air velocities (0 – 5.5 m/s) can be determined by manipulating the blower frequency (0 – 50 Hz).



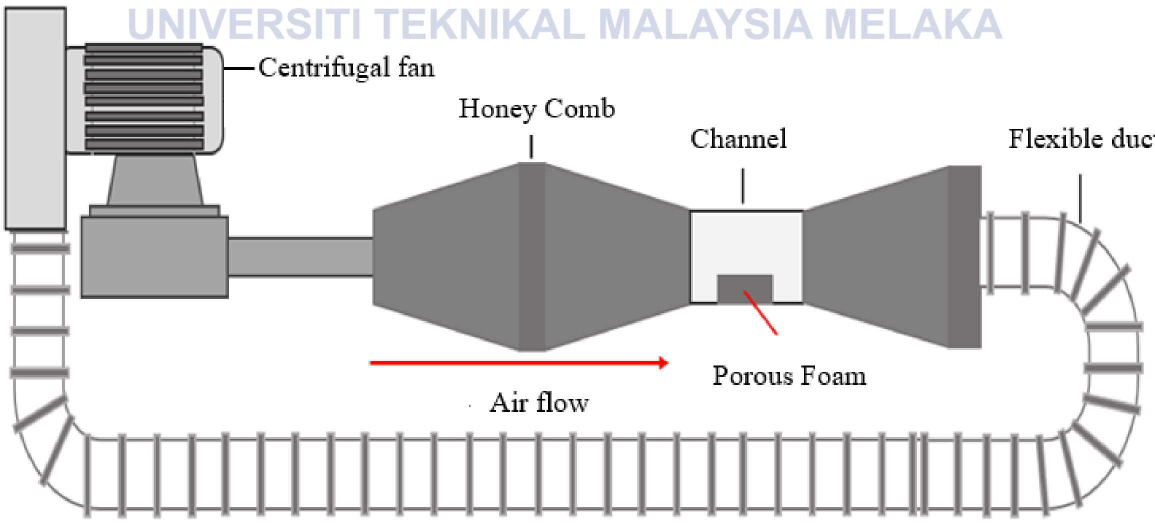


Figure 3.8: Schematic diagram of close-loop wind tunnel

The air from the fan passes through a diffuser, which is installed with a honeycomb to stabilize the flow before entering the channel. The channel size is 0.10 m (H) × 0.10 m (W) × 0.35 m (L) and its top wall is designed to be easily opened for the installation of foam samples. The top wall of the channel features multiple holes that enable the use of sensors and hot wire anemometer probes. In addition, the channel's side and top walls are prepared from transparent materials for a better observation of the sensor position. The experimental work was conducted by placing a foam sample inside the test section. The test section had a slot at the centre to fix the placement of the foam sample. The foam was designed to the same size and shape of the slot. To make sure the flow could not move the foam, the bottom part of the channel was attached with double-sided tape. The 3D printed foam was designed to tightly sit between two walls, rigidly positioned inside the channel. Thus, only three surfaces (sides) of the foam were directly exposed to the airflow, which were : (1) the frontal area, (2) the top or interface, and (3) the back surface.

The experiment started by measuring the air temperature inside the wind tunnel to find the correct fluid properties such as air density, $\rho$ and viscosity, µ. The air temperature was measured using a Type-K thermocouple that was connected to a data logger (Pico, TC-08). The Reynold number, $Re_{Dh}$ can be calculated using Equation (3.6), whereas the hydraulic diameter of the channel can be determined using Equation (3.7). Note that, A and p in Equation (3.7) are the channel cross-sectional area (inlet), and perimeter of the cross-sectional area, respectively. The flow in the channel is turbulent with the range of $Re_{Dh}$ from $5.86 \times 10^3$ to $2.93 \times 10^4$, which depends on the inlet velocities, $U_{inlet}$ used in the experiments. The turbulent flow regime and the result of velocity profiles of an unloaded channel (without foam) could be used as a reference case for experiments with 3D printed foams.

$$Re_{Dh} = \frac{\rho.U_{inlet}.D_h}{\mu} \tag{3.6}$$

$$D_h = \frac{4A}{p} \tag{3.7}$$

The friction factor, *f* of the unloaded channel can be calculated using the measured pressure drop and the Darcy-Weisbach equation in Equation (3.8). The maximum friction factor value in the channel is 0.62. Note that $\Delta P$, g, L and $U_{inlet}$ in Equation (3.8) are the pressure drop, gravitational acceleration, channel length, and inlet velocity, respectively.

$$f = \frac{2\Delta P.D_h.g}{LU_{inlet}^{2}} \tag{3.8}$$

### 3.3.2 Experimental setup

The flow velocities were measured in five regions, at different positions in order to comprehend the flow behaviours in the channel. Different types of hot-wire anemometers, Sentury, ST-732; (accuracy: ± (0.03+3%)) and Omega, HHF 1000; (accuracy: ± (0.5%)) were used for purpose of calibrating and validating the experimental data. Meanwhile, the pressure drops were measured across the foams in the partially filled section using a pressure sensor (Sensirion, 500 Pa; Accuracy: ±3%). The pressure taps were installed at a close distance near the edges of the foam, with a gap distance of 99.0 mm as shown in Figure 3.9, and the velocities measurement points are shown as vertical red-dash lines. The pressure sensor was connected to a data logger and the results are presented in the averaged values in Pascal (Pa). The same measurement techniques using a hot-wire anemometer and pressure sensors were used to investigate the unloaded condition and fully filled channel for wind tunnel flow characterization and permeability test. Different blockage ratios were created in the partially filled experiments by changing the foam heights.

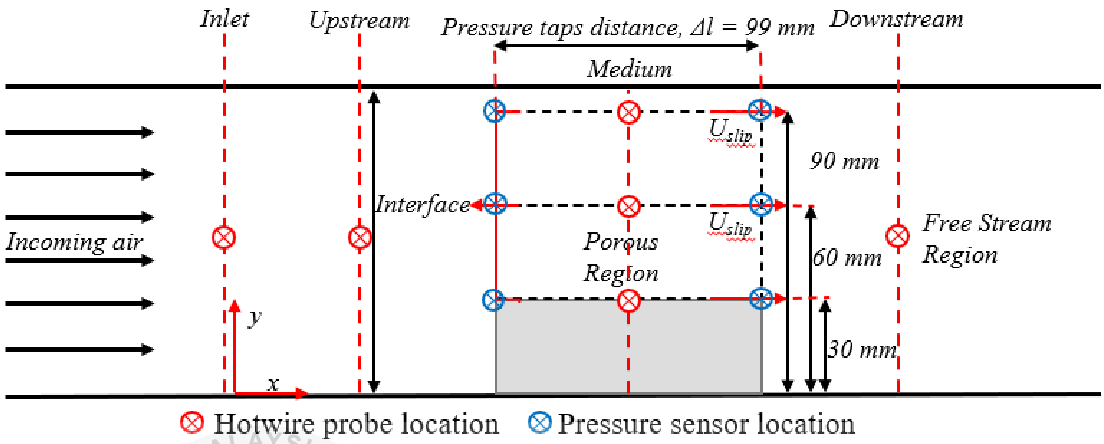


Figure 3.9: Schematic diagram of channel with measurement points

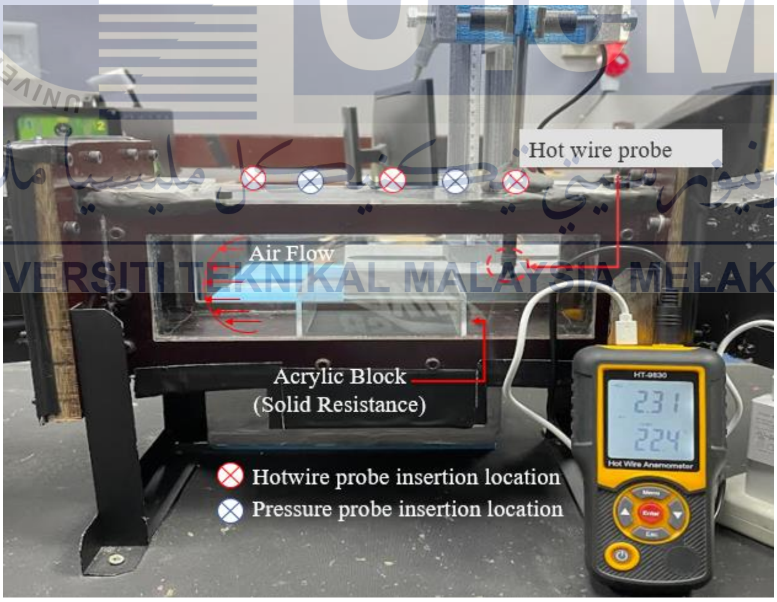


Figure 3.10: Acrylic solid block setup in the channel



The acrylic solid block was used as a solid resistance to the fluid flow in the channel. It can be used to study the effects of porous structure on fluid behaviours and determine the wind tunnel's limitation in terms of pressure drop effects. Hence, the investigation using the solid resistance was conducted at the same setup as the porous foams.

### 3.3.3 Instruments calibration and validation

The calibration of the instruments was conducted to configure the desired air velocities in the wind tunnel and the setup was checked by manipulating the frequencies using the inverter. The air velocity was set at 1.0, 3.0 and 5.0 m/s at the setting frequencies of 10, 22 and 46 Hz. For the calibration with the hotwire anemometer, it was placed at the inlet region and 50 mm from the bottom wall (middle section of the channel height). The air velocity (due to the turbulent regime) is expected to be constant across the channel height. Meanwhile, the experiments started with an unloaded wind tunnel to be used as a reference in a later investigation for a partially filled setup. The velocity profiles of the unloaded wind tunnel are shown in Figure 3.11. The velocity profile shows a slightly bigger difference at the lowest inlet velocity of 1.0 m/s, especially at the entrance of the channel. Similar velocities can be achieved at $U_{Inlet}$ = 3.0 m/s and 5.0 m/s, regardless of the streamwise measurement locations from the entrance of the channel (inlet) towards the outlet, suggesting a uniform flow in the channel Figure 3.11 also shows that the velocity profiles are asymmetric, unlike the ideal turbulent velocity profile. These asymmetrical profiles should be anticipated since different materials were used at the bottom wall ($h/h_c = 0$) and top wall ($h/h_c = 1.0$), made of aluminium and Bakelite with borosilicate glass, respectively.

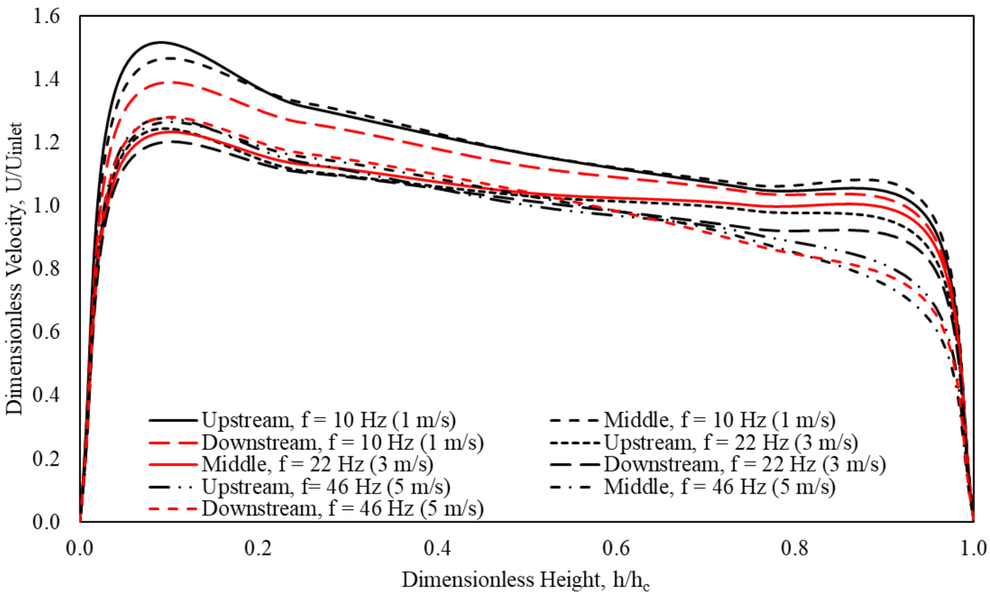


Figure 3.11: Velocity profiles in the unloaded channel with different frequencies

The unloaded wind tunnel experiment also shows a small pressure drop in the channel, with the maximum measured value is 37.77 Pa, occurring at an inlet velocity of 5.0 m/s. The collected data are presented in terms of pressure drop per unit length, ΔP/ Δl on the y-axis, while the inlet velocity, $U_{Inlet}$ on the x-axis as shown in Figure 3.12. The pressure drops increase with the inlet velocity as one would expect, and it is directly proportional to the air velocity inside the channel. The installation of solid blocks in the channel was also done to investigate the capability of the wind tunnel to operate with loaded cases. The result shows that the pressure drops can be increased up to 1857.58 Pa with the addition of 60% of blockage in the channel. Using a higher blockage would change the shape of the flexible duct that was connected to the channel outlet, obstructing the flow in the closed-loop wind tunnel. Hence, the wind tunnel is only operable with 40% clearance at the channel.

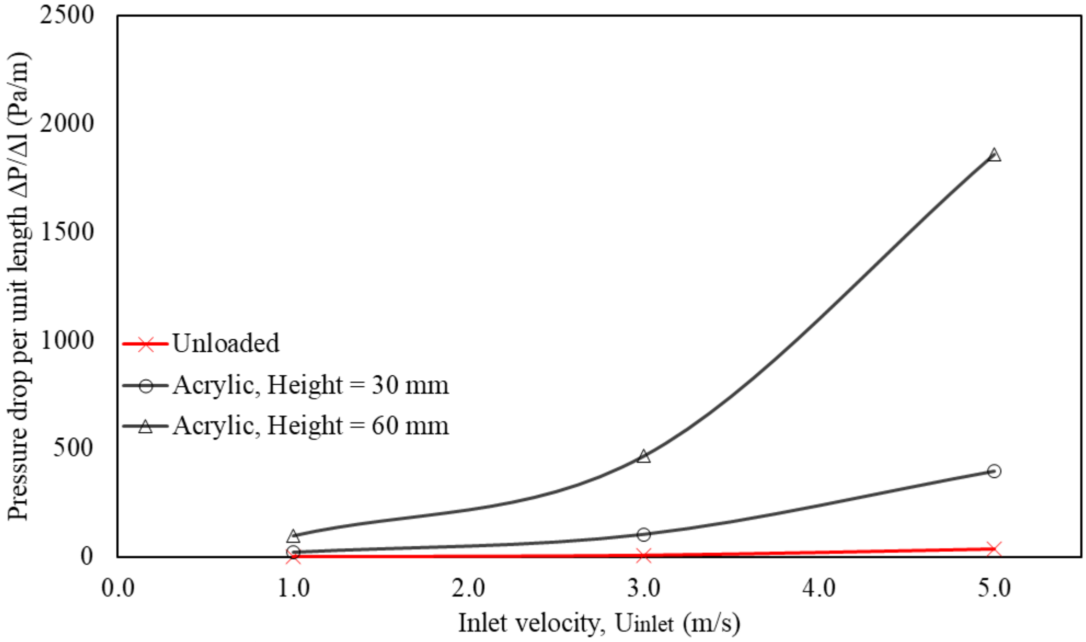


Figure 3.12: Pressure gradient for unloaded channel and loaded channel with solid block

### 3.3.4 Uncertainty calculation for experimental works

The uncertainty analysis was performed in this research to increase the accuracy of experimental data while minimizing errors. To ensure accuracy and repeatability, three sets of experimental data were collected for each foam sample using the same setup, and the average values were calculated. This approach was employed for both velocity and pressure drop experiments. The averaged value is determined through the general formula presented in Equation (3.9).

$$\bar{x} = \frac{1}{n}\left(x_1 + x_2 + x_3 + \cdots + x_n\right) \tag{3.9}$$

$$\sigma_x = \sqrt{\frac{1}{n-1}\sum (x_i - \bar{x})^2} \tag{3.10}$$

Note that in Equations 3.9 and 3.10, the variable n represents the number of repeated measurements, which must be at least three. The deviation values that were calculated from the averaged values are defined as the experimental error where the standard deviation, σ is used in estimating the variances as shown in Equation (3.10).

## 3.4 Regression analysis and model validation

Regression analysis was conducted to identify which dimensionless variables have more significant effects on the slip velocity. This analysis allows for the identification of the most significant factors while disregarding any insignificant ones. A comprehensive dataset is required, which can be obtained by collecting data from various 3D printed foams and metal foams at different inlet velocities. The regression analysis was conducted using Excel software. The analysis was set at a 95% confidence interval, with the P-value < 0.05 and the adjusted $R^2$ should be in an acceptable range, larger than 0.7 (Hajiahmadi, Elyasi, and Shakeri, 2019). Since there is no consensus in the literature regarding the characteristic length of open-cell foam, the research was carried out using a trial-and-error methodology to determine which parametric model and experimental data had the best conformity. The values of slip velocity from the proposed model were compared with the experimental results and simulation, as discussed in section 4.5.2.

### 3.4.1 Parameter selection

In investigating the open-cell foam in a partially filled channel, there are many parameters that need to be considered, from the foam's physical and geometrical properties (such as foam length, foam height, pore and ligament diameters), as well to the channel dimensions and operating condition (a range of inlet velocities). The foam properties were very important to be considered in the selection of the variables since each of the parameters would determine the resistances to the fluid flow. Meanwhile, the porosity and permeability stimulate the rate of fluid in the porous region. At the same time, all the parameters from the BJ theory should be selected as well, considering the foam itself is a kind of porous medium, and those parameters are relevant to this research. The slip velocity was considered as a dependent variable, and the rest of the parameters (independent variables) were assumed to have influences on the slip velocity. A dimensional analysis using the Buckingham $\pi$ theorem was conducted to obtain a relevant list of dimensionless groups. The dimensionless groups that been obtained from the dimensional analysis were used to compute a predicted model of slip velocity, where these processes are illustrated in the flow chart shown in Figure 3.1.

This research aims to formulate the slip velocity at the interface region that may depend on a few parameters. Considering there is a lack of investigations on the effect of various parameters on slip velocity, the formulation of a new model that may be beneficial in determining the slip velocity with a variety of pore diameters would be helpful. Dimensional analysis is very useful to generate dimensionless parameters to design simpler experiments (physical or numerical) and in reporting the experimental result (Cengel and Cimbala, 2019). Buckingham $\pi$ theory is widely used in the fluid mechanics field to determine the possible dimensionless groups that form respective parameters that may influence parameters of interest, in this research, the slip velocity. Thus, the most efficient slip velocity predicted models at the interface region were determined by regression analysis where the most relevant and acceptable parameters are selected from the dimensional analysis. Moreover, the proposed slip velocity model may be helpful in estimating the slip velocity compared to past studies. For instance, Beaver-Joseph, Ochoa-Tapia-Whitaker only conclude in some theories and define the slip coefficient at the boundary where there is no finding for the exact value of slip velocity. Thus, those parameters in the slip velocity models for different types of porous media were also considered when developing the dimensionless groups in this research.

The dimensional analysis technique utilized the similarity law and the principle of dimensional homogeneity (Hajiahmadi, Elyasi, and Shakeri, 2019). In similarity law, there are three necessary conditions to complete the similarity between a prototype and a model (geometric similarity, kinematic similarity, and dynamic similarity). The geometric similarity defines the model must be in the same shape as the prototype but could be different in scale and size. The geometric similarity was considered achievable since the foam used the same basic structure but with variations in pore diameter, ligament size, and thickness. The kinematic similarity specifically concludes that the magnitude of a model must be in the same relative direction as the prototype. In this research, all necessary conditions were achieved in a general flow field, including the crucial kinematic condition of ensuring that the magnitudes of the variables are the same. Lastly, the dynamic similarity was achieved when all forces in the model flow scale by a constant factor corresponding to the forces in the prototype.



### 3.4.2 Dimensional analysis of slip velocity

The Buckingham π theorem was used to determine the dimensionless groups created from the independent parameters that were related to the dependent parameter. The relationship between the slip velocity and the related parameters can be determined from Equation (3.11),

$$U_s = f(U_{inlet}, U_0, \rho_{fluid}, \mu_{fluid}, K, \Delta P/\Delta l, h_c, d_p, d_l, h_f) \tag{3.11}$$

where "$U_s$" is the slip velocity, U is the air velocity that was measured in the wind tunnel, "$\rho_{fluid}$" is the air density, and "$\mu_{fluid}$" is the dynamic viscosity of air. The total number of independent and dependent parameters is n = 11 which is presented in Table 3.4 and the dimensionless groups can be derived into 8 π groups from the main dimensions, m = 3 by considering the reduction factor "k = n - m". Three parameters were selected as the repeating variables, while the rest were treated as independent parameters.

Table 3.4: Dimensional matrix for independent and dependent parameters.

| Dimension | $U_s$ | $U_{inlet}$ | U | $\rho_{fluid}$ | $\mu_{fluid}$ | $h_c$ | $d_l$ | $d_f$ | K | $\Delta P/\Delta l$ |
|---|---|---|---|---|---|---|---|---|---|---|
| M | 0 | 0 | 0 | 1 | 1 | 0 | 0 | 0 | 0 | 1 |
| L | 1 | 1 | 1 | -3 | -1 | 1 | 1 | 1 | 2 | -2 |
| T | -1 | -1 | -1 | 0 | -1 | 0 | 0 | 0 | 0 | -2 |

The steps in determining the dimensionless groups are described below. The first π group has been defined in Equation (3.12) which simplify the understanding of parameters and method that have been used in this research.



$$\pi_1 = U_s U_{inlet}{}^a \rho_{fluid}{}^b h_c{}^c \tag{3.12}$$

Then, the selected parameters concerning the π groups as in Equation (3.2) were converted to the main dimensions (M, L, T) as listed in Equation (3.13).

$$\pi_1 = (L/T)(L/T)^a (M/L^{-3})^b (L)^c \tag{3.13}$$

A dimensionless number and homogeneity are shown in Equation (3.14). Thus, the powers of the dimensionless matrix (M, L, T) have been equated and solved using the simultaneous equation to solve the unknown.

$$(M^0L^0T^0) = (L/T)(L/T)^a(M/L^{-3})^b(L)^c \quad (3.14)$$

Finally, the dimensionless group was obtained by deducing Equation (3.13) and incorporating all the unknowns. The final form of the π group can be shown in Equation (3.15). Note that the final form of the π group should have a total dimensional matrix equal to zero, consistent with the dimensionless convention.

$$\pi_1 = U_s/U_{inlet} \quad (3.15)$$

The dimensionless groups obtained from the analysis are listed in Table 3.5, where $\pi_1$ is the ratio of slip velocity with the inlet velocity, $\pi_2$ is the ratio between fixed air velocity (measured in empty channel cases) with the inlet velocity, $\pi_3$ is the Reynold number with the selected characteristic length is foam height, $\pi_4$ is a dimensionless quantity made of various parameters, $\pi_5$ is the blockage ratio, $\pi_6$ is the ratio of pore diameter with channel height, $\pi_7$ is the ratio of ligament diameter with channel height and $\pi_8$ is the ratio of surface area at the free stream region with channel height.

Table 3.5: Dimensionless π groups

| $\pi$ -group | Parameter |
|---|---|
| $\pi_1$ | $\frac{U_s}{U_{inlet}}$ |
| $\pi_2$ | $\frac{U}{U_{inlet}}$ |
| $\pi_3$ | $Re_{hc}$ |
| $\pi_4$ | $\frac{(\frac{\Delta P}{\Delta l})h_c}{U_{inlet}^2 \rho}$ |
| $\pi_5$ | $\frac{h_f}{h_c}$ |
| $\pi_6$ | $\frac{d_p}{h_c}$ |
| $\pi_7$ | $\frac{d_l}{h_c}$ |
| $\pi_8$ | $\frac{K}{h_c^2}$ |



## 3.5 Numerical studies on fluid flow behaviours

To further comprehend the experimental data presented in the preceding section, a CFD analysis was conducted based on the same setup in the channel. The numerical data from the CFD simulation were used to verify the experimental data and slip velocity model. In the research, a 3D simulation is not conducted due to the complex mesh structure of the foam images. Configuring the porous structure within the simulation is challenging and requires advanced technology for processing. However, the 2D simulation is easier to be completed with lesser computational cost. Moreover, the channel setup with a foam block can be considered symmetrical due to its rectangular design. This research focuses on obtaining averaging data in the free stream region, instead of localized data within the porous structure of the foam. Hence, the 2D simulation is preferred instead of 3D simulation. The pore diameter was set, according to the averaged pore size of 3D printed foam, that was produced using Selective Laser Sintering (SLS) technology.

### 3.5.1 Computational Fluid Dynamics (CFD) model construction

This research used Ansys Fluent 2022 R2 software to conduct CFD analysis of partially and fully filled channels with a porous medium. The 2D model was taken as initiative instead of 3D model mainly due to the difficulties in computational the real structure of open-cell foam from CT-scan. Since the CT-scan process produced a translation of the images from the porous foam in meshing form, the process of declaring the domain of the porous region cannot be proceeded which may result in an error in reading the file. The 2D domain was created based on the foam sizes from experimental studies. Two rectangle areas were generated separately in different sketches, where sketch 1 represents the channel while sketch 2 represents the porous foam as shown in Figure 3.13. Separate bodies were created for each sketch by defining the material. The sketch 1 was occupied with fluid and frozen, while sketch 2 was defined with specific material properties of foam, making it easier to be analyzed. The sketches with '2 part, 2 bodies' were then merged to become '1 part, 2 bodies' by highlighting both sketches to avoid the contact region between the created bodies. Both regions can be assumed as homogenous in sizes, dimensions and shapes since the fluid is moving in a constant size channel and the pore cells in the porous region are hard to determine as it is randomly oriented (Sauret, Abdi, and Hooman, 2014). Since the sketches for the porous structure only have a rectangular surface, the porous structure properties such as porosity will then be defined in another part of numerical studies; cell zone condition. The blockage ratio between the porous foam and the channel height is the same as in the experiments; 0.3, 0.6 and 0.9 for the partially filled channel. The geometry sketches can be seen in Figure 3.13 while the dimensions used in the simulation are tabulated in Table 3.6.

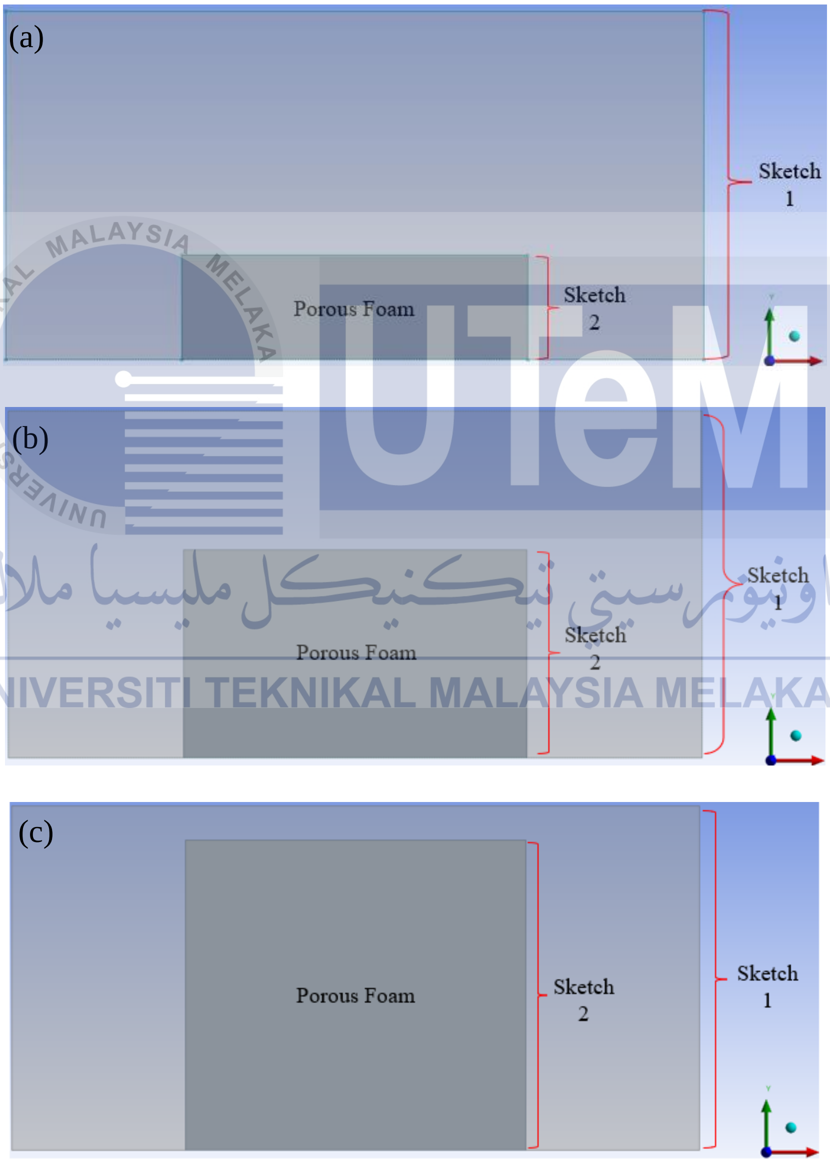




Figure 3.13: Channel setup with different blockage ratios: (a) 0.3, (b) 0.6, and (c) 0.9

Table 3.6: Dimensions of the channel and porous medium

| | Pore diameter (scale) | Porous foam height (mm) | Porous foam length (mm) | Channel Dimension (mm) |
|---|---|---|---|---|
| Partially Filled | 2, 4, 6 | 30, 60, 90 | 99 | 94 x 100 x 200 |
| Fully Filled | | 100 | | |

After sketching, the CFD analysis continued with the meshing process. For every sketch, the smoothing was set to ‘High’. In addition, the Map Face Meshing and Refinement were set to ‘3’ on the two rectangular parts of the 2D model that had been drawn earlier while the default growth rate of 1.2. Once the meshing setup was done, a computational grid line would be generated for both rectangular parts. After completing the meshing process, each part was assigned a name such as ‘Inlet,’ ‘Outlet,’ and ‘Wall’ to define their parameters in the boundary condition settings.



### 3.5.2 Grid independence test for the channel and porous medium



A grid independence test was performed to check the sensitivity of the analysis solution with a specific grid size and to obtain the optimum number of grids (Jadhav et al., 2021). The objective is to determine the optimum point for more precise and reliable solution results by using smaller cell sizes and finer grids. Some parameters, such as too coarse mesh, high skewness, large aspect ratio, and inappropriate boundary layer will impact the solver's performance and accuracy. The incompatible grid size may cause a significant influence on the analysis solutions, which then leads to the requirement for a mesh sensitivity analysis by determining the necessary meshing elements. This sensitivity analysis includes refining the mesh to a preferred solution. It is acceptable when the mesh refinement is not affecting the solutions anymore. The configuration setup in the CFD analysis (for all blockage ratios) was tested with three mesh independence models. In the meshing process, the refinement was set at 1 until 3 to configure the most suitable grid size for all cases. By increasing the number of cells, the grid size becomes smaller as shown in Figure 3.14. Table 3.7 shows the grid independence test results, and finally, refinement with '3' is chosen to be used in all analyses due to insignificant effects on the computational cost.

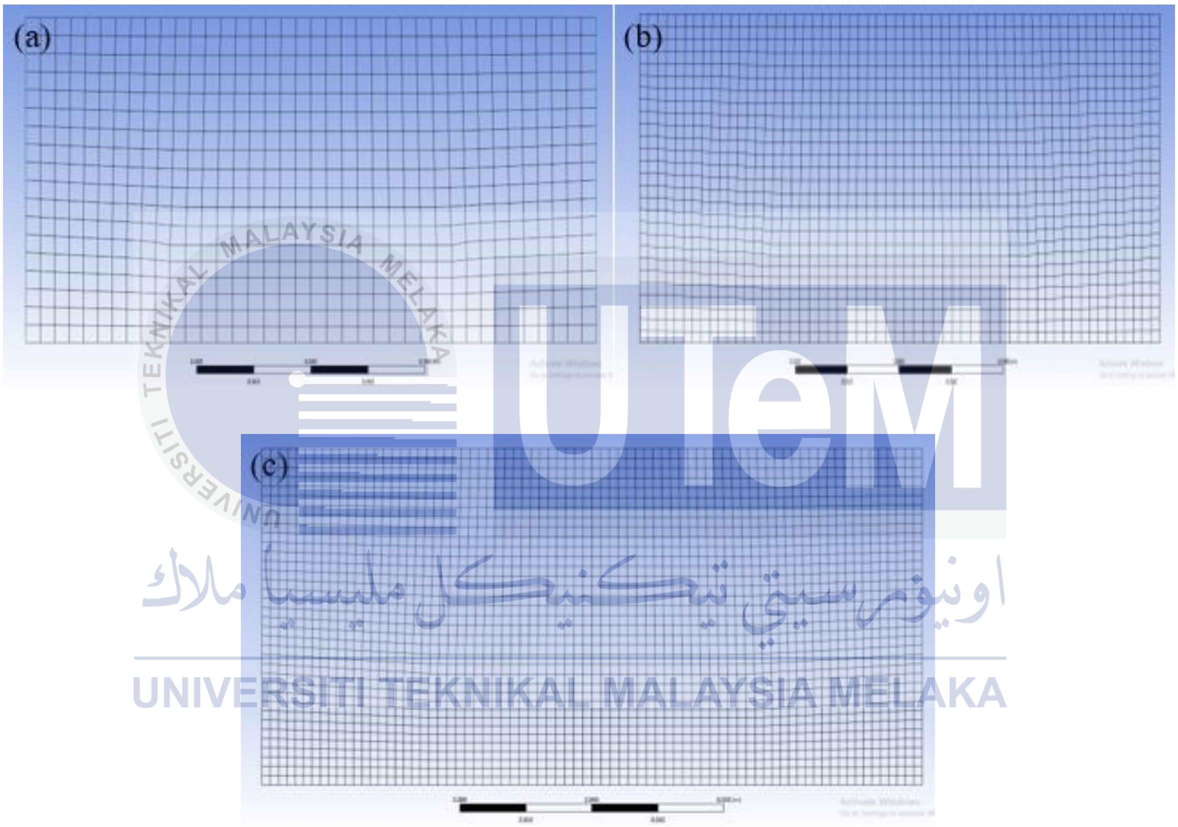




Figure 3.14: Meshing of 2 scale foam with different grid independence test: (a) Test 1, (b) Test 2 and (c) Test 3

Table 3.7: Parameters of grid independence test for 2 scale foam

| Parameters | Grid Independence Test 1 | Grid Independence Test 2 | Grid Independence Test 3 |
|---|---|---|---|
| Refinement | 1 | 2 | 3 |
| Nodes | 741 | 1624 | 2849 |
| Element | 684 | 1539 | 2736 |
| Velocity, $h_f$ = 30 mm | 3.11 | 3.12 | 3.12 |
| Velocity, $h_f$ = 60 mm | 2.90 | 2.92 | 2.92 |
| Velocity, $h_f$ = 90 mm | 2.89 | 3.05 | 3.07 |

### 3.5.3 Cell zone and boundary condition

The properties of the porous zone in the partially filled section were set using two different conditions: (1) cell zone conditions and (2) boundary conditions. In the cell zone condition, there are two available parts: 'Channel' and 'Porous.' Hence, the rectangular structure needs to be defined with an appropriate foam property. The setting can be done in the ‘setting of the cell zone’ where a porous zone is defined and selected at the porous part. A no-slip condition is applied to the channel wall to assume that there is no velocity at the wall boundaries that could affect the fluid velocity inside the channel. The porosity, viscous and inertial resistance coefficient was set as required, following the experimental data. Earlier, the viscous and inertial resistance coefficients were found using Equations (2.8) and (2.9) from Ergun law. Meanwhile, an isothermal condition was assumed along the channel since this research mainly focused on the flow behaviour and did not consider any changes of the temperature inside the channel or its effect. The k-ε turbulence model was used in the CFD simulation, considering the turbulent flow in the wind tunnel (Sauret, Abdi, and Hooman, 2014; Banjara and Nagarajan, 2020). The turbulent flow was also considered inside the porous region since the Reynolds number based on permeability is greater than 150. The same inlet velocities of 1.0, 3.0, and 5.0 m/s were used in the simulation at the boundary conditions. The simulation under ‘hydraulic diameter and turbulent viscosity’ was used in this CFD simulation for a turbulence flow which is the most appropriate to be used with the present data. The parameters and boundary conditions used in the analysis are tabulated in Table 3.8.

Table 3.8: Parameter and boundary conditions for channel and porous medium

| Parameter \ Foam Scale | 2 | 4 | 6 |
|---|---|---|---|
| Velocity, ($ms^{-1}$) | | 1.0, 3.0, 5.0 | |
| Porosity, ε (-) | 0.88 – 0.90 | 0.88 – 0.91 | 0.88 – 0.94 |
| Pore Diameter (mm) | 11.55 | 23.10 | 34.60 |
| Viscous resistance coefficient | 29251.65 – 45060.13 | 16033.32 – 31519.34 | 13554.30 – 27802.36 |
| Inertial resistance coefficient | 57.24 – 73.48 | 41.68 – 61.46 | 16.53 – 45.18 |



### 3.5.4 Solving and visualization

The simulation can only be conducted once all the material characteristics, zone and boundary conditions were defined correctly. A SIMPLE algorithm was chosen because the method uses the relationship between velocity and pressure to enforce mass conservation (Park, Seo, and Jeong, 2020; Diani et al., 2014). Meanwhile, hybrid initialization located under ‘solution initialization’ was used for solving Laplace’s equations to determine the velocity and pressure parameters. The results of CFD analysis were observed at the upstream, porous, free stream (above the porous medium) and the downstream regions as shown in Figure 3.15. The solution converged in 1000 iterations for utilizing precise data measurement and calculation. The CFD results are presented as streamlines where it can show the pathway of the fluid particles. The colours distinguish the fluid velocities in the partially filled channel. Therefore, a local velocity at each region of interest can also be used to generate a velocity profile and used to validate the experimental data. The simulation data was collected at the upstream and downstream regions, specifically, at 0.075 m away from the middle section as shown in Figure 3.15.

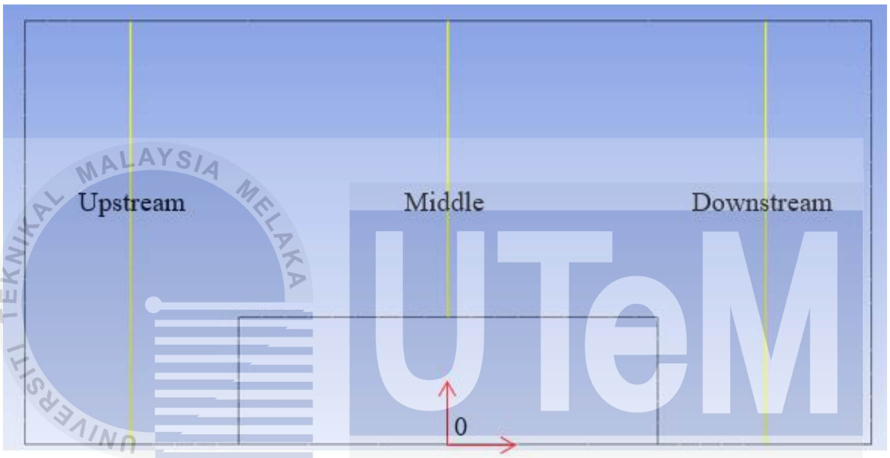


Figure 3.15: Area of observation in CFD result



### 3.5.5 Model validation

The results of the past studies (Sauret, Abdi, and Hooman, 2014) and (Narasimmanaidu et al., 2021) were used to verify the CFD model in the partially filled channel. Both studies (Sauret, Abdi, and Hooman, 2014; Narasimmanaidu et al., 2021) conducted 2D CFD analysis and validated the results by an experimental data that illustrated almost similar patterns. In this research, the foam was placed in the middle section of the channel, where the channel size is 0.1 m (H) × 0.2 m (L). However, a slightly smaller setup with size as of 0.5 m (H) x 2 m (L) was used in Sauret, Abdi, and Hooman (2014) while Narasimmanaidu et al. (2021) at 0.078 m (H) x 0.35 m (L). In this step, the fluid velocity in the CFD analysis was set at 6.2 m/s, used only for a validation process to similarize the fluid properties and a porous structure with 30 PPI properties has been defined in the middle. Figure 3.16 shows the model validation with the past studies in terms of velocity profile. The velocity profile at the upstream region and downstream region were evaluated, where the effects from the presence of open-cell foam are discussed. The region that most affected by the presence of open-cell foam is the downstream region where the foam restricts the fluid path to that region. The results show that the CFD analysis is slightly different compared to the past studies, where it may result from the different heights of the channel. The blockage ratio then will clearly see forms a different blockage ratio where the study from Narasimmanaidu et al. (2021) will resulting 0.39 of blockage ratio which is higher compared to this study, 0.2 blockage ratio. From the previous study, it is expected that the velocity at the same height of blockage ratio will produce a smaller velocity and increase to the freestream region. However, the fluid flow in the CFD study is an almost similar pattern to the past studies from Sauret, Abdi, and Hooman (2014) and Narasimmanaidu et al. (2021) where we can see the occurrence of higher velocity at the top part of the partially filled channel. The red box in Figure 3.16 highlighted the difference in velocity profiles at the downstream region between the present and existing study from Narasimmanaidu (2021) and Sauret (2014). The difference could be due to different channel lengths used in their studies where the lengths are longer between the rear edge of the foam to the downstream region. The turbulent flow could have fully developed along the channel length but the intensity of the turbulence may decrease with a shorter channel's length. The consistency of trend from this research as a comparison to Sauret, Abdi, and Hooman (2014) and Narasimmanaidu et al. (2021) is sufficient to imply the validation for the predicted and experimental studies.

Meanwhile, the velocity profiles from the experiment share almost the same velocity patterns and the value is slightly higher compared to the study by Shikh Anuar et al. (2018). The accuracy of the hot wire anemometer contributes to the difference in velocities measurement. The structure of the open-cell foam also needs to be considered since the actual phenomenon from the experimental study considered some of the foams as a solid block, e.g., the 30 PPI foam has a very small pore structure that reluctantly allows the fluid to flow inside its porous structure and the CFD simulation ignores the probability in the real cases. Shikh Anuar et al. (2018) also observed that the velocity at the upstream region is slightly higher than the inlet velocity, $U_{inlet}$ and the air velocity that was originally set up in the unloaded wind tunnel, $U_0$. At the downstream region, the velocity profile from the experimental studies also shares the same pattern with the CFD result where the velocity profile is larger compared to the previous study from Shikh Anuar et al. (2018). It is important to consider a few factors such as the channel length, blockage ratio and others since this research may have slightly different parameters compared to the previous study. In conclusion, the results from this research have good agreement with the previous study but the uses of different parameters may relate to slightly different findings.

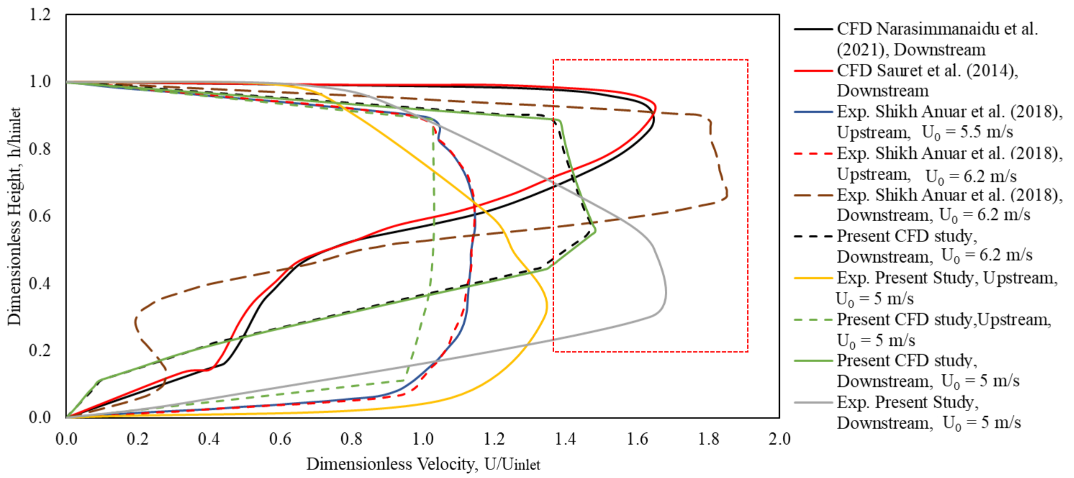


Figure 3.16: CFD model validation

## 3.6. Summary

In summary, the details of experimental and numerical works in this research have been explained, where the experimental works focused on the configuration the arrangement of the works including the specifics and descriptions of each instrument, rig, and sensor. All the sensors used need to be placed exactly at the right location so that the experimental setup and processes are in good working order for data collection. Meanwhile, the numerical works consider closely the setup of the experiments so that a comparison can be made between the results from experimental and numerical works at the later stage of this research.

# CHAPTER 4

# RESULTS AND DISCUSSIONS

## 4.1 Overview

This chapter presents the outcomes from both experimental and numerical studies on a partially filled channel with 3D printed open-cell foams. The 3D printed foams were produced using two different 3D printing technologies, and they were discussed in terms of surface roughness, microstructures and other properties that are relevant to porous materials. The behaviour across the partially filled channel is analyzed through velocity profiles and the effects of pressure drop are investigated further to develop a model of slip velocity at the interface of open-cell metal foam. The predicted model of slip velocity, obtained from the 3D printed foams is presented and its compatibility with the open-cell metal foam of smaller pore diameters is discussed in detail.



## 4.2 Microstructural and physical properties of 3D printed open-cell foam

### 4.2.1 Physical and microstructural properties

Figure 4.1 shows the 3D printed open-cell foams with different pore diameters produced using SLS and FDM. There is a limitation in producing the open-cell foams using SLS and FDM. Figure 4.1 (a) shows some damage to the porous structure, marked with red circles. which occurred when cleaning off the foams from the unfused nylon powder. Thus, the smallest foam, intended to mimic the pore diameter of a real 5 PPI metal foam, was found to be fragile when produced using SLS with nylon material. This failure is also expected to happen with other types of additive manufacturing that use thermoplastic materials.

Therefore, it is rather difficult to produce a 3D printed foam with a pore diameter of 5 PPI and ligament diameter of 1.13 mm, moreover, foams with smaller pore diameters such as 10 PPI to 40 PPI, are commonly used in industries. Figure 4.1 (b) – (d) shows the 3D printed foams with larger pore diameters; 2 scale, 4 scale, and 6 scale, produced using SLS. The thicker ligament makes the structure strong and can be cleaned easily using high-pressure air. Meanwhile, Figure 4.1 (e) shows the 6-scale foam produced using FDM. Regardless of the 3D printing technology and used material, the scale factor of 2 or above results in larger ligaments and improved foam's ligament strength compared to the 5 PPI foam. However, the 5 PPI or higher PPI is not used in the research since the pores were clogged by the residues from the AM machining e.g., FDM.

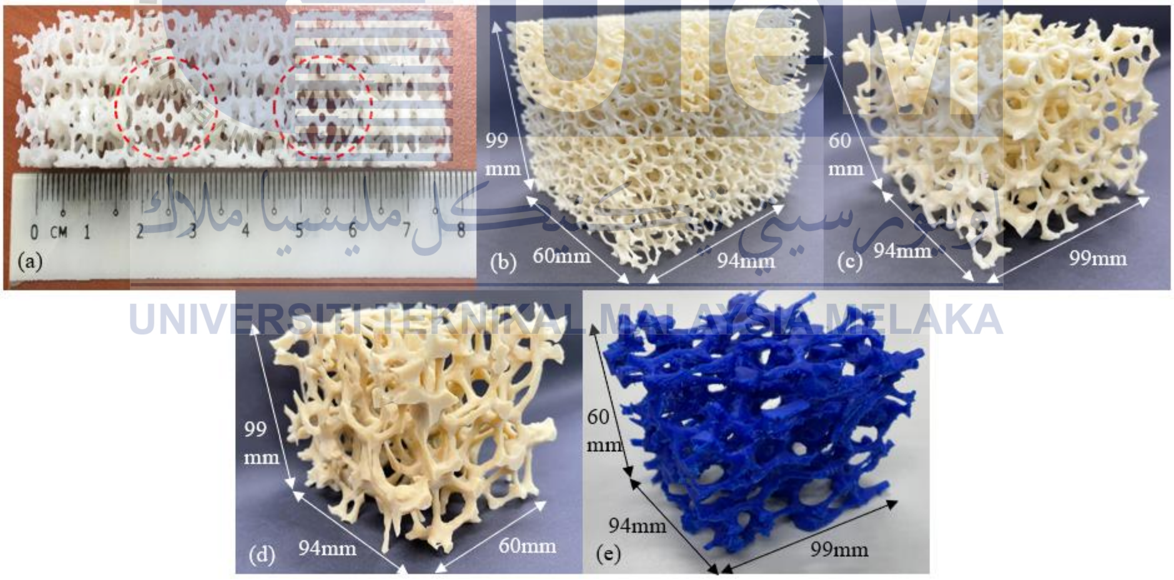


Figure 4.1: (a) SLS, 5 PPI, (b) SLS, 2 scale foam, (c) SLS, 4 scale foam, (d) SLS, 6 scale foam, and (e) FDM, 6 scale foam

Microscope images of 3D printed foams and metal foams can be seen in Figure 4.2, where different structure compositions and surface finishing (roughness) are shown on the ligament surfaces. Figure 4.2 (a) - (b) represent the structure of SLS foam while Figure 4.2 (c) - (d) and Figure 4.2 (e) - (f) represent the structure inside the FDM and conventional 10 and 30 PPI metal foam, respectively. The use of FDM has created more residues (thin strings within the porous structure) with significant layering effects, as shown in Figure 4.2 (c). The residues obstruct the fluid flow passages and potentially altered the fluid flow behaviour in the porous structure. The residues can be removed easily from large pore foams e.g., 2 scale foam and above. However, it will be difficult to reach the residues in smaller pore diameters, especially in the middle of a thicker foam. Melting and extruding raw materials at an angle greater than $45^\circ$ can cause residue buildup and require support for FDM foam structures. Thus, it is not recommended to use FDM to produce 3D printed foams with small pores. Unlike FDM, in SLS production, the unfused powder serves as the support and does not adhere to the foam structure. Hence, it is a lot easier to clean the foam produced with SLS as compared to FDM's. Figure 4.2 (b) depicts the cross-section of an SLS-printed foam with visible powder marks on the connecting struts. Meanwhile, FDM yields an unsatisfactory surface finish compared to SLS, a result of melting the material during the printing process. Melting and extruding raw materials at an angle greater than $45^\circ$ can cause residue build-up. Support structures should not be removed during the slicing process and must be applied strategically to maintain the structure's shape and produce high-quality foam. Further investigation into surface roughness is necessary because there are variations in the finished surfaces produced by these two 3D printing technologies. It is important to note that surface roughness plays a significant role in various conditions such as pumping power or the amount of contact surface area in a partially filled configuration.

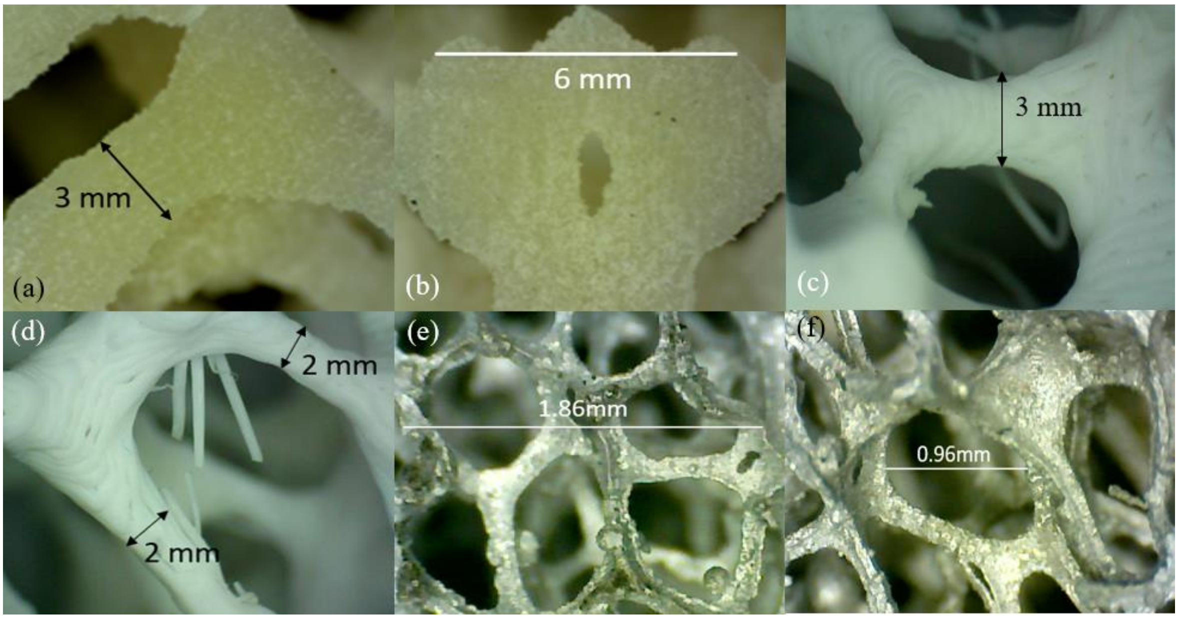


Figure 4.2: (a) SLS foam ligament (b) Cut-section of the SLS foam, (c) FDM ligament (d) Residues within FDM foam structure (e) Microstructure of 30 PPI open-cell metal foam and (f) Microstructure of 10 PPI

### 4.2.2 Morphologies and surface roughness

Figure 4.3 show ligament surfaces of 4-scale foam, which is preferred in order to have a sufficiently flat surface area to ease image processing. Figure 4.3 (a) shows a raw surface image of SLS's foam ligament, while Figure 4.3 (b) shows the same image with a subtracted background, in which the accumulated leftover powder on its surface can be clearly seen. Figure 4.3 (c) and (d) show the layering effect of FDM and its subtraction background image, respectively.

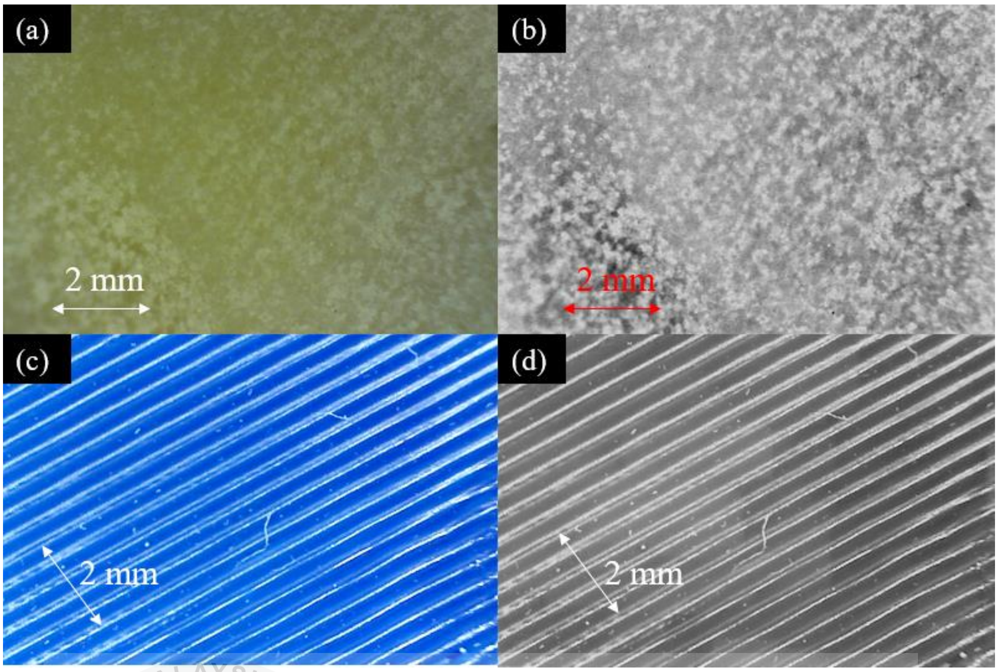


Figure 4.3: Image processing using Image J: (a) Raw images of SLS's foam, (b) SLS's subtracted background image, (c) Raw images of FDM's foam, and (b) FDM's subtracted background image



Figure 4.4 shows surface plots for 3D printed foams produced using the SLS from three different faces; the top, and two sides of the foam. The surface plot is obtained from three different surfaces which are exposed to the free stream region while the other sides are being attached to the wall of wind tunnel. The mean calculated surface roughness is 4.553, 5.353, and 4.880 µm for the top, side 1, and side 2, respectively. It shows there is no specific difference between sides 1 and 2 but the smoothest surface will be used to face the incoming flow direction to reduce the frictional effects. There is a small difference in surface roughness, regardless of the face sides, which is 8.84 %. A previous study from Omar et al., (2022) also conducted a surface roughness test for the SLS sample (in the range of 12-23 µm), but this present research has a better surface roughness since it uses a high composition of virgin nylon powder that aid bonding and reduced spacing between the particles. There is also an outlier, which can be seen in Figure 4.4 (b), which appeared as a ‘red’ peak. There is a possibility that the outlier is caused by imperfect finishing quality in that specific region or the accumulation of powders at a single spot. The surface roughness is an important factor to be understood since a higher surface roughness will intently increase resistances in the streamwise direction of open-cell foam and create a more tortuous path for the fluid flow. This occurrence contributes to an increase in pressure drop as the fluid must navigate through the intricate structure of the open-cell foam. Meanwhile, the relationship between the pressure drops and fluid flow is described by Darcy’s law.

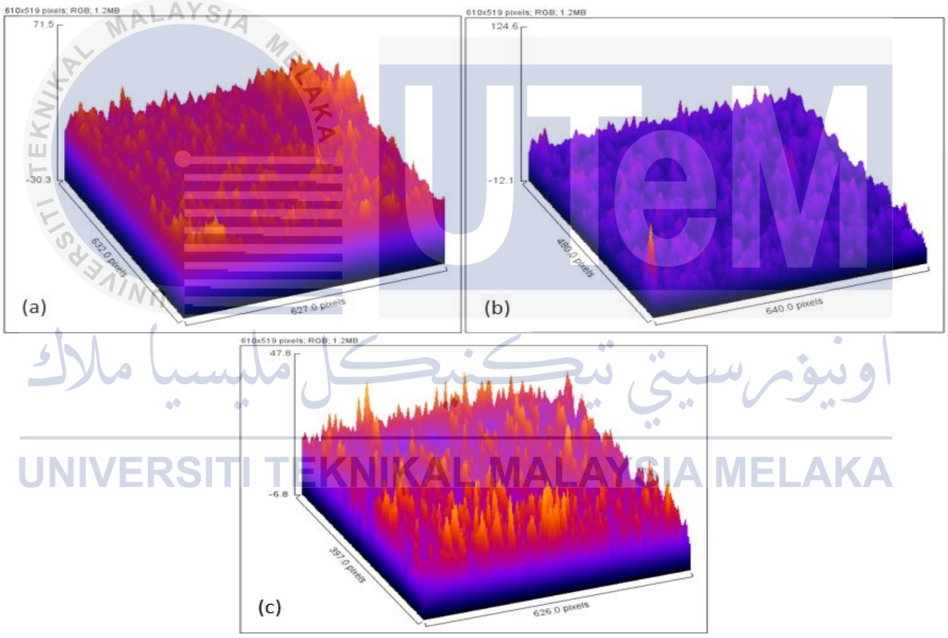



Figure 4.4: Surface plot for SLS foam: (a) Top, (b) Side 1, and (c) Side 2

By comparing Figure 4.4 with Figure 4.5, it becomes apparent that the ligament surface of 3D printed foams generated using FDM is rougher than SLS. The mean surface roughness values calculated for FDM are approximately 26.270 Ra for the top surface, 32.133 Ra for side 1, and 28.395 µm for side 2. The maximum difference between these values is approximately 18.25%, which is observed between the top surface and side 1. The top surface has lower layering effects (thickness) as compared to the other surfaces. The factor that causes differences in this layering thickness is still undescribed which is mainly not covered in this study. Figure 4.5 (b) shows Side 1 has a slightly different pattern as compared to the other surfaces where the surface plot for side 1 has stable in increasing the roughness. Side 1 tends to be the cut-section face as an example that has been shown in Figure 4.2 (b), where the surface is formed during the earlier process in drawing and reconstructing the CAD drawing where it is the part that has been removed to apply the required dimension. Thus, the surface may be formed with the most stable groovy surface and cause more arranged surface roughness peaks compared to the rests. It was found that the machining parameters such as nozzle speed and extruding temperature could be insignificant factors as they do not influence the variety of Ra reading on part surface (Kazim et al., 2022). Thus, those parameters or any other parameters were not considered in this research. This research focuses on two types of 3D printing technologies to find a better solution for producing the open-cell foam with smoother surface.



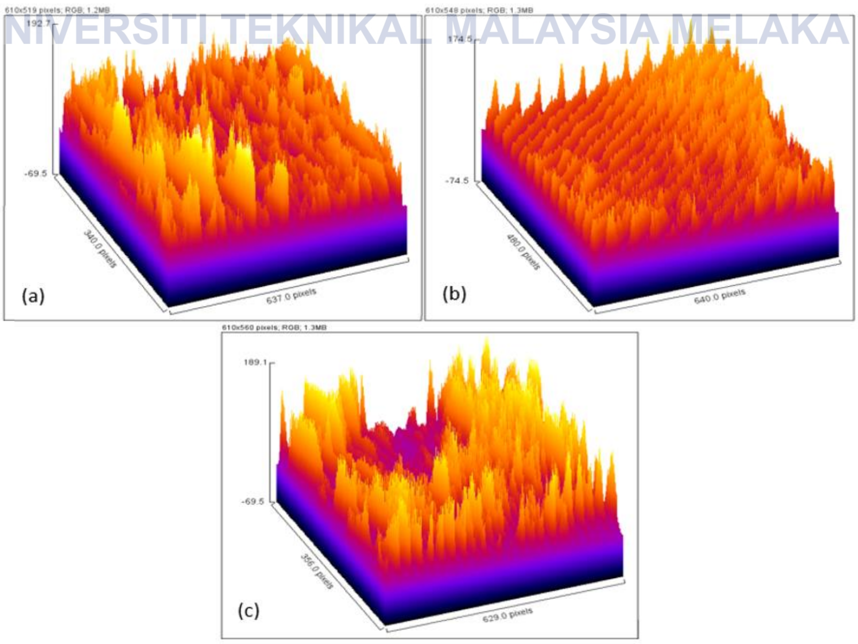


Figure 4.5: Surface plot for FDM foam: (a) Top, (b) Side 1, and (c) Side 2

The comparison of gray values between SLS dan FDM foams is shown in Figure 4.6, where the values fluctuate within a specific range, from 5 to 20 for SLS and higher for FDM in a range between 20 to 95. For open-cell foams produced using SLS, those three sides (Top, Side 1, and Side 2) have fluctuated gray values, where the top side shows a maximum value of 20. Meanwhile, the top side from the FDM foam as shown in Figure 4.6 (b) shows several peaks, reaching up to 94 gray values. The highest gray value from the SLS surface as shown in Figure 4.6 (a) could be due to randomly scattered powder that has been attached to the ligament surfaces. Since the gray values for the FDM foam have significant fluctuation trends and are higher than SLS's, it proves that the FDM causes a greater surface roughness, even though both foams were produced from the same STL file. This could be due to the layering effects (the nature of the FDM printing process) has formed on the ligament surfaces. This distinctive feature could be seen as the PLA was melted and extruded to build the foam layer-by-layer. As the PLA has low layer adhesion, a rough surface finish should be expected. In this study, these layers are significantly visible, creating a series of horizontal lines on the foam surfaces. To minimize this effect, the temperature must be carefully controlled, and the printing speed should not be too high. The trial-and-error method is the best way to produce a smoother foam surface. In this research, the SLS technology is a better choice as compared to FDM.

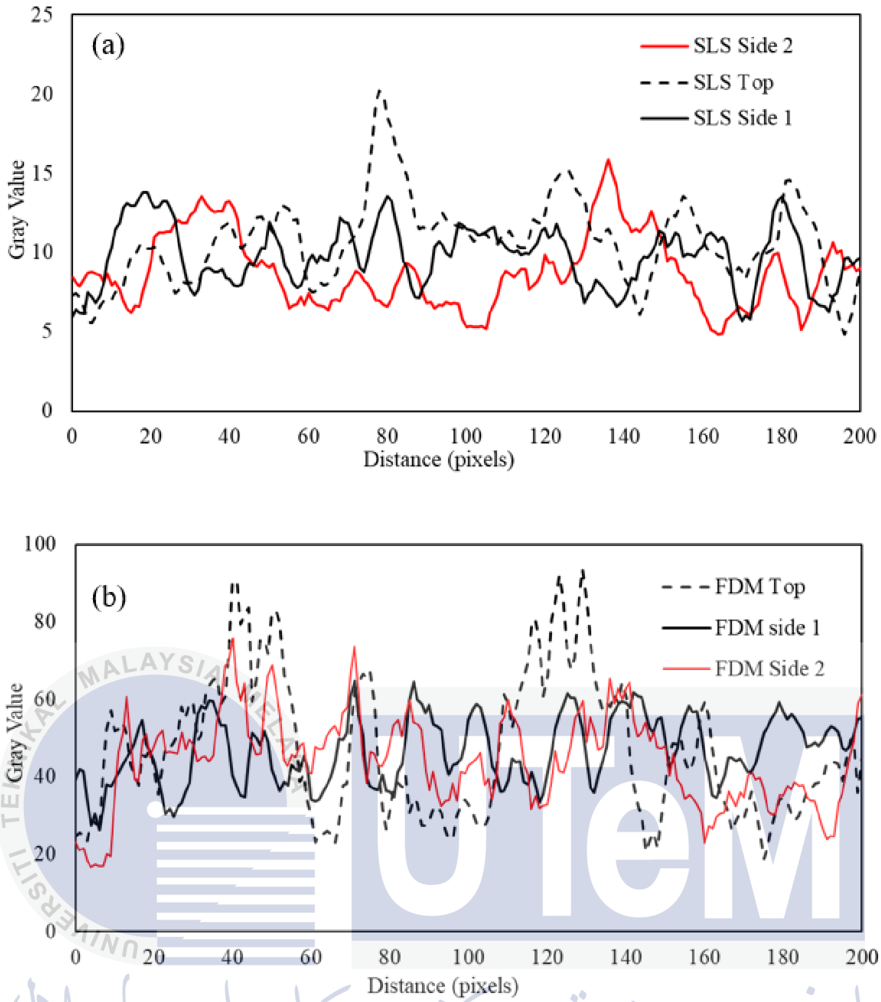


Figure 4.6: Comparison between faces (frontal area): (a) SLS foam and (b) FDM foam



The comparison of the averaged gray value plots for surface areas for SLS and FDM foam is shown in Figure 4.7. The qualitative data, from Figure 4.7 shows a lower averaged gray value that does not exceed 20 gray values which are considered smoother surfaces of 3D printed foams printed using SLS compared to FDM. When exposed to fluid applications, it is expected that the significant difference in the surface roughness of open-cell foam from these two 3D printing methods will result in a notable difference in pressure drop values, especially at higher flow rates.

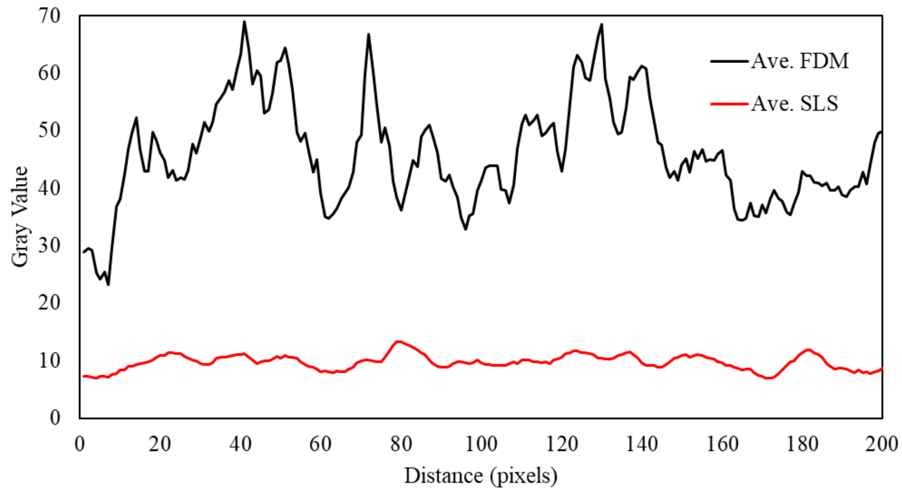


Figure 4.7: Comparison of surface roughness between SLS and FDM foams

### 4.2.3 Permeability of various foams

Permeability is defined as the volume of fluid that passes through the porous structure, where the structure of interconnected ligaments and pores plays an important factor in affecting its value. The lesser number of ligaments and a larger pore diameter will lower the restriction for the fluid moving across the porous structure. The permeability and inertial coefficient of 3D printed foam were determined using the Forchheimer equation, which can be solved by using experimental data and quadratic polynomial expression in a fully filled configuration. A plot of pressure drops per unit length, $\Delta P/\Delta l$ against inlet velocity is needed, and the quadratic polynomial expression was extracted from the trendline as shown in Figure 4.8 (a) - (c). Table 4.1 shows the tabulated result of permeability, inertial coefficient, and coefficients for the fully filled configuration with a blockage ratio, $h_f/h_c$ of 1 which represents a fully filled configuration.

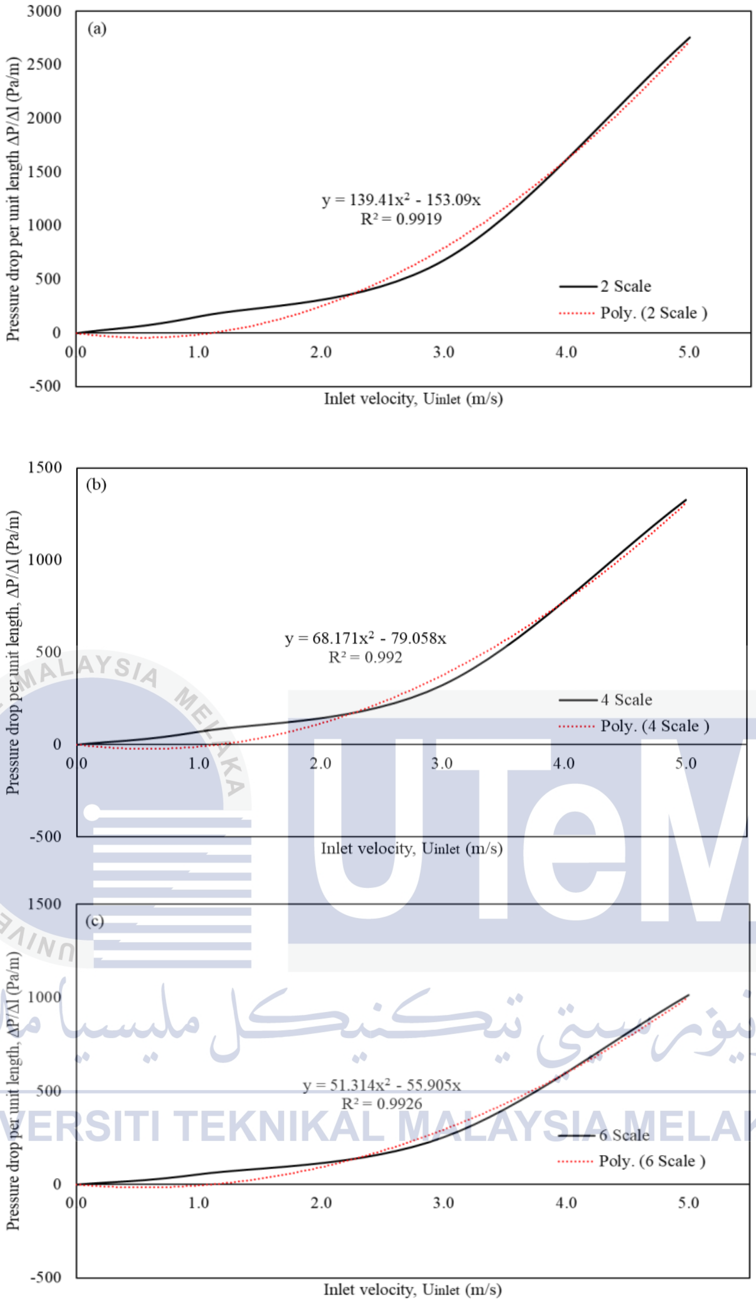


Figure 4.8**:** Determination of Forchheimer's coefficient for different scaling factors; (a) 2 scale, (b) 4 scale and (c) 6 scale

Table 4.1: Permeability and inertial coefficient for fully developed configuration.

| Pore size (Scale) | a | b | Permeability, K x$10^{-9}$ ($m^2$) | Inertial coefficient, $f$ |
|---|---|---|---|---|
| 2 scale | 153.09 | 139.41 | 1.24 | 0.0429 |
| 4 scale | 79.058 | 68.177 | 2.40 | 0.0292 |
| 6 scale | 55.905 | 51.314 | 3.39 | 0.0261 |

Meanwhile, the permeability for the partially filled configuration with different foam heights (30, 60 and 90 mm) was obtained through the product of permeability of the fully developed configuration with the blockage ratios. Table 4.2 shows the properties of 3D printed open-cell foams of 2, 4, and 6 scale factors.



Table 4.2: Physical properties of 3D printed open-cell foam

| Physical properties | 3D printed open-cell foam | | |
|---|---|---|---|
| Scale | 2 | 4 | 6 |
| Ligament diameter, $d_l$ (mm) | 2.28 | 4.54 | 6.80 |
| Pore diameter, $d_p$ (mm) | 11.55 | 23.10 | 34.60 |
| Porosity, ε (–) | 0.88 – 0.90 | 0.88 – 0.91 | 0.88 – 0.94 |
| Permeability, K ×$10^{-9}$ ($m^2$) | 0.37 – 1.24 | 0.72 – 2.40 | 1.02 – 3.39 |
| Foam height, $h_f$ (mm) | 30, 60, 90, 100 | | |
| Blockage ratio, $h_f/h_c$ | 0.30, 0.60, 0.90, 1.00 | | |
| Foam length, $L_f$ (mm) | 94 | | |

Figure 4.9 illustrated the relationship between the permeability of the foams with foam height. It is shown that the permeability for each scale factor shares the same trend, which is increasing with the foam height. The 6-scale foam also allows larger fluid passage, as the pore diameter is bigger. Thus, more fluids can easily pass through the porous structure

at a larger foam scale. A thicker foam with a foam height, $h_f$ = 100 mm shows higher permeability when compared to a smaller blockage ratio, e.g., 0.3, 0.6 or 0.9 with a foam height is less than 100 mm. The highest permeability at the foam height, $h_f$ = 100 mm for 2, 4 and 6 scales were recorded at $1.24 \times 10^{-9}$ m$^2$, $2.40 \times 10^{-9}$ m$^2$ and $3.39 \times 10^{-9}$ m$^2$, respectively. The lowest permeability can be seen from the 2 scale foam at height of 30 mm, which is 0.37 $\times 10^{-9}$ m$^2$.

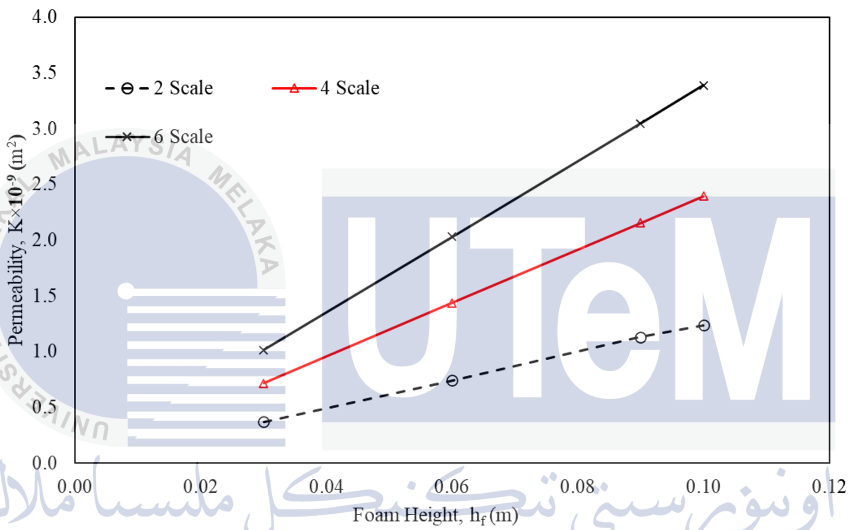


Figure 4.9: Plot of permeability against foam height

The inertial coefficient, $f$ is a dimensionless parameter that refers to the inertial effects in fluid flow through the foams. It has a significant relationship with pore diameter and foam height as shown in Figure 4.10. The inertial coefficient is inversely proportional to a dimensionless characteristic length of foam, which is a ratio of pore diameter and foam height, $d_p/h_f$. The lowest inertial coefficient is $7.83 \times 10^{-3}$ recorded at the highest ratio of pore diameter and foam height of 0.51. Meanwhile, the highest velocity recorded at $42.85 \times 10^{-3}$ which is at a ratio of pore diameter and foam height, 0.08. The inertial coefficient for foam with a 2 scale is higher when compared to other foam scales, 4 and 6.

Thus, the same height foam with smaller pores would contribute to more inertial effects as compared to the larger pores. Comparing the inertial coefficient in the same group of foam scales but different foam heights shows that the difference may be giving about 70 % where it has occurred at 2 scale foam. However, when comparing the same foam height but different foam scales show a lower difference, which is 39.09 %. The foam height is seen to be more affiliated with the flow characteristics in this research, but the pore diameter also plays an important factor.

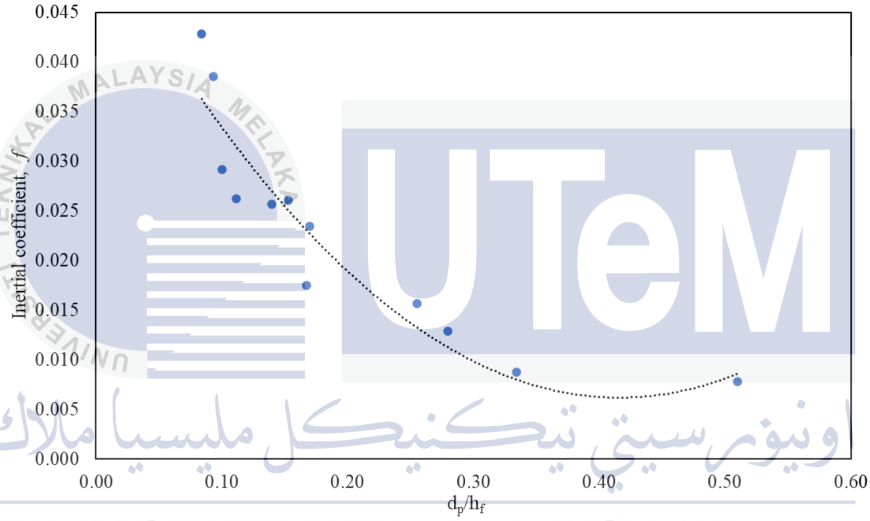




Figure 4.10. Plot of inertial coefficient against a ratio of pore diameter and foam height

## 4.3 Flow characteristics in partially filled channel with open-cell foam

The fluid flow behaviour in the partially channel is discussed in terms of velocity profiles for all the affected regions (upstream region, partially filled section and downstream region). The velocity profiles are presented as dimensionless velocity, $U/U_{inlet}$ (a ratio of local velocity with inlet velocity) on the y-axis, while dimensionless height, $h/h_c$ (a ratio of measurement point with channel height) on the x-axis. The pressure drops are also discussed as a crucial key parameter that would be affected by the foam porous structure. The pressure drop data is presented as pressure drop per unit length ($\Delta P/\Delta l$) at the y-axis and inlet velocity, $U_{inlet}$ for the x-axis.

### 4.3.1 Velocity profiles

The presence of a porous structure block has affected the velocity profiles in the channel. Figure 4.11 shows the velocity profiles at the upstream region with foam sizes of 2, 4 and 6 scales with different blockage ratios (0.3, 0.6, and 0.9). In the upstream region, the velocities show larger values near the bottom side of the channel, $h/h_c = 0$ which is the same with the unloaded wind tunnel cases as shown in Figure 3.11, regardless of the pore diameters and foam heights. A similar result for the upstream region was also found by Sauret, Hooman, and Saha (2014), where there is no significant changes in the fluid flow at quarter length of the channel. By introducing various inlet velocities, there are insignificant changes in the velocity profiles due to the capability of the porous foam to transmit the fluid inside the structure that is affected by pore diameter where the velocity is in the nearest range. This happened because of the larger pore diameter used in this research, at least twice 5 PPI, which allowed the fluid to flow into the porous structure with lesser restrictions, resulting in undisturbed flows at the upstream region. A study by Lu, Zhang, and Yang (2016) also stated that the resistance from porous structures is affected by pore density and influencing the amount of fluid that can pass through the porous region. The lower blockage ratio also shows a larger velocity in the upstream region as compared to the higher blockage ratio, e.g., 0.6 and 0.9. However, the fluctuated velocity in the partially section occurs possibly because of the randomness interconnected pores at the interface region. However, the fluctuated velocities could be due to the sensitivity of hot-wire anemometer. Thus, the averaged velocities along the y-axis were used to compute the slip velocity model.

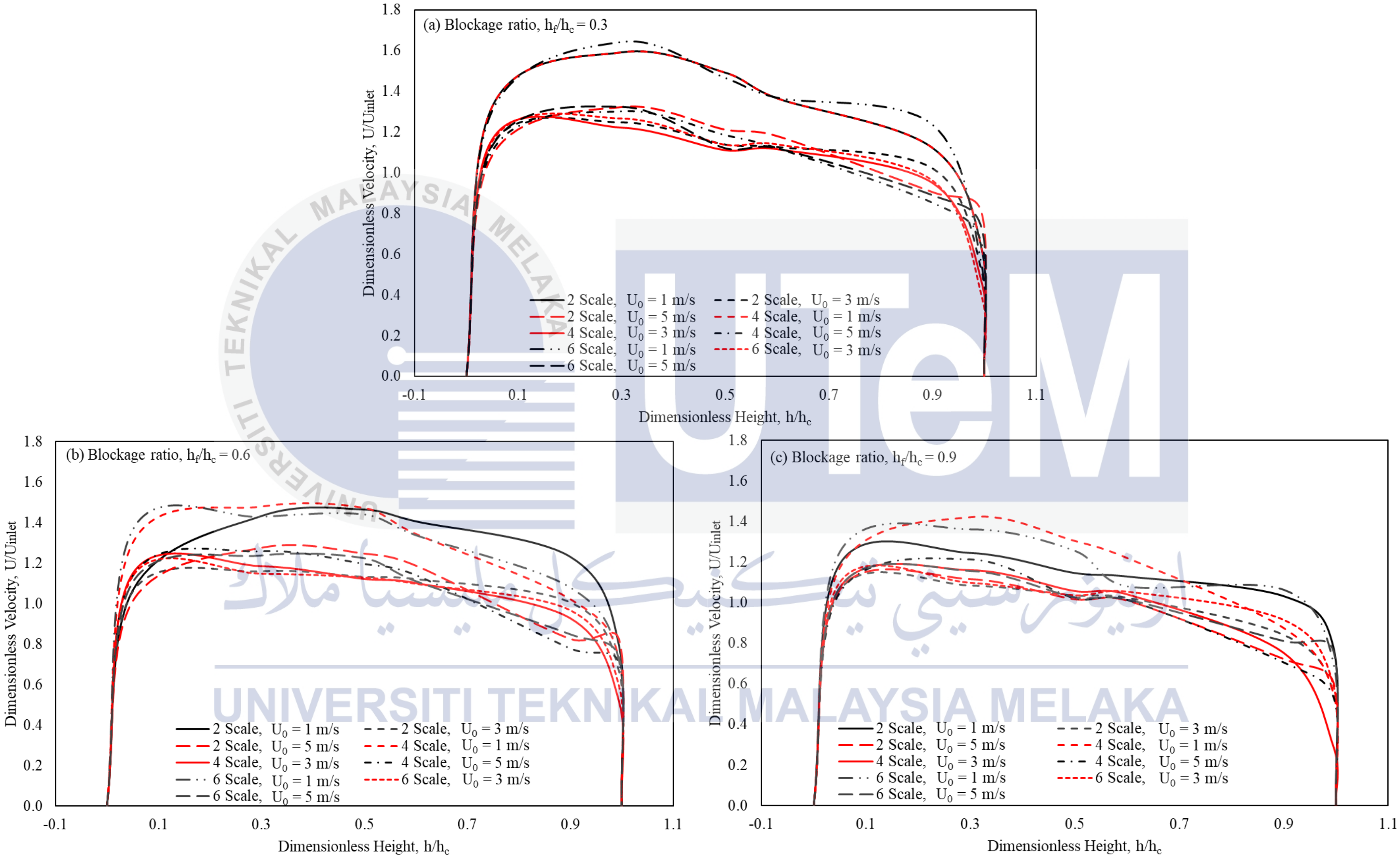


Figure 4.11: Velocity profiles in the upstream region with different blockage ratios: (a) 0.3, (b) 0.6, and (c) 0.9

Figure 4.12 shows the velocity profiles at the downstream region for various blockage ratios and pore sizes. The foam with a blockage ratio of 0.3 shows an asymmetric pattern at the downstream region, unlike the turbulent velocity profile in the unloaded channel. The same blockage ratio also induces the highest flow velocity at the middle height of the channel. The flow velocities in a region, from the bottom to the center of the channel (h/hc = 0 to 0.5) asymmetrical to the top part, from the center to the top wall of the channel (h/hc = 0.5 to 1.0). The flow patterns are different compared to the unloaded wind tunnel since there is a reduction of velocities near the bottom part of the channel. This difference shows the influences of foam existence on the fluid flow in the downstream region. Based on Figure 4.12 (a) to (c), it is also can be concluded that the flows encounter a high restriction that possibly affected the area behind the porous foam. The flow velocity also gradually increases until reaching the highest value in the free stream, right after the middle of channel height and then decreasing towards the top wall. However, there remains fluctuation of velocities at the bottom part, which has a higher velocity compared to the region before the blockage ratio at 0.3 but decreases to a certain value before the velocity reaches the highest peaks. The result only occurs in some cases with a blockage ratio of 0.6 and 0.9, which may be attributed to the high turbulence flow and fluctuated velocities because of the randomness of interconnected pores at the interface region. The results from 3D printed foams with a blockage ratio of 0.3 also show that the fluid tends to be turbulent in the downstream region but the occurrence is affected by the distance between the downstream region and the foam's rear end which should slightly decrease when the flow rate increases (Luu, Philippe, and Chambon, 2015). However, this is not happening for the foams with a higher blockage ratio since the fluid requires more distance of downstream region to form a uniform flow.

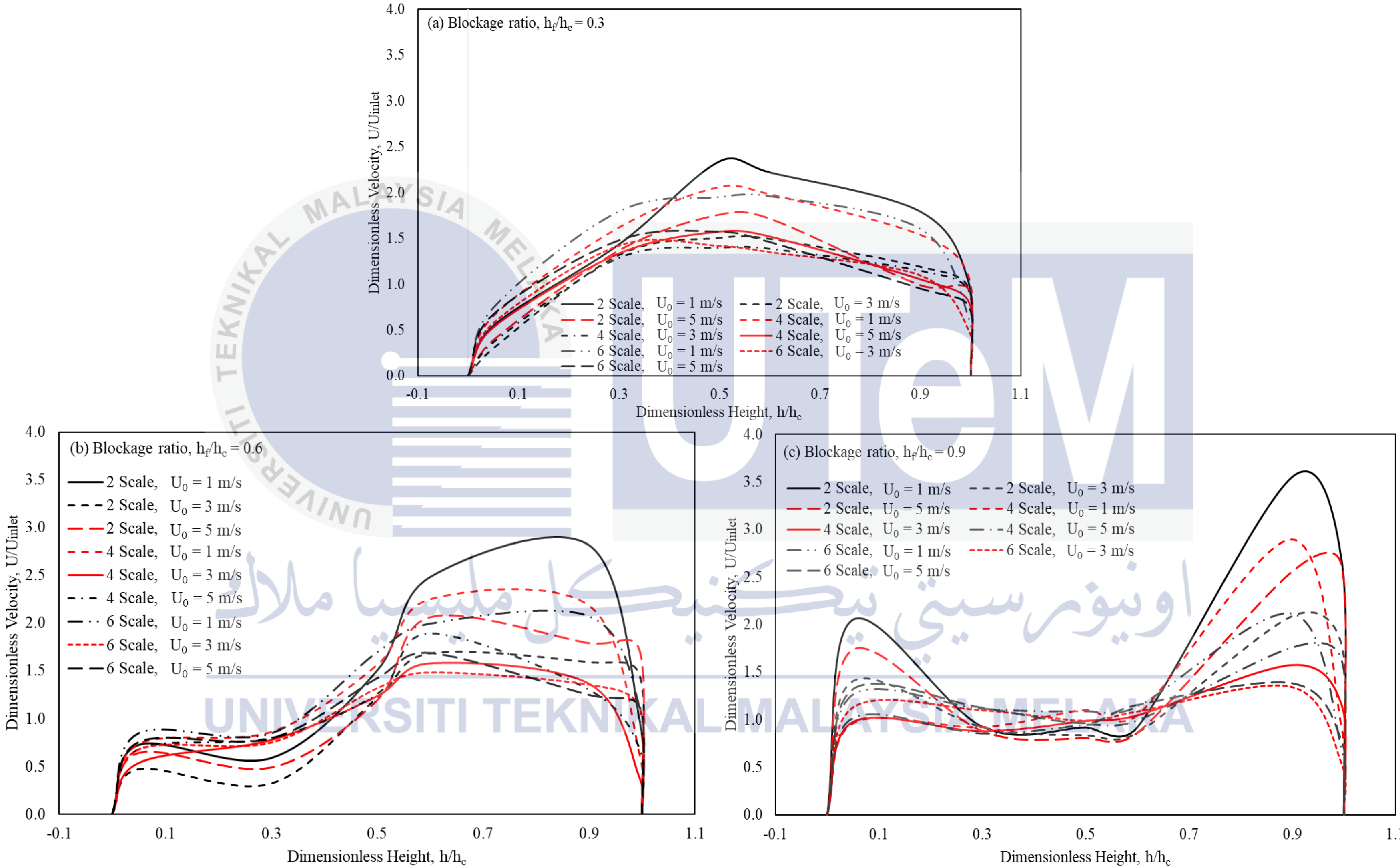


Figure 4.12: Velocity profiles in downstream region with different blockage ratios: (a) 0.3, (b) 0.6, and (c) 0.9

The fluid flow behaviour at the middle section of porous foam is shown in Figure 4.13. The velocity profiles represent data from 2 to 6 scale foams with different blockage ratios in the free stream region. Since the velocity profiles are used to illustrate the flow behaviours in the middle section, the velocity inside the porous region is uncovered to give a better presentation presence of porous foam in Figure 4.13 (a) – (c). It is important to mention that this research does not measure the pore velocity as it only focused on the slip velocity at the interface region. The closest measurement point near the foam interface is 0.5 mm, due to the location of the built-in sensor inside the hot-wire anemometer. At blockage ratio, $h_f/h_c$ = 0.3, the 2 scale foam would have a lower velocity near the interface region compared to 4 and 6 scale foams, regardless of the inlet velocities. But this situation has changed in the free stream region, where the velocity for the 2 scale also recorded a higher velocity compared to the foams with the 4 and 6 scales. However, the fluid flow behaviour in the free stream region remains the same for each blockage ratio, where the 2 scale foam has a higher velocity compared to the other scale foams at 4 and 6 scales. At the blockage ratio, $h_f/h_c$ = 0.9, it also shows the 2 scale foam also has the highest dimensionless velocity, $U/U_{inlet}$ = 3.15 compared to the other blockage ratios, 0.3 and 0.6. The law of conservation of momentum states that a force is equal to the rate of change of momentum. By understanding the law of conservation of momentum, ones can see that the velocity is related to the cross-sectional area of the flow passage, where the point of interest is the free stream region and pore diameter at the interface region. Thus, the velocity increases as the flow passages through those two regions are decreased. A study by Lu, Zhang, and Yang (2016) also stated that an increment of foam height may lead to a higher velocity in the free stream region since the foam restricts the fluid flow in the porous structure, and at the same time forcing more fluids in the free stream region.

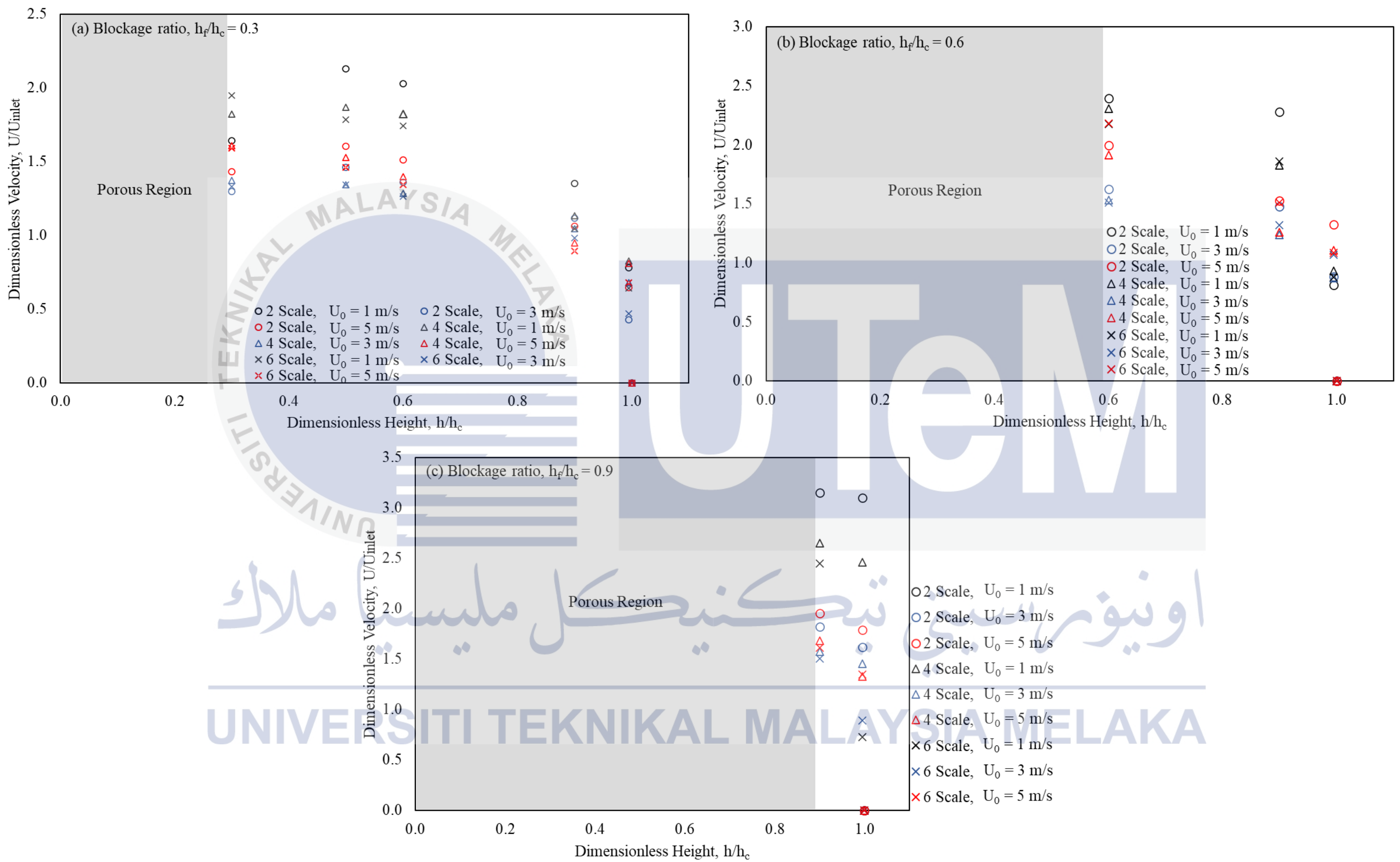


Figure 4.13. Velocity profiles at middle region with different blockage ratios: (a) 0.3, (b) 0.6, and (c) 0.9

The comparison between a solid resistance (acrylic block) and the porous foam is a must especially in determining whether there is a significant effect on the fluid flow due to the porous structures in the partially filled channel. This comparison is also to determine the fluid particle pathways, either entering or avoiding the porous structure and flowing into the free stream region. The effects of resistances between 3D printed foam and acrylic blocks of the same size in investigating the flow characteristics are illustrated in Figure 4.14 at different blockage ratios; 0.3 and 0.6. The comparison is made at only two different blockage ratios as the wind tunnel cannot support a fluid flow at 0.9 of blockage ratio using acrylic blocks. When a very thin flow passage in the partially section suddenly becomes larger at the downstream region, the pressure of the fluid will decrease. This is due to the principle of the conservation of energy, which states that the total energy of a closed system must remain constant. Thus, the fluid velocity in the downstream region decreases to maintain a constant mass flow rate, which results in a decrease in the kinetic energy of the fluid. According to Bernoulli's principle, this decrease in kinetic energy is accompanied by an increase in pressure energy and causes a decrease in fluid pressure in the downstream region and flexible duct. Consequently, the atmospheric pressure acts on the walls of the flexible duct, forcing it to be contracted with smaller flow passages inside. Thus, the comparison to the solid acrylic block is possible only up to 0.6. Most of the velocity profiles for both 3D printed foam and acrylic blocks have the same patterns except the flow velocity in the free stream region for a blockage ratio of 0.6. In this case, the flow is avoiding the obstacle and changes its direction into the free stream region. Thus, higher velocity is observed near the top wall. The same blockage ratio of the acrylic block also creates a recirculation zone in the downstream region as shown in Figure 4.14 (d). At a low inlet velocity of 1.0 m/s, the acrylic block also shows a higher velocity than the 3D printed foam at the high blockage ratio either in the upstream or downstream regions. This is because the acrylic block creates a sharper obstacle for the fluid to flow across the partially section, which results in a higher velocity region in the free stream region. As the fluid flows towards the acrylic block, it encounters a sudden increase in resistance to its flow. This causes the fluid to accelerate as it flows over the block. The fluid then decelerates as it passes through the wake region behind the block. This acceleration-deceleration process results in a higher velocity region in the free stream on the top of the block. In contrast, the use of the porous structure or 3D printed foam has a less defined obstacle but still provides restriction to the fluid flow. This leads to a more gradual change in the flow velocity as it passes through the porous structure, but a less pronounced increase in velocity in the free stream region.

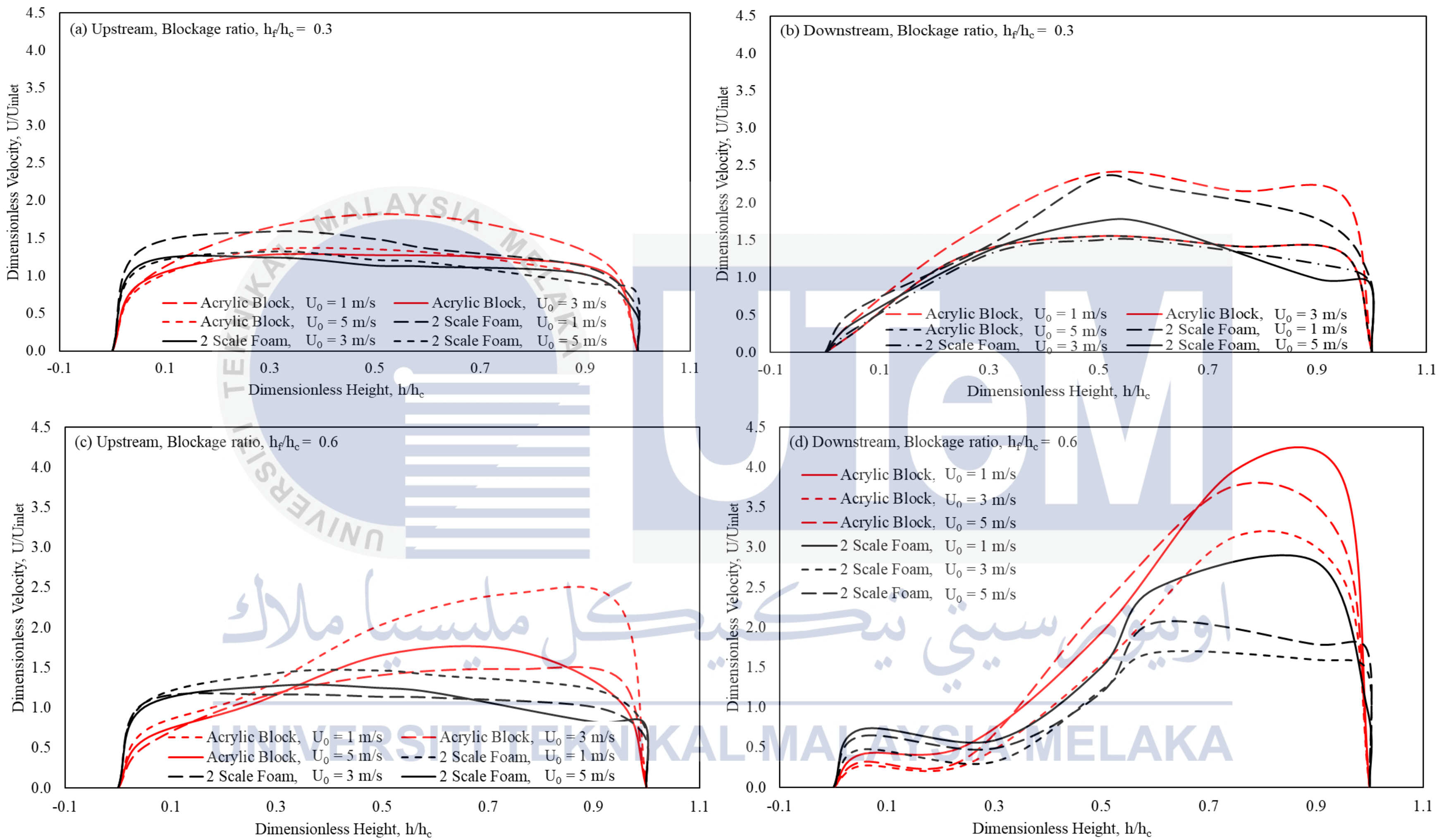


Figure 4.14: Comparison of velocity profiles between 3D printed foams and acrylic blocks with different blockage ratios: (a)-(b) 0.3 and (c)-(d) 0.6

The velocity of fluid flow through a real OCMF has been studied as a benchmark for analyzing the effects caused by the open-cell foam in the channel and the results are shown in Figure 4.15. The 10 and 30 PPI metal foams have pore diameters of 2.56 mm and 0.87 mm, respectively, which is about “4.5 times” smaller compared to the smallest 3D printed foam (11.56 mm). At the upstream region, it also shows a similar trend to the unloaded and 3D printed foam cases where it recorded an asymmetrical trendline that the velocity at the $h/h_c < 0.35$ is higher compared to $h/h_c > 0.35$. This happens as the fluid near the bottom wall started to accelerate to avoid the foam block. Meanwhile, the velocity profile at the downstream region for the open-cell metal foam shows a trendline that increases with a steeper gradient until reaching $h/h_c = 0.3$, which matches the pattern observed in the 3D printed foam. The 30 PPI foam has the highest velocity than the 10 PPI foam, regardless of the measurement locations. However, each velocities profile for inlet velocity, 3 and 5 m/s have the same and also almost close to the velocity despite having different pore diameters when comparing both 10 and 30 PPI which are at the middle region. The present research found a similar result with Shikh Anuar et al., (2018), where a larger PPI causes a lower velocity since the flow resistance is also more pronounced at higher blockage ratio foam. Similar to the previous literature by Sauret, Abdi, and Hooman (2014), this research also found the velocities of the fluid are increasing when approaching the foam surface. By increasing the foam’s pore density, the fluid tends to flow in the free stream region with a lower pressure drop (Jadhav et al., 2022).

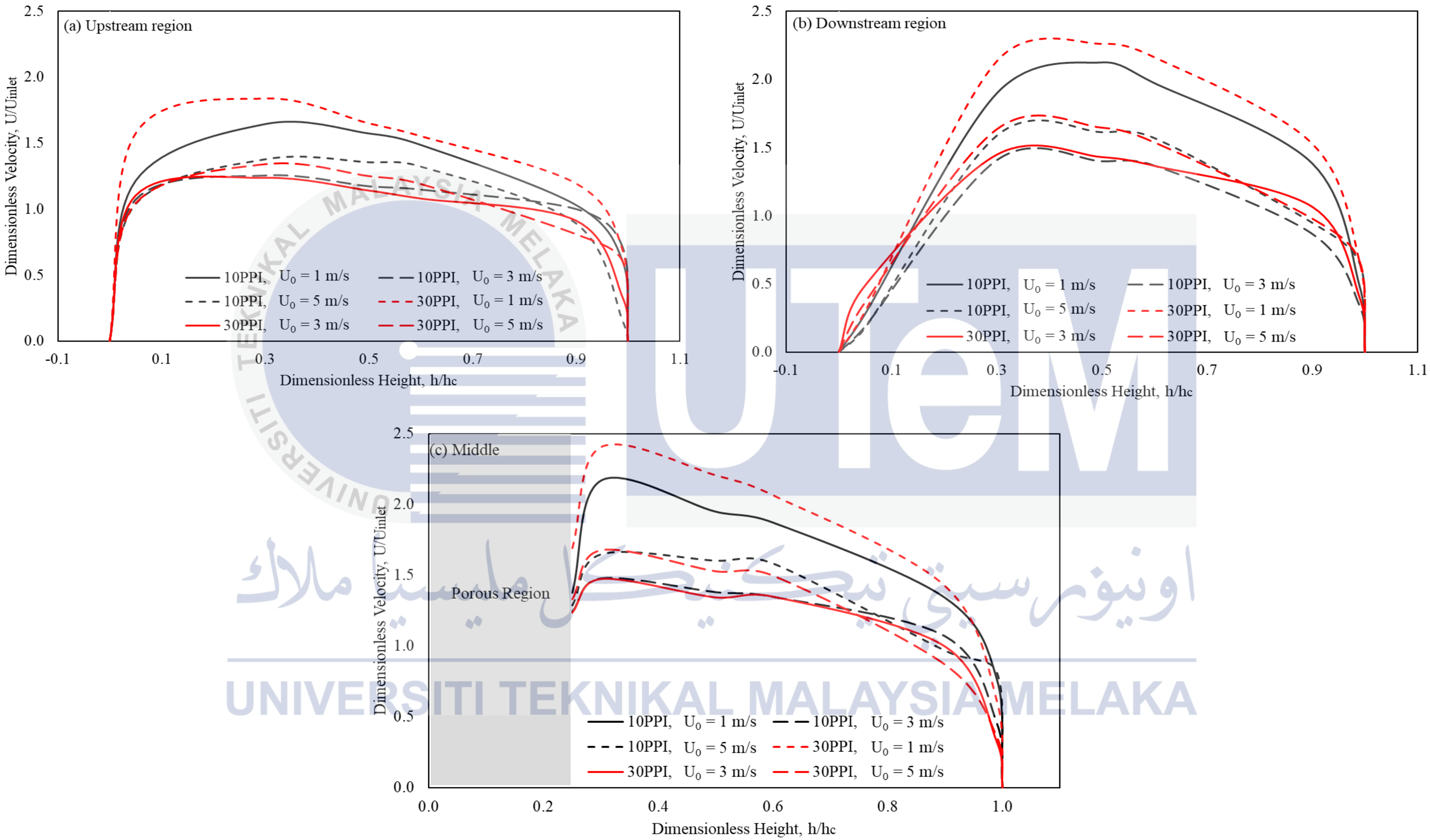


Figure 4.15. Velocity profiles across the open-cell metal foam at three different regions: (a) Upstream, (b) Downstream, and (c) Middle

### 4.3.2 Pressure drops effects

The effects of porous structure on the pressure drops are also investigated with the results shown in Figure 4.16. In this approach, the pressure drop of solid blocks is compared to 2 scale 3D printed foams. The effects of various blockage ratios are discussed. However, at a blockage ratio of 0.6, it shows that the acrylic block has a greater pressure drop than 3D printed foam, where it could reach 2000 Pa/m at $U_{inlet}$ = 5 m/s. The acrylic block does not allow the fluid to pass through, and higher restrictions to fluid flow. In the partially filled channel, the fluid tends to find small openings to flow through. With the 3D printed foam, its porous structure allows the fluid to move easier with less restrictions, which results in a lower pressure drop as compared to the acrylic block. Additionally, the surface area of the foam is much greater than that of the acrylic block with the same dimensions, which allows for more fluid to come into contact with the foam's internal structure, which can help to distribute the flow and reduce the pressure drop. However, for the higher blockage ratio, the results are quite similar for both 3D printed foam and also acrylic blocks. It is noteworthy to mention that the frictional effects in the porous structure of foam can also contribute to the pressure drop in the partially filled channel. As the fluid flows through the porous structure, frictional resistance would increase due to the interactions between the fluid molecules and the foam material, the nylon and also the layering effects. However, these frictional effects become significant only at a high blockage ratio of 0.9, in which, the induced pressure drop is similar to the acrylic block at a lower blockage ratio of 0.6. This result is only applicable to nylon material since the pressure drop may vary depending on the surface roughness of different materials, e.g., a more hydrophilic surface can also reduce frictional resistance and the associated pressure drop.

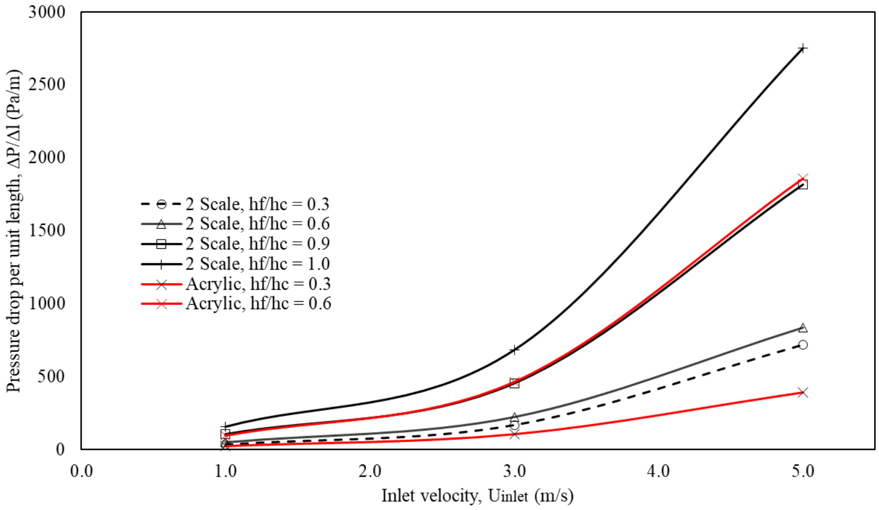


Figure 4.16: Comparison of pressure drops between 3D printed foam and acrylic block

The effects of various blockage ratios and pore diameters on pressure drops of the 3D printed foam are presented in Figure 4.17. The pressure drops for each foam show a similar trend inside the partially filled channel, where the pressure drops are increasing with the inlet velocity, regardless of the scale factors and blockage ratios. Even though each different blockage ratio shares a similar pattern of increasing pressure drop, the 2 scale foam shows a greater pressure drop compared to the larger scales with 4 and 6. This is attributed to the high numbers of ligaments in the 2 scale foam as compared to the rest. The pressure drops of 2 scale foam with a blockage ratio of 0.3 also recorded a higher value compared to the higher blockage ratio of 0.6 and 0.9. The result also shows that the foam with the largest pores, e.g., 6 scale induces smaller pressure drops as expected, since lesser restrictions to the airflow as compared to the foams with 2 and 4 scales. Furthermore, using a higher inlet velocity of 3.0 and 5.0 m/s cause more significant pressure drops as compared to the pore sizes. As the fluid velocity increases, the frictional resistance between the fluid and the ligament surfaces increases. The higher velocity results in more turbulent flow and a greater amount of fluid encounters the ligament surfaces and increases the frictional resistance. This increased frictional resistance contributes to a higher pressure drop. Moreover, the increases in velocity also increase the viscous drag force and oppose the fluid flow, contributing to the pressure drop. Thus, smaller pores and higher fluid velocities can lead to greater frictional resistance and higher pressure drop. Lu, Zhang, and Yang (2016), who used the Brinkman-extended Darcy model to characterize the pressure drops of metal foam also found the same trend as in this research, where the pressure drop is increasing with the decreasing pore diameter. By optimizing the pore diameter and surface, it is possible to minimize the pressure drop effects. Other factors such as the shape of the pores, as well as the viscosity and the fluid properties, may also affect the pressure drops in the channel.

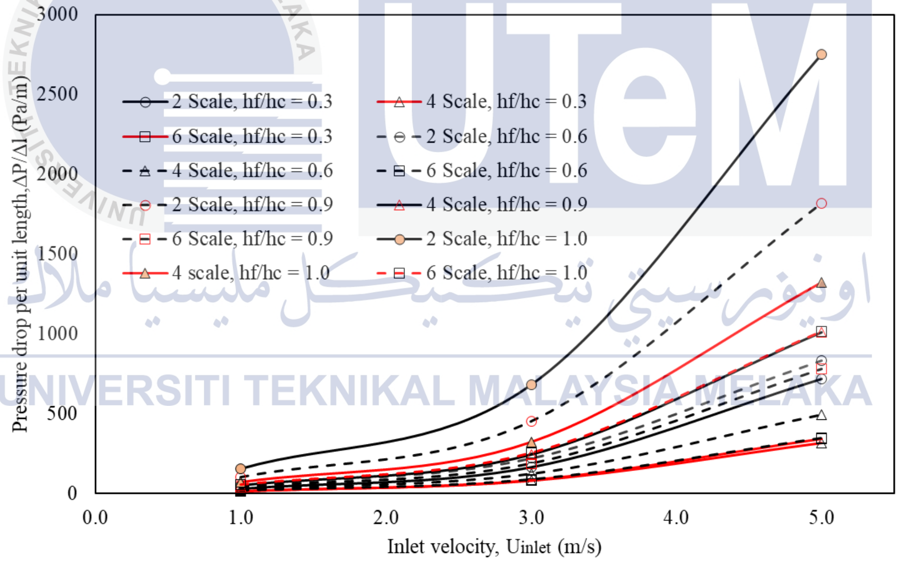


Figure 4.17: Pressure drops of 3D printed open-cell foam with various pore diameters and blockage ratios



The pressure drops between the 3D printed foam and open-cell metal foam (OCMF) are also investigated. The OCMF has a pore density, of 10 and 30 PPI and partially filled the channel. The pressure drops effects from both types of foam with different materials, pore sizes and blockage ratios share a similar trend, where the pressure drop is increasing with the inlet velocity and blockage ratio. This comparison shows similar trends with acrylic blocks. However, the 3D printed foam illustrated a higher pressure drop than 10 PPI open-cell metal foam, even though its pore diameter is smaller. Therefore, the 10 PPI open-cell metal foam also shows an appealing finding as the pressure drop tends to be almost in line with the 3D printed foam with 4 and 6 scale foams. In this case, the ligament thickness of 3D printed foam also plays an important role in increasing the pressure drop, as its size is also increasing with pore diameters, unlike the conventional OCMF. However, the 30 PPI OCMF has a higher pressure drop than 4 and 6 scale foams but lower than the 2 scale foam. At first, it can be seen as the blockage ratio contributes to the values of pressure drop, if compared to only the 10 PPI OCMF. But the effects of a pore diameter of 30 PPI become significant since the induced pressure drop is higher than the 4 and 6 scales though those 3D printed foams have a slightly higher blockage ratio of 0.3.

A comparison with an existing study by Jadhav et al. (2021) is shown in Figure 4.18. The partially filled tube with a blockage ratio of 0.4 using 10 PPI aluminium foam shows a higher pressure drop than the 10 PPI used in this research when comparing at the same inlet velocities of 1.0 to 3.0 m/s. However, the difference could be attributed to the type of setup – a circular tube, a variation in the pore sizes and also a slightly higher blockage ratio of 4.0. Besides the pressure drop effects, it is also important to note that a small pore foam with high numbers of ligaments can drive the flow into free spaces, which can affect the flow behaviours at the interface and free stream region of a partially filled channel. As a result, the use of small pore foam can have a significant impact on the heat and mass transfer characteristics, as well as the overall performance of the channel.

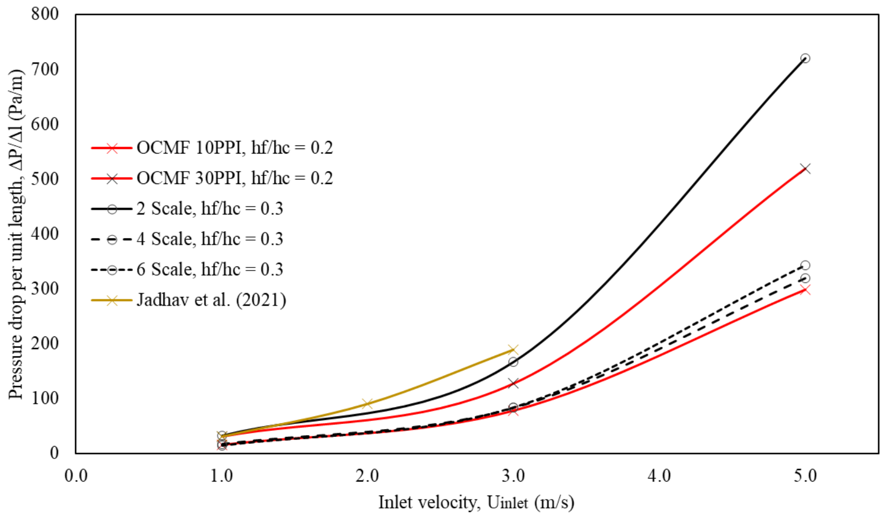


Figure 4.18. Comparison of pressure drops between 3D printed foams and open-cell metal foam

## 4.4 Regression analysis and slip velocity

A model of slip velocity for the partially filled configuration with OCMF has been proposed in this research. The model for a slip velocity was formulated by applying a regression analysis with the possible dimensionless group, obtained from the dimensional analysis using Buckingham π theorem. The key parameters that have been considered in this research are slip velocity, inlet velocity, air velocity in the unloaded wind tunnel, channel height, foam height, pore diameter, ligament diameter, permeability, fluid density, fluid dynamic viscosity and pressure drop per unit length. The analyses were conducted by using a trial-and-error method with no agreement in the literature regarding the typical length characteristics in the partially filled configuration of the open-cell foams where it could be considered from the channel, foam geometry and microstructure. In the multi-linear regression analysis in this research, the confidence interval was set up at 95% of the confidence interval and resulting in a possible P-value $< 0.05$ with the adjusted $R^2 = 0.88$. It was expected that $R^2 < 0.9$ since there are a lot of variables that should be considered which influence the slip velocity at the interface region. Replication of data also occurred during the regression analysis since a trial and error method is used in considering the dependable parameters to generate the slip velocity correlation. The regression results show the dimensionless groups used in Equation (4.1) were statistically correlated with the slip velocity as the dimensionless group showed a P-value < 0.05. The correlation is from the 3D printed foam data set which is twice or larger than 5 PPI metal foam. The correlation is testified using the data set gathered from the 10 and 30 PPI metal foam to ensure the agreement with the experimental studies. However, it should be adjusted by multiplying the constant with "4.5" for the slip velocity model to fall within the uncertainties of the experimental studies. This is one of the steps in the dimensional analysis that used factorial constant when formulating the correlation. In regression analysis, it also shows the ligament diameter, $d_l$ also plays an important role compared to pore diameter, $d_p$ as the P-value of dimensionless group relating to the ligament diameter, $d_l$ is lower than 0.05 compared to the dimensionless group using pore diameter, $d_p$.



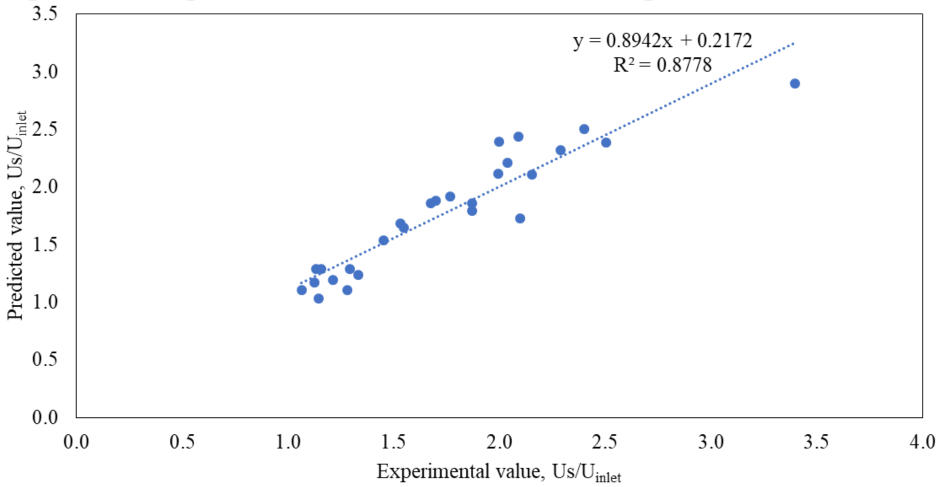


Figure 4.19. Experimental against predicted slip $U_s/U_{inlet}$ of 3D printed foam

The correlation of slip velocity for a partially filled channel with OCMF is expressed as follows:

$$\frac{U_s}{U_{inlet}} = 79.25 \times \left( \frac{\frac{\Delta P}{\Delta l} h_c^2}{U_{inlet}^2 \rho} \right)^{0.46} \times \left( Re_{h_c} \right)^{0.07} \times \left( \frac{h_f}{h_c} \right)^{0.44} \times \left( \frac{d_l}{h_c} \right)^{0.31} \times \left( \frac{K}{h_c^2} \right)^{0.34} \tag{4.1}$$

Thus, the slip velocity for OCMF has been estimated using the proposed model. The correlation between dimensionless slip velocity versus pore diameter per the foam height from experimental data, predicted model and existing literature are shown in Figure 4.20. The slip velocity estimated using the predicted model is lower than the experimental data in the partially filled channel with OCMF. Several past studies that related to the slip velocity are compared to the results of this result. Nair and Sameen (2015) who have used two different porosity and inlet velocity where there was a model with 0.88 porosity running with 5.1 m/s of inlet velocity, $U_{inlet}$ and the other model with 0.65 porosity running with $U_{inlet,}$ 3.88 m/s. The study by Nair and Sameen (2015) shows both setups with different porosity and pore diameter from are underpredicted the slip velocity for the OCMF. A data set from Shikh Anuar et al. (2018) tends to scatter accordingly to the x-axis, pore diameter per foam height while one of the data sets tends to approximately have a similar $U_{slip}/U_{inlet}$ at pore diameter per foam height nearest to 0.1. Both numerical and analytical studies from Lu et al. (2016) and Jadhav et al. (2020), also found that their data set was placed a bit away can be lower and also higher than the experimental data of OCMF. Therefore, the analytical data set for smaller pore diameter (1.27 - 5.08 mm) from Lu, Zhang, and Yang (2016) tends to be lower than the present experimental data of $U_{slip}/U_{inlet}$ but almost in the range of the $U_{slip}/U_{inlet}$ with the proposed model using the metal foam's properties.

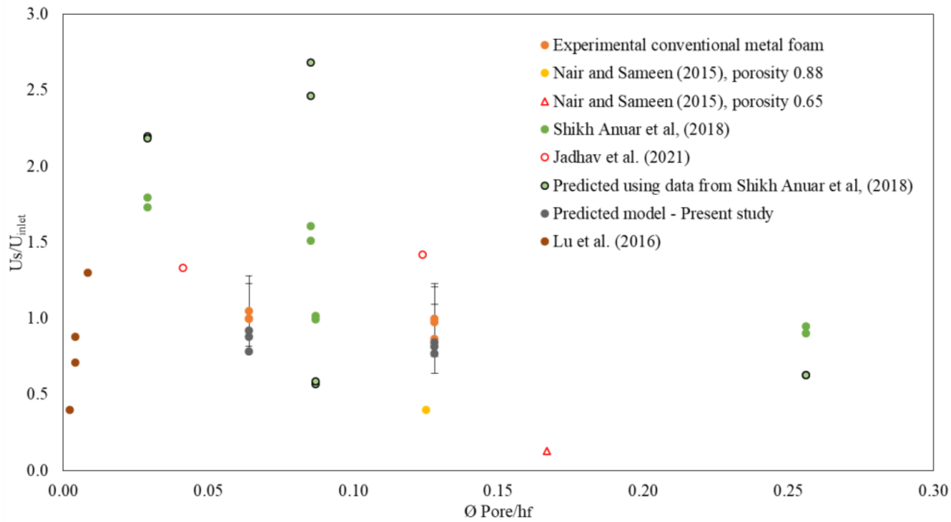


Figure 4.20. Comparison of dimensionless slip velocity against pore diameter between experimental data, predicted model and existing literature

## 4.5 Fluid flow simulation

### 4.5.1 Flow behaviours across partially filled channel

A simulation using Computational Fluid Dynamic (CFD) analysis is done to validate the experimental data obtained in the wind tunnel. The CFD analysis was configured according to the operation of the wind tunnel and foam properties. The results of flow behaviours in the free stream region and pore velocity due to the effect of blockage ratio are discussed alongside the slip velocity at the interface region. The analysis is presented as the velocity streamlines with different colours that indicate the velocities in the specific region or areas. The velocity distribution in five different regions, (1) upstream, (2) free stream, (3) interface, (4) porous and (5) downstream are analyzed.

Figure 4.21 shows the result from CFD analysis inside the wind tunnel with partially filled porous foam at a blockage ratio of 0.3. The streamlines at the upstream region remain the same with purple or orange colour with a different velocity magnitude that varies with the inlet velocity setup until the fluid flow approaches the porous structure. The light blue colour represents a lower air velocity with a range of 0 – 1.0 m/s. Meanwhile, the orange colour represents a higher air velocity, from 1.2 – 7.4 m/s. The maximum velocity region is shown in the free stream region which is started from the interface region towards the upper part of downstream region. The flow direction in Figure 4.21 is illustrated from left (channel inlet) and reach the right side (channel outlet). The fluid flow at the upstream region also shows a uniform velocity distribution the same as a turbulence flow where the flow tends to have a uniform velocity magnitude across the region. Mostly, the colour of the streamlines varies with the inlet velocity. The upstream region produces the highest velocity at about 0.9 m/s, 2.5 m/s and 4.3 m/s for 2 scale foam while the lowest at 6 scale foam, 0.8 m/s, 2.3 m/s and 3.9 m/s. The streamlines show a variation of velocities in the upstream region for each foam with varied pore diameters, where the 2 scale foam has the highest velocities compared to 4 and 6 scale foams. However, the flow velocity is decreasing as the fluid enters the porous region and tends to reduce along the porous foam length and producing the lowest velocity magnitude at the rear end of the foam. As an example for 4 scale foam, the velocity at the entrance of foam recorded the same as the upstream region, 0.8 m/s, 2.5 m/s and 4.1 m/s but when reaching the end of foam, it produces a velocity of about 0.4 m/s, 1.2 m/s and 2.1 m/s. The reduction of velocity may cause ligament structure in the porous region giving a restriction to the flow velocity inside the porous region. The reduction of velocity inside the porous region due to the structure of the ligament also can be justified by comparing the velocity inside the porous foam that has different upscaling sizes. A smaller scale foam will have more ligament structure to fill the foam printing dimension. A study by Yerramalle, Premachandran, and Talukdar (2021) also observed a decrease in fluid velocity along the porous structure until the flow reached the center of the foam (with a porosity of 0.8). The 3D printed foam presented in this research is also different from OCMF. In OCMF, increasing the pore diameter reduces the ligament thickness. However, for foams (2, 4 and

6 scales), increasing the pore diameter also increases the ligament thickness, assuming that the overall size remains constant. In these cases, the larger pore diameter used for the porous foam will resulting a decrease in the number of ligaments structure in order to maintain the exact overall size of foam according to the channel size. Thus, more collisions between the fluid with the ligament's structure will occur at a smaller foam scale.

On the interface region, the analysis for every foam with a blockage ratio of 0.3 that varies with inlet velocity, shows the presence of fluid velocity is lower compared to the upstream region. The interface velocity shares the same velocity as the upstream region where the highest is also produced from 2 scale foam. The fluid flow on the free stream region also tends to move along the x-axis until reaching the rear ends of the porous foam while having a little bit gradually increasing of velocity that represents different streamlines colours. The varied velocity at the free stream and interface region can be seen starting at the region above the foam frontal area. The highest velocity at the free stream region is located a few millimeters above the interface region. The highest velocity range illustrated by the streamline colour that varies with the inlet velocity is; (1) 1.2 - 1.5 m/s at $U_{inlet}$ = 1.0 m/s, (2) 3.5 - 4.6 m/s at $U_{inlet}$ = 3.0 m/s, and (3) 5.8 – 7.4 m/s at $U_{inlet}$ = 5.0 m/s. Some of the fluid particles tend to evade the porous structure and slide to the free stream region. Thus, it gives additional forces to create the highest velocity magnitude in the free stream region, toward the end of the partially section. Therefore, there is also fluid particle entering the porous region while exiting at the interface region. In the downstream region, the flow velocity has the same velocity magnitude as the flow in the rear ends of porous foam. The values are about 0.2 m/s, 0.6 m/s and 1.1 m/s for 2 scale foam with $h_f/h_c$ = 0.3, with slightly smaller values for 6 scale foam of the same blockage ratio. The highest velocity downstream that occurs at the region after the free stream region is observed at 1.5 m/s, 4.6 m/s and 7.4 m/s for 2 scale foam while for a bigger foam (6 scale), it induces a velocity at 1.4 m/s, 3.5

m/s and 5.8 m/s. The streamlines show the fluid tends to remain in the flow pattern from the middle part where there is also no occurrence of a recirculation zone at the downstream region. By comparing the upstream and downstream regions, ones can observe that the velocity at downstream is mostly higher compared to the upstream region which is illustrated by foam with 2 and 4 scale pore sizes. A transition from a purple colour (0.6 – 4.3 m/s) to an orange-yellow colour (1.2 – 7.4 m/s) from the upstream to downstream regions. A study by Tang, Wang, and Huang (2023) stated that the transition of the velocities pattern could be due to the increase of Reynolds number in the flow that contributes to a turbulence phenomenon. It also needs to understand that there are a few parameters that may influenced the Reynold number such as air velocity, hydraulic diameter and others.

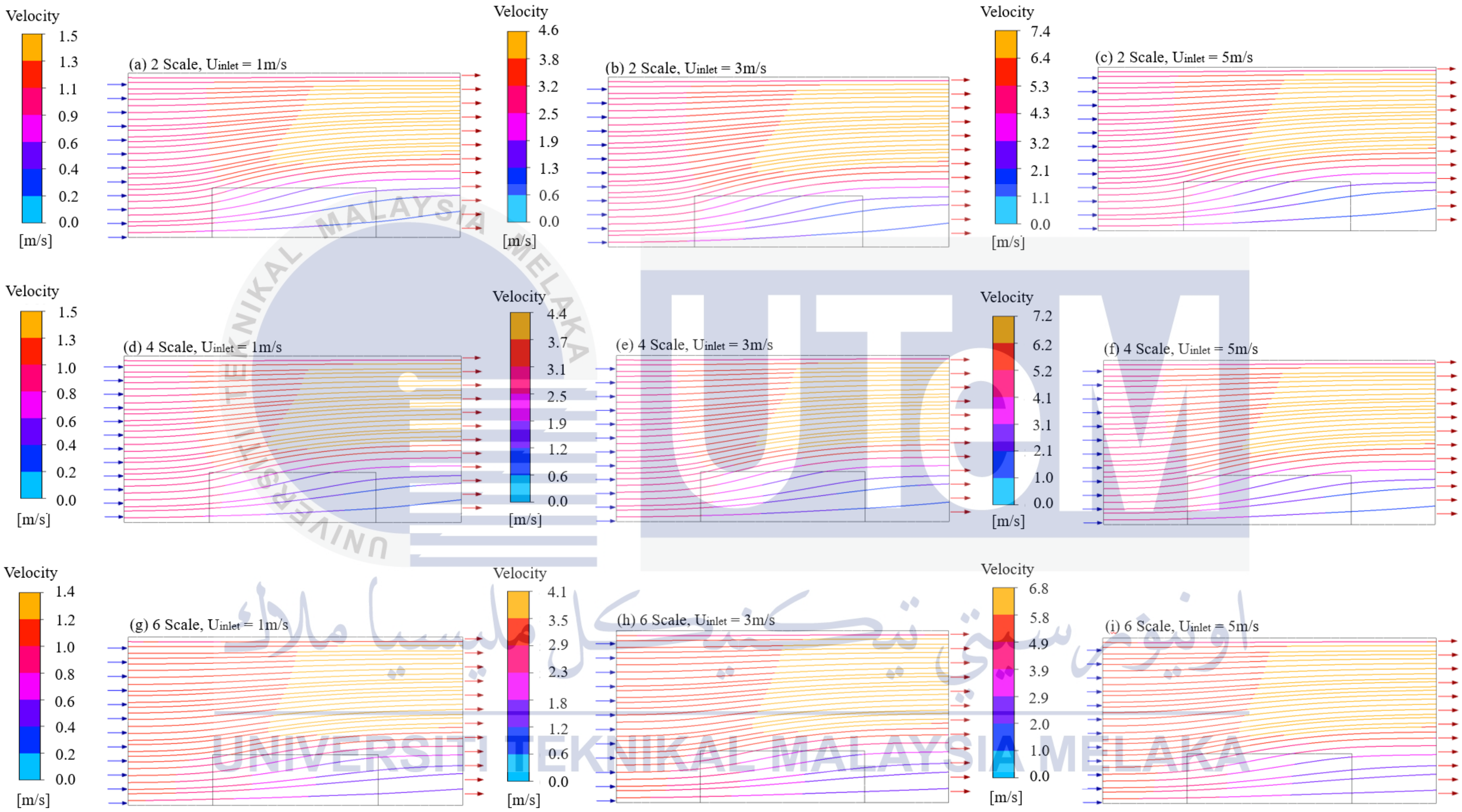


Figure 4.21: Velocity streamlines for blockage ratio of 0.3 at different inlet velocities and pore diameters

Meanwhile, Figure 4.22 (a) – (i) shows the CFD analysis with the presence of foams with a blockage ratio of 0.6 in the middle of the channel. At a foam with a blockage ratio of 0.6, the velocity at the upstream region shows a higher velocity compared to the foams with a 0.3 blockage ratio. The highest velocity for streamlines at a blockage ratio of 0.6 contributes about 20% higher compared to the cases with a blockage ratio of 0.3. The streamline at the upstream region also shows the lowest velocity occurs at 6 scale foams about 1.0 m/s, 3.0 m/s and 4.9 m/s. Meanwhile, the velocity distribution is also similar to the previous 0.3 blockage ratio, which illustrated a constant velocity distribution in the region. In the porous region, the 2 and 4 scale foams with blockage ratio 0.6 also produce the same situation as in 0.3 blockage cases where the velocity also varies from the entrance until reaching the rear end but the 6 scale foams showing a constant velocity distribution at 0.8 m/s, 2.4 m/s and 3.9 m/s. However, there is still a reduction of velocity from the upstream region that occurs at the entrance of the porous region. The fluid also passes through the interface region, suggesting the presence of slip velocity at that specific region which is following the BJ theory. The velocity streamlines show that the pore velocity keeps increasing until reaching the upstream region velocity (that is parallel to the interface region) as the fluid exits the foam. The 4 scale foam at the interface region recorded a velocity of about 1.2 m/s, 3.6 m/s and 6.0 m/s. The CFD analysis also shows the porous foam with 0.6 blockage ratio cases producing high velocity compared to the 0.3 blockage ratio cases that resulted in 23% higher from comparing the highest velocity for both blockage ratios. The velocity inside the porous region shows different characteristics, which depends on the pore sizes. The foams with 2 and 4 scale have a reduction of velocity magnitude as the fluid reaches the rear end of the foams. The ligament's structure easily blocks the fluid path and some fluid particles may collide with the ligament and contribute to the loss of fluid momentum. The fluid also continues to lose kinetic energy from the collision with the ligament structure that has been dragged with the friction on the ligament's surfaces (Park, Seo, and Jeong, 2020). The velocity at the downstream region also shows the same pattern as foam with a blockage ratio of 0.3, where a portion of the flow is continuously moving from a region at the rear of the foam and then entering the downstream region. A bit different from the blockage ratio of 0.3, the 2 scale foam with a blockage ratio of 0.6 still has a reduction of velocity at the region behind the rear foam. The reduction of velocity may reach a velocity at 0.3 m/s, 0.8 m/s and 1.4 m/s.

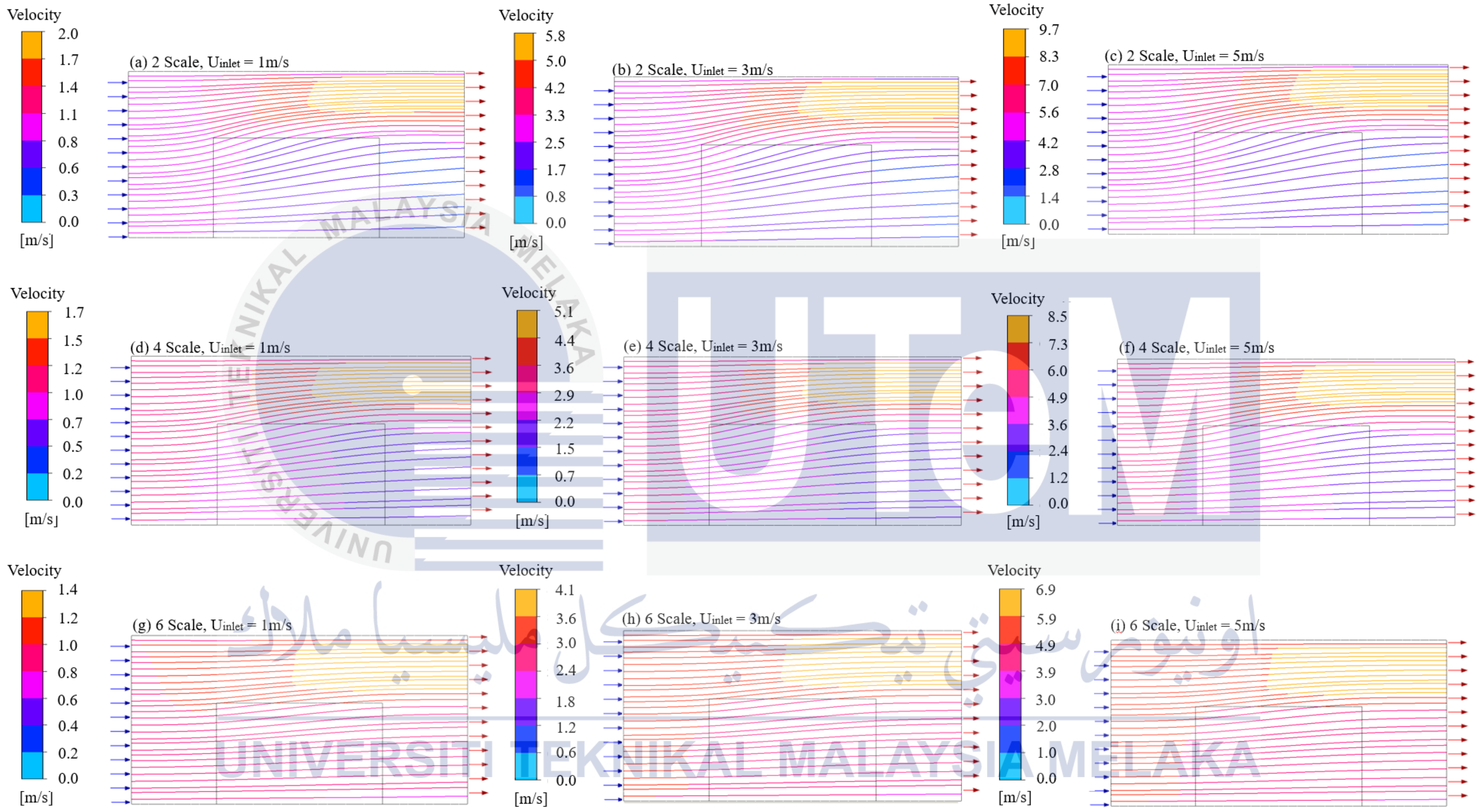


Figure 4.22: Velocity streamlines for blockage ratio of 0.6 at different inlet velocities and pore diameters

For the installation of a porous foam with a blockage ratio of 0.9, the free stream region height is 10 mm, 1/10 of the channel area which is illustrated with the analysis in Figure 4.23 (a) – (i). The streamline in the upstream region also shows a constant velocity distribution similar to the foams with a blockage ratio of 0.3 and 0.6. The highest velocities recorded by the streamline at the upstream region are 1.2 m/s, 3.5 m/s and 5.9 m/s which is at the foam with a 2-scale factor. Meanwhile, the lowest velocity is produced from the biggest pore diameter foam, 6 scale which is about 0.8 m/s, 2.4 m/s and 4.1 m/s. Furthermore, the velocity inside the porous region also has a constant distribution with the same pattern and velocity magnitude as the upstream region. A contrast to the smallest blockage ratio of 0.3 and 0.6, the velocity is having a tendency to flow at a constant velocity along the foam length until reaching the rear ends. Since a majority of the channel is filled with porous foam, the fluid tends to flow as normal by forcing itself to enter the porous region. Thus, the ligament structure no longer restricted the fluid movement inside the porous region as a huge force also formed at the area behind the porous region since the centrifugal fan sucked the air to be recycled inside the closed loop wind tunnel system. Meanwhile, at the middle part of the foams, the fluid velocity in the free stream region and interface region is still higher compared to the velocity at the porous region and the upstream region, which is different from the other cases, with a blockage ratio of 0.3 and 0.6. Sauret, Abdi, and Hooman (2014) also found the interface velocity is very high when the fluid first got into the porous medium but then sharply drops along the flow path since a significant part of the flow tried to avoid the porous region. Banjara and Nagarajan, (2020) also mention the occurrence of higher velocity at the interface region due to lesser restrictions offered to the fluid in the open space of the channel. At the highest velocity, foams with 2-scale factor show the velocity magnitude at 1.7 m/s, 5.3 m/s and 8.8 m/s. The fluid flow also tends to reach the top wall of the channel, and when in contact, it is at no-slip condition, (U = 0). By observing the colour in the free stream region, one can notice a transition colour from orange turns to yellow when approaching the free stream region above the rear edge of the foams. It shows a reduction in fluid velocity since the fluid is entering a bigger clear region at the downstream region. As ones could understand, a bigger surface area of a clear region may result in a lower velocity since the surface area and velocity are related to each other. Lastly in the downstream region, the fluid flow behaviour remains the same with other foams with $h_f/h_c$ = 0.3 and 0.6, where the velocity is the same as the velocity at a region located at the rear edge of the foams. At 4-scale foam, the streamline behind the porous region illustrated a velocity at 1.1 m/s, 3.3 m/s and 5.5 m/s and also the same with the upstream and porous region.

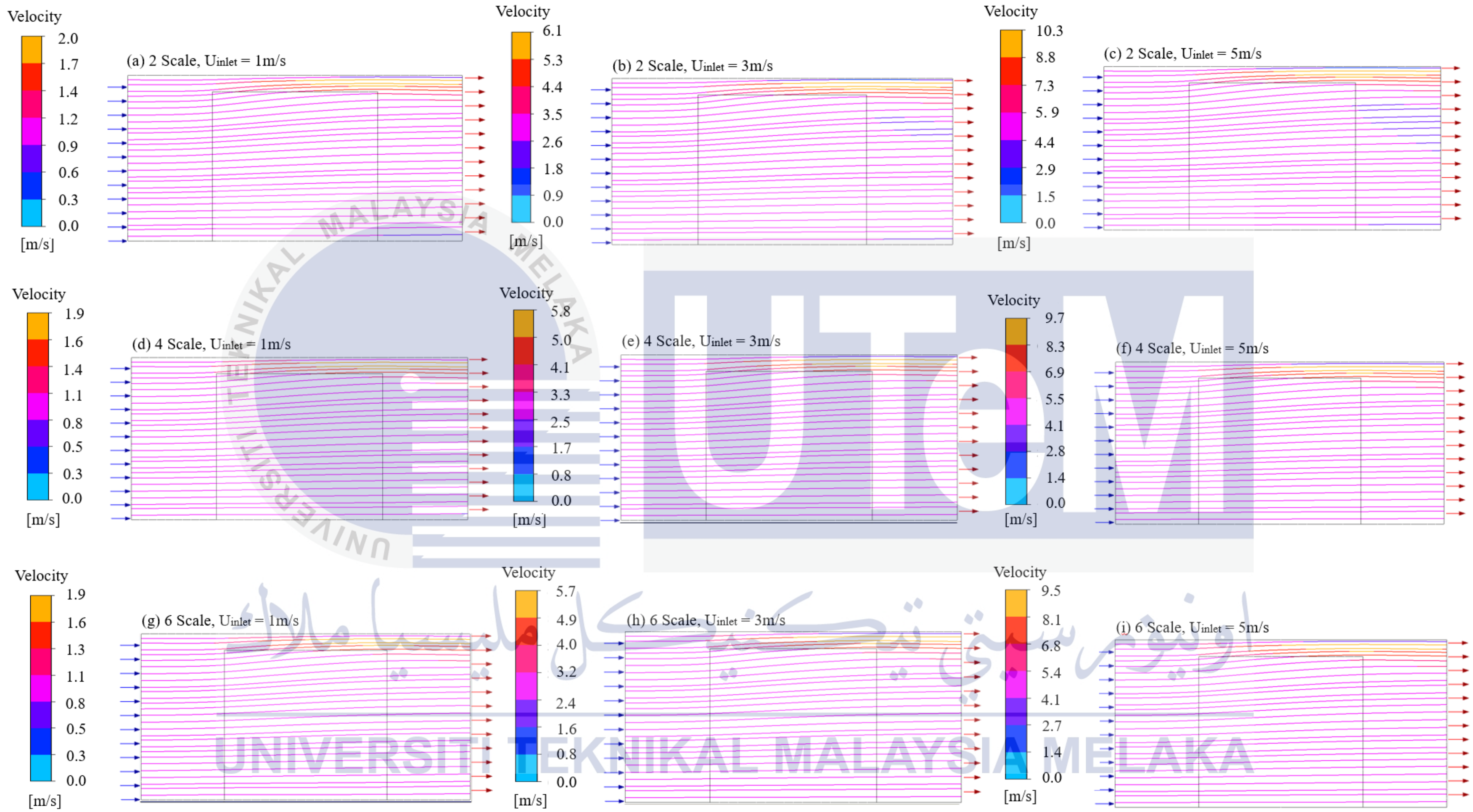


Figure 4.23: Velocity streamlines of blockage ratio 0.9 at different inlet velocities and pore diameters

### 4.5.2 Slip velocity at the middle of partially filled channel

Figure 4.24 shows a comparison between the CFD analysis and experimental studies in the middle of the partially filled section. The middle location was chosen as a comparison to the single value, obtained from the predicted model. The velocity profile result from the CFD analysis shares the same data set values with the velocity streamlines in the previous discussion. However, the velocity profile tends to have specific data set values of the fluid particles in the vertical direction, crossing the channel height. In Figure 4.24 (a) – (c), the velocity profile at the interface region shows the experimental data is higher compared to the CFD analysis. There are a bit differences when comparing the velocity profile for CFD analysis to the experimental studies where the maximum percentage of difference can be reached at 64 % which is for 2 scale foam with a blockage ratio of 0.9 at $U_{inlet}$ = 1 m/s. The difference is expected as more contribution factors may appear in the experimental investigation that cannot be demonstrated in the CFD analysis. To ease the CFD simulation, a few assumptions need to be considered e.g. isothermal, homogeneity and others that may not represent a real case of the experimental study. Most of the velocity from the experimental studies increases slightly and reaches the highest magnitude at the free stream region while the velocity from the CFD analysis tends to increase drastically and then both fluid flow for experimental and CFD analysis continues to decrease until reaching the top wall of the wind tunnel channel.

By comparing both data sets (experimental and CFD studies), ones can observe the differences in data values between the two types of studies. The difference in the CFD analysis at the interface region is too small so that the velocity trendline can be seen to be in line for each inlet velocity case and can be differentiated with the different pore diameters compared to the experimental study that easily can be identified. The velocity in the CFD analysis at blockage ratios 0.3 and 0.6 show the foam with a larger pore diameter is higher compared to the smaller one (2 scale) at the interface region but at a blockage ratio of 0.9, the velocity for every foam at the interface region remains constant at 1.1 m/s. Some factors possibly attributed to the results of velocity at blockage ratio 0.3 and 0.6; (1) the exiting fluid through the pore at the interface region and (2) the number of ligament structures inside the porous region. A bigger pore diameter can enable the fluid to exit into the interface region and drive the fluid particle to accelerate more. The presence of ligament structures also may hinder a part of the fluid particle from reaching the interface region. By comparing the experimental data with CFD's, it shows that the flow will remain passing through the porous structure but with the fluid that exits into the interface region, the velocity will become smaller and can be neglected for a case with more ligament structure. Hence, it solves the situation that occurs for a blockage ratio of 0.9 where the velocity remains constant at the interface. From observing with difference blockage ratio, it is also shown that the increment blockage ratio for each foam will be resulting in increasing in fluid velocity at the interface region.

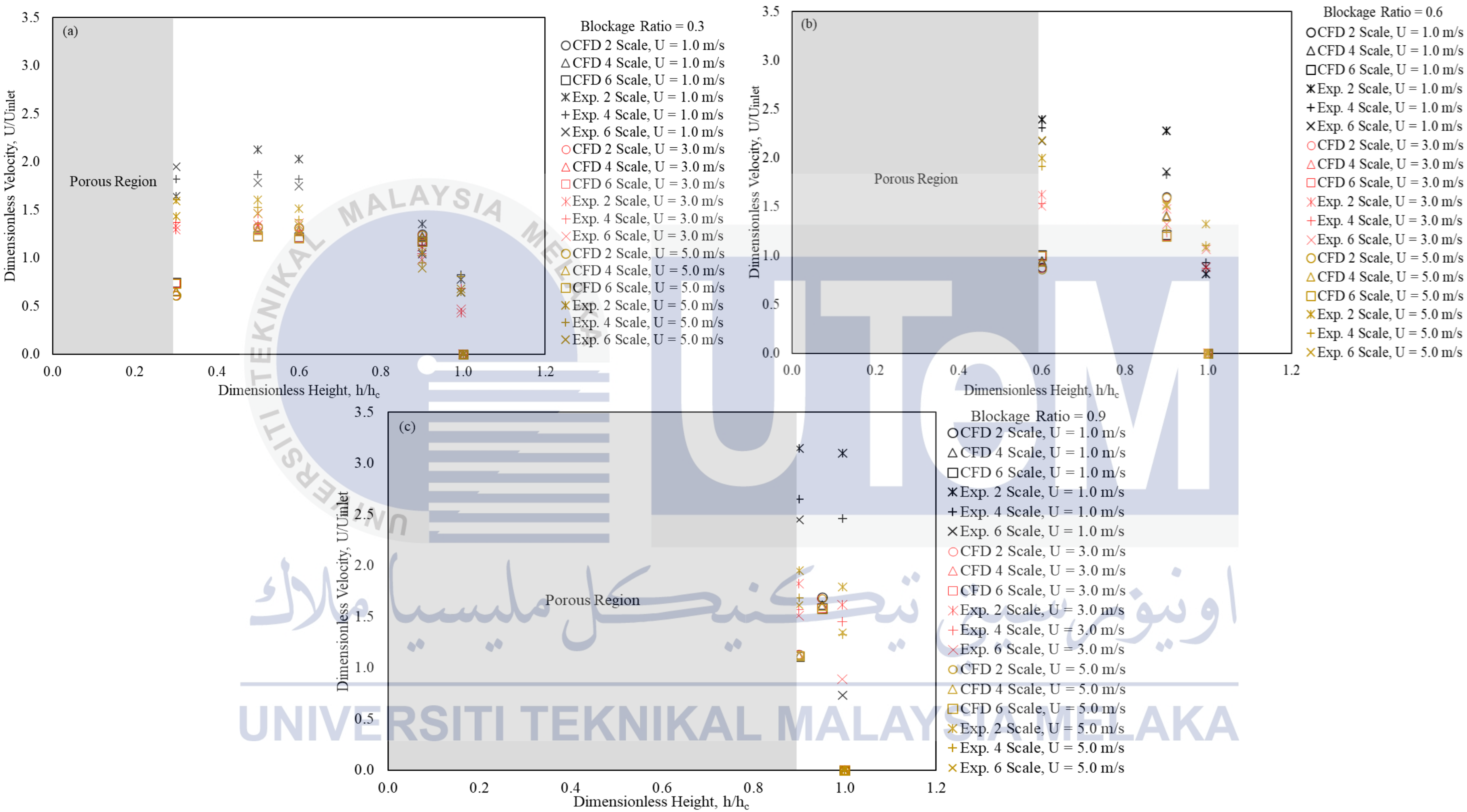


Figure 4.24: Comparison of velocity profiles between CFD analysis and experimental data at the middle of partially filled channel

Figure 4.25 illustrated the comparison between the experimental, predicted model and simulation results along the dimensionless variable (pore diameter per foam length, $l_f$). The data set from 10 and 30 PPI open-cell metal foam (OCMF) is also included. The CFD analysis has an almost "4.5 times" lower value when compared to the experimental and predicted velocity for 10 and 30 PPI open-cell foam as shown in Figures 4.25 (a) and (b). The slip velocity model that used an averaging value has slightly underpredicted the real phenomenon at the interface region with 0.13 % of maximum percentage difference when compared to the experimental data. Meanwhile, Figure 4.25 (d) shows the collection of all OCMF with different $U_{inlet}$ for experimental, predicted and CFD analysis. The major differences are attributed to the uses of 2D CFD model where the simulation may not be capable of analyzing the exact effects of resistance from the open-cell foam since only the properties such as porosity, inertial and viscous coefficients were taken into account. There is no exact structure in defining the size of ligaments and pores which also may be a significant influence on the analysis. Therefore, the porous model (k-ε turbulence model) inside the CFD analysis cannot capture the real phenomenon in the free stream region compared to the experimental study. Moreover, the predicted model shows a closer value to the experimental than the CFD when investigating the 10 PPI foam while at $U_0$ = 1m/s, the value from the model falls within the experiment uncertainties. It shows the capabilities of the model in estimating velocity on the interface region for a foam with smaller pores, i.e. 10 and 30 PPI. When comparing with different inlet velocities, ones can see the experimental studies will become closer to predicted values. Averaging the slip velocity in the CFD simulation underestimates the real phenomenon in the open-cell metal foam (OCMF). Thus, the estimation of slip velocity can rely on the slip velocity model generated in this study where the model will estimate the average values of slip velocity but the experimental studies are also very important since it will be describing a full range of the real slip velocity cases.

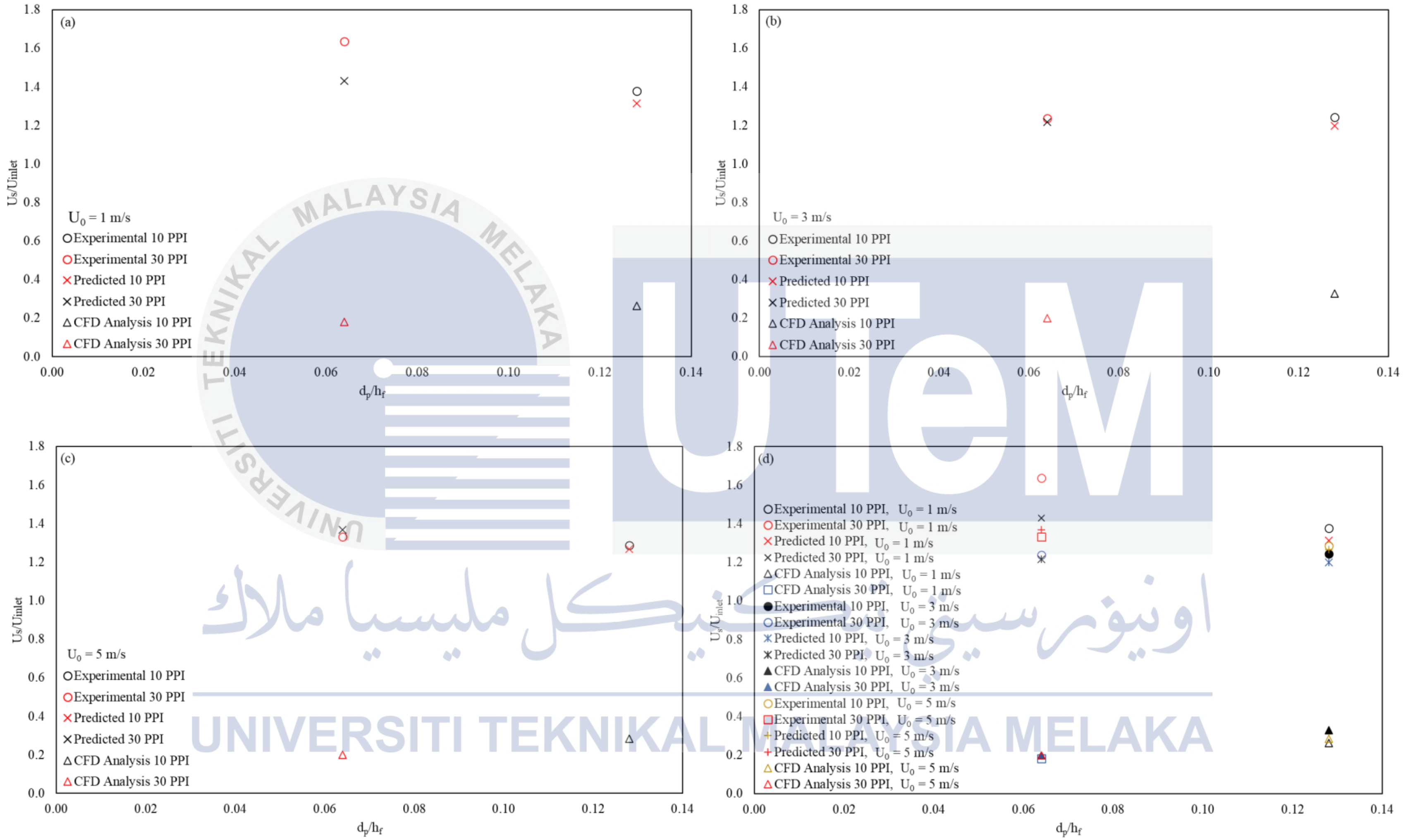


Figure 4.25: Comparison of slip velocity at the interface of porous-clear region between CFD analysis, experimental values and predicted model at different velocities: (a) 1.0 m/s, (b) 3.0 m/s, (c) 5.0 m/s and (d) 1.0 – 5.0 m/s

# CHAPTER 5

# CONCLUSION AND RECOMMENDATIONS FOR FUTURE RESEARCH

This chapter briefly concludes the findings of the whole research while providing the recommendations for achieving a better solution in the future works. It is concluding all objectives for this research is successfully achieved through the recommended method and procedure for this research.

## 5.1 Conclusion

The open-cell foams that were produced using SLS method have a smoother surface compared to the ones produced by FDM. A reverse engineering method was conducted starting from preparing the CAD design until producing the open-cell foam structure using the AM methods. The dimensions of the 3D printed foams were manipulated to fully and partially filled the channel. The properties of 3D printed foams have been determined through experimental measurement or calculation. The open-cell foams with scaling factors of 2, 4 and 6 have a porosity in the range of 0.88 - 0.94 while the permeability is ranging from $0.0304 \times 10^{-8}$ to $7.3915 \times 10^{-8}$ $m^2$.

The flow characteristics has been experimentally investigated inside a closed loop, small-scale wind tunnel using a partially filled configuration. The experimental studies discussed four different regions that have possibly been affected by the presence of porous structures. In summary, different blockage ratios and pore diameters affect the fluid velocity inside the wind tunnel. The velocity at the interface region or mainly called slip velocity also can be measured experimentally using the setup and then used to achieve objective 3. The fluid velocity in the upstream, middle or downstream regions gradually shows an increasing pattern with the increases of blockage ratio and the decreases in pore size. In addition, the pressure drops have also been investigated experimentally along with the fluid characteristics due to the effect of the presence of porous structure which may be affecting the fluid velocity. The result shows that the pressure drop increases with higher inlet velocity, higher blockage ratio and smaller pore diameter. The fluid flow characteristics are then validated with a 2D CFD analysis.

The main aim of this research is achieved from objective 3, which is to propose a predicted model for slip velocity at the interface of the foam-fluid region. Two methods have been used in proposing the predicted model, which are the dimensional analysis and regression analysis. A few relatable parameters are selected during the dimensional analysis and then constructed into a few dimensionless groups. The dimensionless group has been considered in the regression group and the slip velocity model was formulated using a regression analysis with the computed value of adjusted $R^2 = 0.86$ and P-value $< 0.05$. The observation shows the predicted and experimental values of the slip velocity at the interface of open-cell metal foam are in agreement since the predicted value falls within the measurement uncertainties. The proposed model can determine the slip velocity of a partially filled channel with open-cell metal foam with a pore diameter equal to and smaller than 5 PPI (5.77 mm).

## 5.2 Recommendations for future works

In consideration for future work, the open-cell foam structure could be produced for metallic materials using technology such as Direct Metal Laser Sintering (DMLS) or coated with metallic substances. The approach has been suggested to follow the real cases of study where the heat transfer also may be applicable and capable to be investigated. However, the surface roughness also needs to be investigated further if a different technique is used to produce the open-cell structure. The foam with its original size (5 PPI) or smaller could be successfully produced due to the use of different materials, e.g., metallic is stronger than nylon. However, the pore structure must be observed whether there is a blockage inside the structure that may affect fluid flow. Meanwhile, the measuring apparatus also can be changed with others such as Particle Image Velocimetry (PIV), and Laser Doppler Anemometry (LDA), despite only using the hot wire anemometer. Besides, the CFD analysis also could be performed with a 3D model to illustrate the flow behaviours in the porous structure better. The reconstructed images of open-cell foam in meshes or surface form should be changed to a solid object before being imported into the ANSYS software to make the process of simulation to become easier and more fluent.

## REFERENCES


ASTM D6011-96., 2022. *Standard Test Method for Determining the Performance of a Sonic Anemometer/Thermometer*.

Adekanye, S. A., Mahamood, R. M., Akinlabi, E. T., and Owolabi, M. G., 2017. Additive manufacturing: The future of manufacturing. *Materials and Technology*, 51 (5), pp. 709-715.

Ahmed, H. E., Fadhil, O. T., and Salih, W. A., 2019. Heat transfer and fluid flow characteristics of tubular channel partially filled with grooved metal foams. *International Communications in Heat and Mass Transfer*, 108, pp. 104336.

Alomair, M., and Tasnim, S. H., 2018. Experimental measurements of permeability of open foam. *International Conference on Fluid Flow, Heat and Mass Transfer*, 186, pp. 186.

Alvandifar, N., and Amani, E., 2018. Partially metal foam wrapped tube bundle as a novel generation of air cooled heat exchangers. *International Journal of Heat and Mass Transfer*, 118, pp. 171–181.

Amin, K. F., and Rashed, H. M. M. A., 2019. Steel Used in Construction Industries. *Reference Module in Materials Science and Materials Engineering*.

Anuar, F. S., Malayeri, M. R., and Hooman, K., 2017. Particulate Fouling and Challenges of Metal Foam Heat Exchangers. *Heat Transfer Engineering*, 38 (7 – 8), pp. 730–742.

Arbak, A., Dukhan, N., Bağcı, Ö., and Özdemir, M., 2017. Influence of pore density on thermal development in open-cell metal foam. *Experimental Thermal and Fluid Science*, 86, pp. 180–188.

Atangana, A., 2018. Principle of Groundwater Flow. *Fractional Operators with Constant and Variable Order with Application to Geo-Hydrology*.

Banerjee, A., and Pasupuleti, S., 2019. Effect of convergent boundaries on post laminar flow through porous media. *Powder Technology*, 342, pp. 288–300.

Banhart, J., 2000. Manufacturing routes for metallic foams. *Jom*, 52 (12), pp. 22–27.

Banjara, K., and Nagarajan, G., 2020. Nuances of fluid flow through a vertical channel in the presence of metal foam/solid block – A hydrodynamic analysis using CFD. *Thermal Science and Engineering Progress*, 20 (February), pp. 100749.

Bastos Rebelo, N. F., Andreassen, K. A., Suarez Ríos, L. I., Piquero Camblor, J. C., Zander, H. J., and Grande, C. A., 2018. Pressure drop and heat transfer properties of cubic iso-reticular foams. *Chemical Engineering and Processing - Process Intensification*, 127 (March), pp. 36–42.

Beavers, S. G., and Joseph, D. D., 1967. Boundary conditions at a natural permeable wall. *Journal of Fluid Mechanics*, 30 (1), pp. 197–207.

BeiHai Composite., 2022. *Open cell aluminum foam.* [online] Available at: https://www.beihaicomposite.com/open-cell-aluminum-foam-annie-product/ [Accessed on 14 February 2024].



Bhattacharya, A., Calmidi, V. V., and Mahajan, R. L., 2002. Thermophysical properties of high porosity metal foams. *International Journal of Heat and Mass Transfer*, 45 (5), pp. 1017–1031.

Bracconi, M., Ambrosetti, M., Okafor, O., Sans, V., Zhang, X., Ou, X., Da Fonte, C. P., Fan, X., Maestri, M., Groppi, G., and Tronconi, E., 2019. Investigation of pressure drop in 3D replicated open-cell foams: Coupling CFD with experimental data on additively manufactured foams. *Chemical Engineering Journal*, 377 (October 2018), pp. 120123.

Brighenti, R., Cosma, M. P., Marsavina, L., Spagnoli, A., and Terzano, M., 2021. Laser-based additively manufactured polymers: a review on processes and mechanical models. *Journal of Materials Science*, 56 (2), pp. 961–998.

Bulat, P. V., and Volkov, K. N., 2020. Simulation of incompressible flows in channels containing fluid and porous regions. *International Journal of Industrial and Systems Engineering*, 34 (3), pp. 283–300.

Chandesris, M., and Jamet, D., 2006. Boundary conditions at a planar fluid-porous interface for a Poiseuille flow. *International Journal of Heat and Mass Transfer*, 49 (13–14), pp. 2137–2150.

Costa, A., 2006. Permeability-porosity relationship: A reexamination of the Kozeny-Carman equation based on a fractal pore-space geometry assumption. *Geophysical Research Letters*, 33 (2), pp. 1–5.

Costanza, G., Del Ferraro, A., and Tata, M. E., 2022. Experimental Set-Up of the Production Process and Mechanical Characterization of Metal Foams Manufactured by Lost-PLA Technique with Different Cell Morphology. *Metals*, 12 (8).

Diani, A., Bodla, K. K., Rossetto, L., and Garimella, S. V., 2014. Numerical analysis of air flow through metal foams. *Energy Procedia*, 45, pp. 645–652.

Dileep, B., Prakash, R., Bharath, H. S., Jeyaraj, P., and Doddamani, M., 2021. Dynamic behavior of concurrently printed functionally graded closed cell foams. *Composite Structures*, 275 (June), pp. 114449.

Dou, H.-S., 2005. Energy Gradient Theory of Hydrodynamic Instability. *Proceeding of The Third International Conference on Nonlinear Science*, Singapore.

Dukhan, N., 2006. Correlations for the pressure drop for flow through metal foam.

*Experiments in Fluids*, 41 (4), pp. 665–672.

Dukhan, N., Bağci, Ö., and Özdemir, M., 2014. Experimental flow in various porous media and reconciliation of Forchheimer and Ergun relations. *Experimental Thermal and Fluid Science*, 57, pp. 425–433.

ERG Aerospace., n.d.. *Metal foam material: Erg Aerospace*. [online] Available at: https://ergaerospace.com/metal-foam-material/ [Accessed on 14 February 2024].

Farah, S., Anderson, D. G., and Langer, R., 2016. Physical and mechanical properties of PLA, and their functions in widespread applications — A comprehensive review. *Advanced Drug Delivery Reviews*, 107, pp. 367–392.

Fengshan, S., Lijun, L., Xianyue, G., Xuejian, J., and Xiangjun, D., 2020. Equivalent model of spatial random array vibration system on sound-absorbing computing for porous material. *Applied Acoustics*, 165, pp. 107299.

Forooghi, P., Abkar, M., and Saffar-Avval, M., 2011. Steady and Unsteady Heat Transfer in a Channel Partially Filled with Porous Media Under Thermal Non-Equilibrium Condition. *Transport in Porous Media*, 86 (1), pp. 177–198.

Gama, N., Ferreira, A., and Barros-Timmons, A., 2019. 3D printed cork/polyurethane composite foams. *Materials and Design*, 179, pp. 107905.

Guo, C., Li, Y., Nian, X., Xu, M., Liu, H., and Wang, Y., 2020. Experimental study on the slip velocity of turbulent flow over and within porous media. *Physics of Fluids*, 32 (1).

Haeri, S., Wang, Y., Ghita, O., and Sun, J., 2017. Discrete element simulation and experimental study of powder spreading process in additive manufacturing. *Powder Technology*, 306, pp. 45–54.

Hajiahmadi, S., Elyasi, M., and Shakeri, M., 2019. Investigation of a new methodology for the prediction of drawing force in deep drawing process with respect to dimensionless analysis. *International Journal of Mechanical and Materials Engineering*, 14 (1).

Hamadouche, A., Nebbali, R., Benahmed, H., Kouidri, A., and Bousri, A., 2016. Experimental investigation of convective heat transfer in an open-cell aluminum foams. *Experimental Thermal and Fluid Science*, 71, pp. 86–94.

Hamidi, E., Ganesan, P., Muniandy, S. V., and Amir Hassan, M. H., 2022. Lattice Boltzmann Method simulation of flow and forced convective heat transfer on 3D micro X-ray tomography of metal foam heat sink. *International Journal of Thermal Sciences*, 172, pp. 107240.

Hollister, S. J., 2006. Porous scaffold design for tissue engineering. *Nature Materials*, 5 (7), pp. 590.

Hu, C., Sun, M., Xie, Z., Yang, L., Song, Y., Tang, D., and Zhao, J., 2020. Numerical simulation on the forced convection heat transfer of porous medium for turbine engine heat exchanger applications. *Applied Thermal Engineering*, 180 (May), pp. 115845.

Husain, F., Siddiquee, A. N., and Khan, Z. A., 2022. Fabrication Routes of Aluminium Metal Foams : A Review. *Proceedings of the 2nd Indian International Conference on Industrial Engineering and Operations Management*, Telangana, India, 16 - 18 August 2022.

Hyung Jin Sung, Seo Young Kim, and Jae Min Hyun., 1995. Forced convection from an isolated heat source in a channel with porous medium. *International Journal of Heat and Fluid Flow*, 16 (6), pp. 527–535.

Jadhav, P. H., G, T., Gnanasekaran, N., and Mobedi, M., 2022. Performance score based multi-objective optimization for thermal design of partially filled high porosity metal foam pipes under forced convection. *International Journal of Heat and Mass Transfer*, 182.

Jadhav, P. H., and Gnanasekaran, N., 2021. Optimum design of heat exchanging device for efficient heat absorption using high porosity metal foams. *International Communications in Heat and Mass Transfer*, 126 (July), pp. 105475.

Jorge, P., Mendes, M. A. A., Werzner, E., and Pereira, J. M. C., 2019. Characterization of laminar flow in periodic open-cell porous structures. *Chemical Engineering Science*, 201, pp. 397–412.

Kafle, A., Luis, E., Silwal, R., Pan, H. M., Shrestha, P. L., and Bastola, A. K., 2021. 3D / 4D Printing of Polymers : Fused Deposition Modelling (FDM). *Polymers*, 13, pp. 1–37.

Kazim, M. N. A., Abdollah, M. F., Amiruddin, H., Liza, S., and Ramli, F. R., 2022. Surface quality and absorption properties of polymeric composite (PLA-PCU) fabricated using 3D printing for articular cartilage application. *Jurnal Tribologi*, 35 (March), pp. 169–185.

Khadhrawi, S., Segni Oueslati, F., and Bennacer, R., 2020. Mixed convection in a channel partially filled with metal foam blocks. *MATEC Web of Conferences*, 330, pp. 01044.

Khudiakova, A., Berer, M., Niedermair, S., Plank, B., Truszkiewicz, E., Meier, G., Stepanovsky, H., Wolfahrt, M., Pinter, G., and Lackner, J., 2020. Systematic analysis of the mechanical anisotropy of fibre-reinforced polymer specimens produced by laser sintering. *Additive Manufacturing*, 36, pp. 101671.

Kim, Y., Moon, C., Nematollahi, O., Kim, H. D., and Kim, K. C., 2021. Time-resolved piv measurements and turbulence characteristics of flow inside an open-cell metal foam. *Materials*, 14 (13).

Koplik, J., Levine, H., and Zee, A., 1983. Viscosity renormalization in the Brinkman equation. *Physics of Fluids*, 26 (10), pp. 2864–2870.

Kotresha, B., and Gnanasekaran, N., 2018. Investigation of Mixed Convection Heat Transfer Through Metal Foams Partially Filled in a Vertical Channel by Using Computational Fluid Dynamics. *Journal of Heat Transfer*, 140 (11), pp. 1–11.

Kotresha, B., and Gnanasekaran, N., 2020. Numerical Simulations of Fluid Flow and Heat Transfer through Aluminum and Copper Metal Foam Heat Exchanger–A Comparative Study. *Heat Transfer Engineering*, 41 (6–7), pp. 637–649.

Kottasamy, A., Samykano, M., Kadirgama, K., Ramasamy, D., Rahman, M. M., and Pandey, A. K., 2021. Optimization of Impact Energy of Copper-Polylactic Acid (Cu-PLA) Composite Using Response Surface Methodology for FDM 3D Printing. *Journal of Advanced Research in Fluid Mechanics and Thermal Sciences*, 84 (1), pp. 78–90.

Kumaresan, R., Samykano, M., Kadirgama, K., Ramasamy, D., Keng, N. W., and Pandey, A. K., 2021. 3D Printing Technology for Thermal Application: A Brief Review. *Journal of Advanced Research in Fluid Mechanics and Thermal Sciences*, 83 (2), pp. 84–97.

Kuruneru, S. T. W., Vafai, K., Sauret, E., and Gu, Y. T., 2020. Application of porous metal foam heat exchangers and the implications of particulate fouling for energy-intensive industries. *Chemical Engineering Science*, 228, pp. 115968.

Kuznetsov, A. V., 1996. Analytical investigation of the fluid flow in the interface region between a porous medium and a clear fluid in channels partially filled with a porous medium. *Flow, Turbulence and Combustion*, 56 (1), pp. 53–67.

Li, Q., and Hu, P., 2019. Analytical solutions of fluid flow and heat transfer in a partial porous channel with stress jump and continuity interface conditions using LTNE model. *International Journal of Heat and Mass Transfer*, 128, pp. 1280–1295.

Liu, Z., He, Y. L., Yang, Y. F., and Fei, J. Y., 2014. Experimental study on heat transfer and pressure drop of supercritical CO2 cooled in a large tube. *Applied Thermal Engineering*, 70 (1), pp. 307–315.

Lu, W., Zhang, T., and Yang, M., 2016. Analytical solution of forced convective heat transfer in parallel-plate channel partially filled with metallic foams. *International Journal of Heat and Mass Transfer*, 100, pp. 718–727.

Lu, X., Zhao, Y., and Dennis, D. J. C., 2020. Fluid flow characterisation in randomly packed microscale porous beds with different sphere sizes using micro-particle image velocimetry. *Experimental Thermal and Fluid Science*, 118 (April), pp. 110136.

Lupone, F., Padovano, E., Casamento, F., and Badini, C., 2022. Process phenomena and material properties in selective laser sintering of polymers: A review. *Materials*, 15 (1).

Luu, L. H., Philippe, P., and Chambon, G., 2015. Experimental study of the solid-liquid interface in a yield-stress fluid flow upstream of a step. *Physical Review E - Statistical, Nonlinear, and Soft Matter Physics*, 91 (1).

Macini, P., Mesini, E., and Viola, R., 2011. Laboratory measurements of non-Darcy flow coefficients in natural and artificial unconsolidated porous media. *Journal of Petroleum Science and Engineering*, 77 (3–4), pp. 365–374.

Mahmoudi, Y., Karimi, N., and Mazaheri, K., 2014. International Journal of Heat and Mass Transfer Analytical investigation of heat transfer enhancement in a channel partially filled with a porous material under local thermal non-equilibrium condition : Effects of different thermal boundary conditions at the porous-fluid interface. *International Journal of Heat and Mass Transfer*, 70, pp. 875–891.

Matheson, K. E., Cross, K. K., Nowell, M. M., and Spear, A. D., 2017. A multiscale comparison of stochastic open-cell aluminum foam produced via conventional and additive-manufacturing routes. *Materials Science and Engineering A*, 707, pp. 181–192.

McKay, G., 2001. The Beavers and Joseph Condition for Velocity Slip at the Surface of a Porous Medium. *Continuum Mechanics and Applications in Geophysics and the Environment*, pp. 126–139.

Mehrizi, V. A., and Ravari, B. K., 2019. Metallic Foams, New Generation of the Environmental Friendly Materials. *Journal of Environmental Friendly Materials*, 3 (2), pp. 33–39.

Mustapha, K. A., Shikh Anuar, F., Mohd Sa'at, F. A. Z., Zini, N. H. M., Mat Tokit, E., Satishwara Rao, N., Hooman, K., and Abdi, I. A., 2022. Production of Open-Cell Foam Using Additive Manufacturing Method and Porous Morphology Effects. *Proceedings of the 7th International Conference and Exhibition on Sustainable Energy and Advanced Materials (ICE-SEAM 2021),* Melaka, Malaysia, pp. 13–16. Springer Nature Singapore.

Nair, K. A., and Sameen, A., 2015. Experimental Study of Slip Flow at the Fluid-porous Interface in a Boundary Layer Flow. *IUTAM Symposium on Multiphase flows with phase change: challenges and opportunities,* Hyderabad, India, 8-11 December 2014, 15, pp. 293-299.

Nakshatrala, K. B., and Joshaghani, M. S., 2019. On Interface Conditions for Flows in Coupled Free-Porous Media. *Transport in Porous Media*, 130 (2), pp. 577–609.

Narasimmanaidu, S. R., Anuar, F. S., Mohd Sa'at, F. A. Z., and Tokit, E. M., 2021. Numerical and experimental study of flow behaviours in porous structure of aluminium metal foam. *Evergreen*, 8 (3), pp. 658–666.

Neale, G., and Nader, W., 1974. Formulation of Boundary Conditions At the Surface of a Porous Medium. *Soc Pet Eng AIME J*, 14 (5), pp. 434–436.

Nield, D. A., 2009. The beavers - Joseph boundary condition and related matters: A historical and critical note. *Transport in Porous Media*, 78 (3 SPEC. ISS.), pp. 537–540.

Ochoa-tapia, J. A., and Whitakeri, S., 1995. Momentum transfer at the boundary between a porous medium and a homogeneous fluid I. Theoretical development. *International Journal Heat Mass Transfer*, 38 (14), pp. 2635–2646.

Omar, M. R., Abdullah, M. I. H. C., Alkahar, M. R., Abdullah, R., Abdollah, M. F., Subramaniam, M., and Ibramsa, R. S., 2022. Effect of Polyamide-12 Material Compositions on Mechanical Properties and Surface Morphology of SLS 3D Printed Part. *Journal of Mechanical Engineering*, 19 (1), pp. 57–70.

Orihuela, M. P., Shikh Anuar, F., Ashtiani Abdi, I., Odabaee, M., and Hooman, K., 2018. Thermohydraulics of a metal foam-filled annulus. *International Journal of Heat and Mass Transfer*, 117, pp. 95–106.

Pandey, P. M., and Singh, G., 2019. Effect of unit cell shape and strut size on flexural properties of ordered Copper foam. *International Journal of Engineering Sciences*, 12 (3).

Park, S. H., Seo, D. H., and Jeong, J. H., 2020. Experimental and numerical analysis of thermal flow in open-cell porous metal during Darcy-Forchheimer transition regime. *Applied Thermal Engineering*, 181 (September), pp. 116029.

Qu, H., 2020. Additive manufacturing for bone tissue engineering scaffolds. *Materials Today Communications*, 24 (November 2019), pp. 101024.

Qu, Z. G., Xu, H. J., and Tao, W. Q., 2012. Fully developed forced convective heat transfer in an annulus partially filled with metallic foams: An analytical solution. *International Journal of Heat and Mass Transfer*, 55 (25–26), pp. 7508–7519.

Sachlos, E., Czernuszka, J. T., Gogolewski, S., and Dalby, M., 2003. Making tissue engineering scaffolds work. Review on the application ofsolid freeform fabrication technology to the production of tissue engineering scaffolds. *European Cells and Materials*, 5, pp. 29–40.

Saiga, K., Ullah, A. S., Kubo, A., and Tashi., 2021. A Sustainable Reverse Engineering Process. *Procedia CIRP*, 98, pp. 517–522.

Sauret, E., Abdi, I., and Hooman, K., 2014. Fouling of waste heat recovery: Numerical and experimental results. *Proceedings of the 19th Australasian Fluid Mechanics Conference*, December 2014, pp. 1–4.

Sauret, E., Hooman, K., and Saha, S. C., 2014. Cfd Simulations of Flow and Heat Transfer Through the Porous. *ASME 2014 Power Conference*, Baltimore, Maryland, USA, 28-31 July 2014, pp. 1–6.

Sener, M., and Yataganbaba, A., 2016. Forchheimer forced convection in a rectangular channel partially filled with aluminum foam. *Experimental Thermal and Fluid Science*, 75, pp. 162–172.



Shen, B., Yan, H., Sunden, B., Xue, H., and Xie, G., 2017. International Journal of Heat and Mass Transfer Forced convection and heat transfer of water-cooled microchannel heat sinks with various structured metal foams. *International Journal of Heat and Mass Transfer*, 113, pp. 1043–1053.

Shikh Anuar, F., Ashtiani Abdi, I., and Hooman, K., 2018. Flow visualization study of partially filled channel with aluminium foam block. *International Journal of Heat and Mass Transfer,* 127, pp. 1197–1211.

Shikh Anuar, F., Ashtiani Abdi, I., Odabaee, M., and Hooman, K., 2018. Experimental study of fluid flow behaviour and pressure drop in channels partially filled with metal foams.

*Experimental Thermal and Fluid Science*, 99 (May), pp. 117–128.

Shokouhmand, H., Jam, F., and Salimpour, M. R., 2011. The effect of porous insert position on the enhanced heat transfer in partially filled channels. *International Communications in Heat and Mass Transfer*, 38 (8), pp. 1162–1167.

Shuja, S. Z., and Yilbas, B. S., 2007. Flow over rectangular porous block in a fixed width channel: Influence of porosity and aspect ratio. *International Journal of Computational Fluid Dynamics*, 21 (7–8), pp. 297–305.

Silva, C., Pais, A. I., Caldas, G., Gouveia, B. P. P. A., Alves, J. L., and Belinha, J., 2021. Study on 3D printing of gyroid-based structures for superior structural behaviour. *Progress in Additive Manufacturing*, 6 (4), pp. 689–703.

Solomon, I. J., Sevvel, P., and Gunasekaran, J., 2020. A review on the various processing parameters in FDM. *Materials Today: Proceedings*, 37 (Part 2), pp. 509–514.

Štefan, K., and Janette, B., 2022. Reverse engineering in automotive design component. *International Scientific Journals of Scientific Technical Union of Mechanical Engineering*, 65 (2), pp. 62–65.

Suga, K., and Nishio, Y., 2009. Three dimensional microscopic flow simulation across the interface of a porous wall and clear fluid by the lattice boltzmann method. *Open Transport Phenomena Journal*, 1 (1), pp. 35–44.

Sutygina, A., Betke, U., Hasemann, G., and Scheffler, M., 2020. Manufacturing of open-cell metal foams by the sponge replication technique. *IOP Conference Series: Materials Science and Engineering*, 882 (1).

Tan, W. C., Saw, L. H., Thiam, H. S., Xuan, J., Cai, Z., and Yew, M. C., 2018. Overview of porous media/metal foam application in fuel cells and solar power systems. *Renewable and*

*Sustainable Energy Reviews*, 96 (November), pp. 181–197.

Tang, Y., Wang, H., and Huang, C., 2023. Pore-scale numerical simulation of the heat transfer and fluid flow characteristics in metal foam under high Reynolds numbers based on tetrakaidecahedron model. *International Journal of Thermal Sciences*, 184 (April 2022), pp. 107903.

Terzis, A., Zarikos, I., Weishaupt, K., Yang, G., Chu, X., Helmig, R., and Weigand, B., 2019. Microscopic velocity field measurements inside a regular porous medium adjacent to a low Reynolds number channel flow. *Physics of Fluids*, 31 (4).

Tupin, S., and Ohta, M., 2020. Assessing porous media permeability in non-Darcy flow: A re-evaluation based on the Forchheimer equation. *Materials*, 13 (11), pp. 2–5.

Vafai, K., and Kim, S. J., 1990. Fluid mechanics of the interface region between a porous medium and a fluid layer-an exact solution. *International Journal of Heat and Fluid Flow*, 11 (3), pp. 254–256.

Valdés-Parada, F. J., Goyeau, B., and Alberto Ochoa-Tapia, J., 2006. Diffusive mass transfer between a microporous medium and an homogeneous fluid: Jump boundary conditions. *Chemical Engineering Science*, 61 (5), pp. 1692–1704.

Vazifeshenas, Y., Sedighi, K., and Shakeri, M., 2020. Open Cell Metal Foam as Extended Coolant Surface – Fuel Cell Application. *Fuel Cells*, 20 (2), pp. 108–115.

Wan, T., Liu, Y., Zhou, C., Chen, X., and Li, Y., 2021. Fabrication, properties, and applications of open-cell aluminum foams: A review. *Journal of Materials Science and Technology*, 62, pp. 11–24.

Wang, L., Li, E. L., Shen, H., Zou, R. P., Yu, A. B., and Zhou, Z. Y., 2020. Adhesion effects on spreading of metal powders in selective laser melting. *Powder Technology*, 363, pp. 602-610.

Wang, S., Ding, Y., Yu, F., Zheng, Z., and Wang, Y., 2020. Crushing behavior and deformation mechanism of additively manufactured Voronoi-based random open-cell polymer foams. *Materials Today Communications*, 25 (February), pp. 101406.

Wood, B. D., Apte, S. V., Liburdy, J. A., Ziazi, R. M., He, X., Finn, J. R., and Patil, V. A., 2015. A comparison of measured and modeled velocity fields for a laminar flow in a porous medium. *Advances in Water Resources*, 85, pp. 45–63.

Wood, B. D., Quintard, M., and Whitaker, S., 2000. Jump conditions at non-uniform boundaries: The catalytic surface. *Chemical Engineering Science*, 55 (22), pp. 5231–5245.

Wu, Z., and Mirbod, P., 2018. Experimental analysis of the flow near the boundary of random porous media. *Physics of Fluids*, 30 (4).

Xu, H., Zhao, C., and Vafai, K., 2018. Analysis of double slip model for a partially filled porous microchannel—An exact solution. *European Journal of Mechanics, B/Fluids*, 68, pp. 1–9.



Xu, Z. G., and Gong, Q., 2018. Numerical investigation on forced convection of tubes partially filled with composite metal foams under local thermal non-equilibrium condition. *International Journal of Thermal Sciences*, 133 (November 2017), pp. 1–12.

Xu, Z. G., Qin, J., Zhou, X., and Xu, H. J., 2018. Forced convective heat transfer of tubes sintered with partially-filled gradient metal foams (GMFs) considering local thermal non-equilibrium effect. *Applied Thermal Engineering*, 137 (July 2017), pp. 101–111.

Yerramalle, V., Premachandran, B., and Talukdar, P., 2020. Numerical investigation of the performance of interface conditions for fluid flow through a partially filled porous channel. *Thermal Science and Engineering Progress*, 20 (July), pp. 100628.

Yerramalle, V., Premachandran, B., and Talukdar, P., 2021. Mixed convection from a heat source in a channel with a porous insert: A numerical analysis based on local thermal non-equilibrium model. *Thermal Science and Engineering Progress*, 25 (February), pp. 101010.

Yu, P., Wang, Y., Ji, R., Wang, H., and Bai, J., 2021. Pore-scale numerical study of flow characteristics in anisotropic metal foam with actual skeleton structure. *International Communications in Heat and Mass Transfer*, 126 (June), pp. 105401.

Zargartalebi, M., and Azaiez, J., 2019. Flow dynamics and heat transfer in partially porous microchannel heat sinks. *Journal of Fluid Mechanics*, 875, pp. 1035–1057.

Zhang, F., Li, Z., Xu, M., Wang, S., Li, N., and Yang, J., 2022. A review of 3D printed porous ceramics. *Journal of the European Ceramic Society*, 42 (8), pp. 3351–3373.

Zhou, Z., Hu, Z., Wang, D., and Wu, H., 2022. Visualized-experimental investigation on the melting performance of PCM in 3D printed metal foam. *Thermal Science and Engineering Progress*, 31 (December 2021), pp. 101298.

## APPENDIX A: Example Calculation (Dimensional Analysis)

$$\pi_1 = U_s U_{inlet}^{\ a} \rho_{fluid}^{\ b} h_c^{\ c}$$

$$\pi_1 = (L/T)(L/T)^a (M/L^{-3})^b (L)^c$$

$$(M^0 L^0 T^0) = (L/T)(L/T)^a (M/L^{-3})^b (L)^c$$

Generic of equation:

M:
$M^0 = (M^0)^a\ (M^1)^b\ (M^0)^c$
$0 = 0\ (a) + 1(b) + 0\ (c)$
$b = 0$

T:
$T^0 = (T)(T^{\ 1})^a\ (T^{\ 0})^b\ (T^{\ 0})^c$
$0 = 1 + 1(a) + (0)(b) + 0(c)$
$0 = 1 + a$
$a = -1$

L:
$L^0 = (L)(L^1)^a\ (L^{-3})^b\ (L^1)^c$
$0 = 1 + 1(a) + (-3)(b) + 1(c)$
$0 = 1 + a - 3b + c$

Solving the equation by inserting all the constant:
$a - 3b + c = -1$
$(-1) - 3(0) + c = -1$
$C = 0$

substitute back inside the equation:

$$\pi_1 = U_s U_{inlet}^{\ a} \rho_{fluid}^{\ b} h_c^{\ c}$$

$$\pi_1 = U_s U_{inlet}^{\ -1} \rho_{fluid}^{\ 0} h_c^{\ 0}$$

$$\pi_1 = U_s / U_{inlet}$$

APPENDIX B: Pressure Drop Result (3D printed foam)

| **Foam Scale** | **Foam Height (mm)** | **Velocity ($ms^{-1}$)** | **Reynold Number** | **Pressure Drop, $\Delta P/\Delta l$ ($Pa.m^{-1}$)** |
|---|---|---|---|---|
| 2 | 30 | 1 | 6042.46 | 31.58 |
| 2 | 60 | 1 | 6042.46 | 47.93 |
| 2 | 90 | 1 | 6042.46 | 103.34 |
| 2 | 100 | 1 | 6042.46 | 155.88 |
| 4 | 30 | 1 | 6042.46 | 17.33 |
| 4 | 60 | 1 | 6042.46 | 28.01 |
| 4 | 90 | 1 | 6042.46 | 54.47 |
| 4 | 100 | 1 | 6042.46 | 70.29 |
| 6 | 30 | 1 | 6042.46 | 14.13 |
| 6 | 60 | 1 | 6042.46 | 20.63 |
| 6 | 90 | 1 | 6042.46 | 41.82 |
| 6 | 100 | 1 | 6042.46 | 55.25 |
| 2 | 30 | 3 | 18127.38 | 166.41 |
| 2 | 60 | 3 | 18127.38 | 221.94 |
| 2 | 90 | 3 | 18127.38 | 452.97 |
| 2 | 100 | 3 | 18127.38 | 682.36 |
| 4 | 30 | 3 | 18127.38 | 83.26 |
| 4 | 60 | 3 | 18127.38 | 126.81 |
| 4 | 90 | 3 | 18127.38 | 247.19 |
| 4 | 100 | 3 | 18127.38 | 322.25 |
| 6 | 30 | 3 | 18127.38 | 83.90 |
| 6 | 60 | 3 | 18127.38 | 90.18 |
| 6 | 90 | 3 | 18127.38 | 189.94 |
| 6 | 100 | 3 | 18127.38 | 254.22 |
| 2 | 30 | 5 | 30212.29 | 720.37 |
| 2 | 60 | 5 | 30212.29 | 835.00 |
| 2 | 90 | 5 | 30212.29 | 1818.26 |
| 2 | 100 | 5 | 30212.29 | 2753.65 |
| 4 | 30 | 5 | 30212.29 | 319.04 |
| 4 | 60 | 5 | 30212.29 | 496.77 |
| 4 | 90 | 5 | 30212.29 | 1010.11 |
| 4 | 100 | 5 | 30212.29 | 1325.22 |
| 6 | 30 | 5 | 30212.29 | 343.53 |
| 6 | 60 | 5 | 30212.29 | 350.73 |
| 6 | 90 | 5 | 30212.29 | 780.14 |
| 6 | 100 | 5 | 30212.29 | 1015.29 |

APPENDIX C: Velocity Result (3D printed foam)

| Foam Scale | Foam Height (mm) | Frequency (Hz) | Mean Velocity ($ms^{-1}$) | | |
|---|---|---|---|---|---|
| | | | Upstream | Downstream | Interface / Slip |
| 2 | 30 | 10 | 1.25 | 1.56 | 1.64 |
| 2 | 60 | 10 | 1.23 | 1.52 | 2.39 |
| 2 | 90 | 10 | 1.09 | 1.84 | 3.15 |
| 4 | 30 | 10 | 1.25 | 1.49 | 1.82 |
| 4 | 60 | 10 | 1.22 | 1.37 | 2.31 |
| 4 | 90 | 10 | 1.09 | 1.31 | 2.65 |
| 6 | 30 | 10 | 1.26 | 1.45 | 1.95 |
| 6 | 60 | 10 | 1.23 | 1.43 | 2.18 |
| 6 | 90 | 10 | 1.12 | 1.23 | 2.45 |
| 2 | 30 | 22 | 3.09 | 3.39 | 3.90 |
| 2 | 60 | 22 | 3.08 | 3.38 | 4.87 |
| 2 | 90 | 22 | 2.80 | 3.96 | 5.47 |
| 4 | 30 | 22 | 3.01 | 3.25 | 4.11 |
| 4 | 60 | 22 | 3.00 | 2.94 | 4.60 |
| 4 | 90 | 22 | 2.69 | 3.30 | 4.72 |
| 6 | 30 | 22 | 3.03 | 3.18 | 4.00 |
| 6 | 60 | 22 | 3.03 | 3.35 | 4.52 |
| 6 | 90 | 22 | 2.90 | 3.09 | 4.53 |
| 2 | 30 | 46 | 5.42 | 5.96 | 7.17 |
| 2 | 60 | 46 | 5.32 | 6.58 | 9.98 |
| 2 | 90 | 46 | 4.62 | 7.89 | 9.77 |
| 4 | 30 | 46 | 5.18 | 5.68 | 8.03 |
| 4 | 60 | 46 | 5.19 | 5.51 | 9.58 |
| 4 | 90 | 46 | 4.63 | 5.99 | 8.43 |
| 6 | 30 | 46 | 5.25 | 5.76 | 7.96 |
| 6 | 60 | 46 | 5.22 | 5.85 | 10.91 |
| 6 | 90 | 46 | 4.88 | 5.59 | 8.06 |

APPENDIX D: Pressure Drop Result (Conventional metal foam)

| Foam Density | Foam Height (mm) | Velocity ($ms^{-1}$) | Reynold Number | Pressure Drop, $\Delta P/\Delta l$ ($Pa.m^{-1}$) |
|---|---|---|---|---|
| 10 | 20 | 1 | 6042.46 | 15.25 |
| 10 | 20 | 3 | 18127.38 | 77.80 |
| 10 | 20 | 5 | 30212.29 | 298.63 |
| 30 | 20 | 1 | 6042.46 | 31.06 |
| 30 | 20 | 3 | 18127.38 | 127.78 |
| 30 | 20 | 5 | 30212.29 | 519.33 |

APPENDIX E: Velocity Result (Conventional metal foam)

| Foam Density | Foam Height (mm) | Frequency (Hz) | Mean Velocity ($ms^{-1}$) | | |
|---|---|---|---|---|---|
| | | | Upstream | Downstream | Interface / Slip |
| 10 | 20 | 10 | 1.26 | 1.36 | 2.17 |
| 10 | 20 | 22 | 3.18 | 2.78 | 4.43 |
| 10 | 20 | 46 | 5.11 | 5.46 | 8.24 |
| 30 | 20 | 10 | 1.42 | 1.51 | 2.41 |
| 30 | 20 | 22 | 2.91 | 3.10 | 4.43 |
| 30 | 20 | 46 | 5.20 | 5.70 | 8.39 |